NASA CR-135080
SOLAR ER-2519

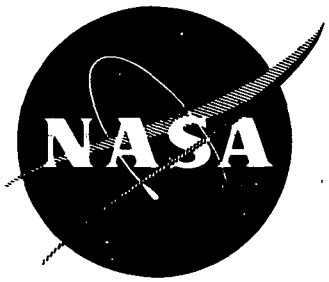

ADVANCED RADIAL INFLOW TURBINE ROTOR PROGRAM– DESIGN AND DYNAMIC TESTING

by

C. Rodgers

SOLAR DIVISION OF INTERNATIONAL HARVESTER

prepared for

NATIONAL AERONAUTICS AND SPACE ADMINISTRATION

NASA Lewis Research Center

Contract NAS 3-18524

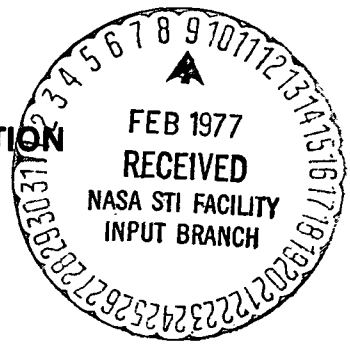

1. Report No.	2. Government Accession No.	3. Recipient's Catalog No.
NASA CR-135080		

4. Title and Subtitle	5. Report Date
Advanced Radial Inflow Turbine Rotor Program - Design and Dynamic Testing	Sept. 1976
	6. Performing Organization Code

7. Author(s)	8. Performing Organization Report No.
Colin Rodgers	ER 2519
	10. Work Unit No.

9. Performing Organization Name and Address	11. Contract or Grant No.
Solar Division of International Harvester P. O. Box 80966 San Diego, Calif. 92138	NAS 3-18524
	13. Type of Report and Period Covered
12. Sponsoring Agency Name and Address	Contractor Report
National Aeronautics and Space Administration Washington D. C. 20546	14. Sponsoring Agency Code

15. Supplementary Notes

Program Monitor, Robert Y. Wong, Fluid System Components Division
NASA Lewis Research Center, Cleveland, Ohio

16. Abstract

The objective of this program was the advancement of small, cooled, radial inflow turbine technology in the area of operation at higher turbine inlet temperatures. The first step of this objective was accomplished by designing, fabricating, and subjecting to limited mechanical testing an advanced gas generator rotating assembly comprising a radial inflow turbine and two-stage centrifugal compressor. The radial inflow turbine and second-stage compressor were designed as an integrally machined monorotor with turbine cooling taking place basically by conduction to the compressor.

Design turbine inlet rotor gas temperature, rotational speed, and overall gas generator compressor pressure ratio were 1422 K (2560°R), 71,222 rpm, and 10/1 respectively. Mechanical testing on a fabricated rotating assembly and bearing system covered 1,000 cold start/stop cycles and three spins to 120% design speed (85,466 rpm).

17. Key Words (Suggested by Author(s))	18. Distribution Statement
Cooled Radial Inflow Turbine High Turbine Inlet Temperatures	Unclassified - Unlimited

19. Security Classif. (of this report)	20. Security Classif. (of this page)	21. No. of Pages	22. Price*
UNCLASSIFIED	UNCLASSIFIED	100	

* For sale by the National Technical Information Service, Springfield, Virginia 22161

Page Intentionally Left Blank

FOREWORD

This is the final report covering work performed by Solar under Contract No. NAS3-18524 during the period June 10, 1974 through June 1, 1976.

This contract was under the technical direction of Mr. R. Wong, Lewis Research Center of the National Aeronautics and Space Administration.

Solar participation was under the direction of Mr. L. Blinman, program manager, and Mr. C. Rodgers, principal investigator. Recognition is also given to the following Solar personnel for their special skill contributions:

G. Aigret	Thermal Analysis
H. Lindgren	Stress Analysis
T. Psichogios	Dynamic Analysis
M. Lafferty	Mechanical Design
T. Witkowski	Experimental Test

Page
Intentionally
Left Blank

TABLE OF CONTENTS

TABLE OF CONTENTS (CONT)

LIST OF FIGURES

LIST OF FIGURES (Continued)

LIST OF TABLES

LIST OF SYMBOLS

		SI Units	English Units
D	Diameter	cm	inch
g	Gravitational constant	m/s^2	ft/sec^2
HP	Horsepower		
J	Joules equivalent	k cal/kg	Btu/lb
N or RPM	Rotational speed	rpm	rpm
N_{Nu}	Nusselt number	--	--
P	Total pressure	Pascal (Pa)	psia
p	Static pressure	Pascal	psia
N_{Pr}	Prandtl number	--	--
R	Gas constant	J/(kg.K)	ft lb/lb-°R
RMS	Root mean square	--	--
N_{Re}	Reynolds number	--	--
SFC	Specific fuel consumption	kg/kW-hr	lb/hp-hr
T	Total temperature	K	°R
U	Blade tip speed	m/s	ft/sec
UTS	Ultimate tensile strength	Pascal	ksi
W	Airflow	kg/s	pps
Δ	Difference	--	--
δ	Inlet pressure/14.7 psia	--	--
η	Efficiency	--	--
θ	Inlet temperature/519°R	--	--
ρ	Density	kg/m^3	lb/ft^3
γ	Specific heat ratio	--	--

Subscripts

c	Compressor
gp	Gas producer
t	Turbine

SUMMARY

The objective of this program was the advancement of small, cooled, radial turbine technology in the area of operation at higher turbine inlet temperatures. The first step of this objective was accomplished by designing, fabricating, and limited mechanical testing of a monorotor engine configuration in which turbine cooling is by direct conduction of heat to the centrifugal compressor blading located on the forward face of the radial turbine disc. Direct conduction cooling at turbine inlet temperatures from 1478 K (2660°R) to 1700 K (3060°R) was studied, along with the use of supplementary internal cooling.

Detailed analysis indicated that the initial objective of attaining a design life of 1000 hours with a mixed rotor gas inlet temperature of 1478 K (2660°R) was not analytically feasible. Derating to 1422 K (2560°R) is recommended to reach the required design life. In addition, the particular monorotor configuration results in a tip leakage of 7 percent between the compressor and turbine flowpaths, diluting the monostator nozzle exit gas temperature. As a consequence, burner exit temperature is 95°C (170°F) hotter then mixed rotor inlet gas temperature, requiring the use of an internally cooled monostator.

A complete monorotor engine rotating assembly comprising three rotors in series, overhung from a forward bearing capsule, was designed and fabricated. Mechanical testing of the rotating assembly was completed in a high-speed spin pit facility. One thousand stop/start cycles and three spins to 120 percent design speed (85,466 rpm) were successfully completed. Monorotor dynamic distortions were measured, and the analytical finite element stress model computations confirmed.

INTRODUCTION

Cooled radial-inflow turbines are of interest for small (less than 2.27kg/s or 5 pps) gas turbine engines. However, the technology of cooling radial-inflow turbines, particularly rotors, is in a rudimentary state. The purpose of this program was to advance that technology. As a focal point for the work effort, a cooling scheme using the monorotor concept for a radial-inflow gas generator turbine rotor of an existing aerodynamic design was to be designed, fabricated, and mechanically tested to demonstrate the structural integrity of the cooled rotor. The complete baseline turbine aerodynamic design was to be provided by NASA.

The monorotor arrangement is an existing low-cost method of cooling a radial inflow turbine rotor. The monorotor is manufactured integrally back to back with the compressor as a single casting; heat from the turbine flows through the common disc to the cold compressor vanes. The turbine is also cooled by controlled leakage air flowing from the compressor tip into the turbine rotor and down the face of the disc. The turbine nozzle and compressor diffuser are also an integrated unit and form a monostator, the hot turbine nozzle being cooled by conduction to the diffuser vanes and by supplementary film cooling.

Although the monorotor concept permits operation at elevated turbine inlet temperatures with potentially low cost components and minimum cooling system performance penalties, the attainment of higher pressure ratios is required to obtain simple cycle, specific fuel consumption values approaching 0.3 kg/kW-hr (0.5 lb/hp-hr). As a result, studies were completed at Solar on the application of a monorotor in a small gas turbine using a two-stage centrifugal compressor operating at a high overall pressure ratio in the range of 10 to 12, the drive turbine for this compressor being the NASA baseline configuration.

Lewis Research Center was particularly interested in this cooling concept with an engine configuration sized to pass an airflow of 0.91 kg/s (2.0 pps). Such an engine was to have a total design life of 5000 hours, of which at least 1000 hours would be spent at maximum rated power. Additionally, the engine was to be capable of completing 30,000 transient power cycles to maximum rated power and 15,000 start/stop cycles. This report describes the work of the Lewis Research Center Contract, which was initiated to design, fabricate, and subject to limited mechanical testing the important components of the monorotor engine configuration. Included is a description of the preliminary design and optimization, tradeoffs during the final selections, detail design, and results of limited mechanical testing of the rotating assembly components.

PRELIMINARY DESIGN

The objectives of the preliminary design study were to obtain solutions for the cooling, mechanical fabrication, and life problems of a monorotor operating at gas inlet temperatures of 1478, 1589, and 1700 K (2660, 2860, 3060°R) based upon reasonable extension of existing technology. Supplementary air cooling schemes were also to be studied for operation at 1589 and 1700 K (2860, 3060°R). Thermal and finite element stress models were to be operated for appraisal of thermal and dynamic stresses.

Initial Thermal Analysis

During initial thermal analyses of the monorotor cooling concept, an approximate expression was derived to calculate the average disc and peak blade metal temperatures, verifying that the conduction cooling concept was feasible without an inordinate amount of detail calculation. It was reasoned early that if the convection coefficients of both the compressor and turbine were similar, the average metal temperature at the center of the rotor would approach the average of the turbine and compressor relative air temperature, i.e.,

$$\text{Average rotor metal temperature} \sim 0.5\left(T_3 + T_2 - 1.8\ \frac{U_t^2}{2gJC_p}\right)$$

where

T_3 = turbine inlet gas temperature

T_2 = compressor exit gas temperature

U_t = turbine tip speed

$$\text{Exducer metal temperature} \sim \text{turbine exit temperature} + \frac{U_t^2}{\epsilon^2 2gJC_p}$$

where

$$\epsilon = \frac{\text{rotor inlet diameter}}{\text{rotor exit diameter}}$$

Following this direct reasoning, a simple assessment of the maximum temperature within a monorotor was made, assuming that the heat flux from the exducer portion of the turbine was negligible. Monorotor equilibrium metal temperatures under these assumptions are shown in Figure 1 (for a uniform burner profile). It is indicated that with a turbine inlet temperature of 1478 K (2660°R) and a pressure ratio of 10.0, the average disc metal temperature would be only 933 K (1680°R), and the maximum metal temperature in the exducer would be 1217 K (2190°R).

Maximum metal temperatures will occur along the turbine rotor shroud streamtube where, fortunately, blade stresses are lowest. Nevertheless, turbine life may be determined by peak metal temperature, which governs blade oxidation and corrosion, rather than stress rupture considerations.

Therefore, to reduce temperatures along the tip, rotor tip blade height, blade taper ratio, and turbine reaction should be optimized for turbine temperature, aerodynamic performance, and life considerations. Small blade heights and large taper ratios are desirable to transmit the heat from the blade into the cooler disc. These conditions increase nozzle and rotor pressure losses, and further, small rotor blade heights demand extremely small rotor-shroud clearances, which are not easy to maintain in a high temperature environment. Monorotor metal temperatures depend on parameters other than average gas temperatures and relative velocities, and additional axial and radial temperature gradients will exist due to:

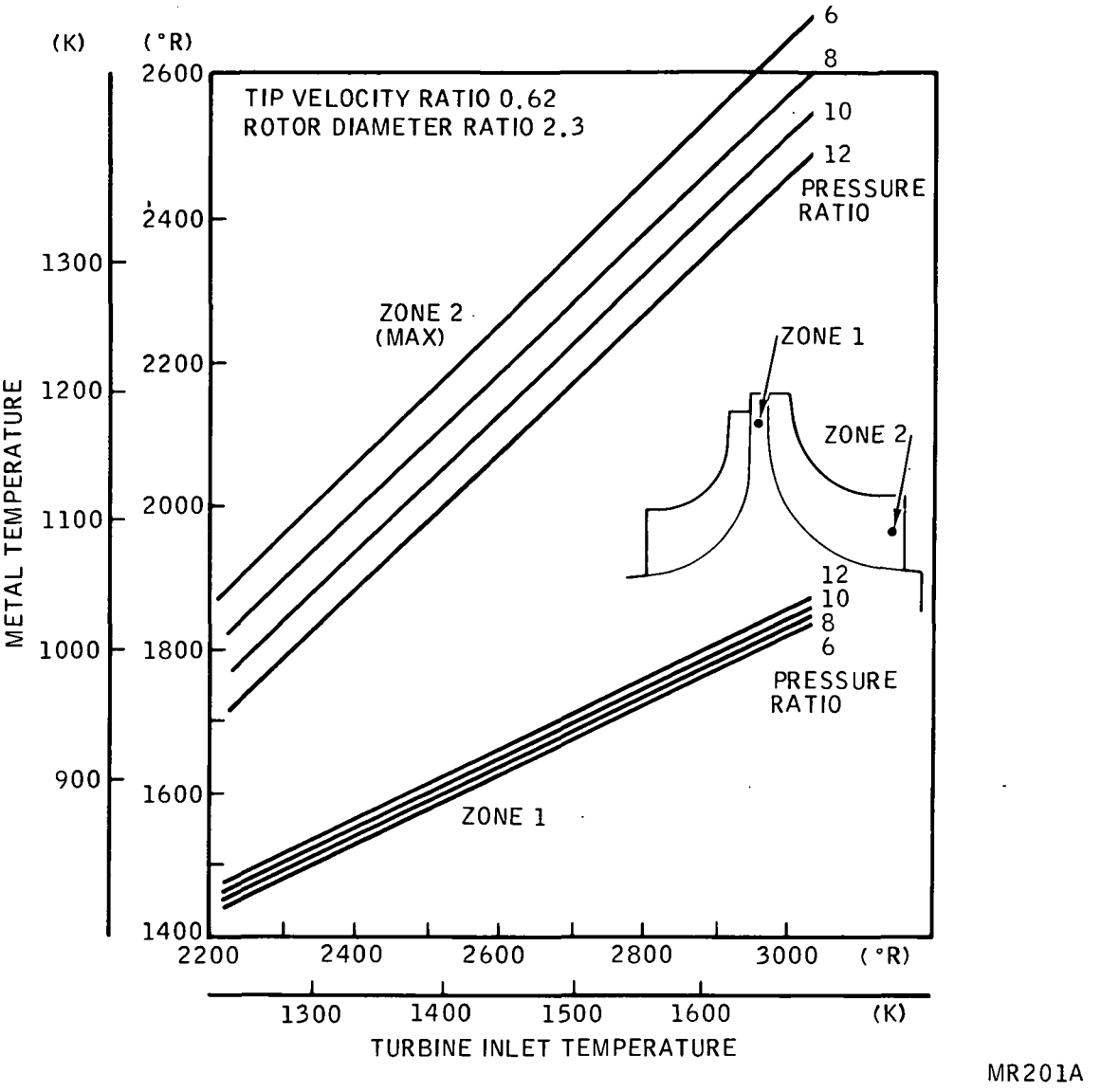

Figure 1 - Estimated Metal Temperatures (Simplified Method)

- Combustor pattern factor
- Tip seal leakage effects
- Additional heat sinks such as the shaft
- Radiation effects

The transfer of monorotor heat back into the compressor air can be determined from the data of Swartout*. With some simplifying assumptions, it can be shown that the additional heat transferred during compression is approximated by:

* Experimental Investigation of Heat Transfer in a Radial Inflow Gas Turbine Rotor, Purdue University Report F-58-2.

$$\Delta T = \left[T_R - \left(T_2 - \frac{\Delta T_c}{4} \right) \right] \frac{D_2^2 \; U_2^{0.8}}{2.5W \; 10^5}$$

where

T_R = is the average disc metal temperature

Examination of this expression reveals that the amount of heat pickup is proportional to the square of the compressor tip diameter and inversely proportional to compressor airflow; thus, low specific speed compressors (large diameter, low flow) will transfer large amounts of heat relative to the airflow.

Second-stage compressor heat transfer was calculated by this method at three turbine inlet temperatures, using a pressure ratio of 10.0 and airflow of 0.91 kg/s (2.0 pps); the results are:

Turbine Inlet Temperature	K	1478	1589	1700
	°R	2660	2860	3060
2nd Stage Compressor Inlet Temperature Rise	K	8.4	11.0	13.6
	°R	15.2	19.8	24.4

The internal (polytropic) efficiency of both the compressor and turbine are basically independent of the heat transfer process. Addition of heat during compression and extraction of heat during expansion simply change the momentum exchange (pressure ratio).

Various additional analytical models have been developed to treat the effect of heat transfer from the hot turbine to the cold compressor. Complex models consist of small-stage compression with incremental heating and small-stage expansion with incremental cooling. The incremental heat quantities to each stage are computed from the local heat transfer coefficients. Before discussing such a model, the following limiting conditions may be postulated:

- Maximum performance penalty would result if the monorotor heat were extracted at the turbine entry and transferred back to the compressor inlet.

- A negligible performance penalty would occur if the monorotor heat were extracted at the turbine entry and transferred back to the compressor discharge. Performance would be the same as without the monorotor.

- A performance gain would result if the monorotor heat were extracted at turbine exit and transferred back to the compressor rotor discharge (equivalent to regeneration).

For convervatism, the heat transfer state yielding the maximum performance penalty (above) was adopted in the initial cycle performance calculations.

Component Size Effects on Cycle Performance

To investigate the cycle performance of a hypothetical engine of fixed power operating at higher turbine inlet temperatures, the adopted heat transfer model was postulated with the following conditions.

Pressure Ratio	Turbine Inlet Temp		Compressor Inlet Temperature Rise	
	(K)	(°R)	(K)	(°R)
10	1478	2660	4.4	8
10	1589	2860	6.1	11
10	1700	3060	7.8	14

A cycle performance analysis technique was used in which component efficiencies were taken as a function of size, i.e., airflow. Increasing turbine inlet temperature for a fixed engine output (320 hp) resulted in lower airflow and hence slightly reduced compressor and turbine efficiencies.

The results of this cycle analysis are shown on Figure 2 where specific fuel consumption (sfc) and power turbine inlet temperature are plotted against turbine inlet temperature for various leakage rates. The leakage as shown is external leakage loss at compressor discharge conditions. Figure 2 indicates that no improvement in sfc would be obtained by operating at turbine inlet temperatures higher than 1478 K (2660°R) and that power turbine inlet temperatures would increase to a level requiring cooling of the power turbine blades. Furthermore, turbine inlet temperatures above 1478 K would also require supplementary cooling of the stationary shrouds and nozzle, thus causing further increases in sfc even if constant airflow (no size penalty) was assumed.

Effects of Internal Heat Transfer

Although heat transfer to the compressor reduces the effective cycle temperature ratio for a given maximum temperature, it does not necessarily decrease compressor efficiency. For a given compressor tip speed, heat addition decreases the pressure ratio, but the internal or polytropic efficiency remains essentially unchanged. In fact, if the compressor of a monorotor gas turbine were specially matched for heat addition, a slight efficiency increase could result from elimination of back-shroud disc friction. The compressor would, however, require a slightly higher tip speed to maintain the unheated pressure ratio.

To determine the worst effect of internal heat transfer on engine performance, it was pessimistically assumed that all of the heat flux soaked through to the compressor inlet rather than occurring gradually throughout the compression process at a rate dependent on temperature gradients and geometry.

A refined analytical model was subsequently used to calculate the effect of internal (monorotor) heat transfer as defined in Appendix A. This model was adapted to an existing variable specific heat cycle analysis and was employed to determine the theoretical difference in gas turbine performance as influenced by tip leakage and heat flux to the second-stage compressor. It was assumed in this analytical model that the effectiveness of leakage flow in producing turbine work was 75 percent of the primary flow. Figure 3 shows the computed influence of monorotor heat transfer and tip leakage on engine output power and specific fuel consumption. With a heat rise corresponding to 8.3 K (15°R) inlet heating and with a 7 percent tip leakage, it was estimated that output power and sfc would worsen by 3.2 and 2.2 percent, respectively.

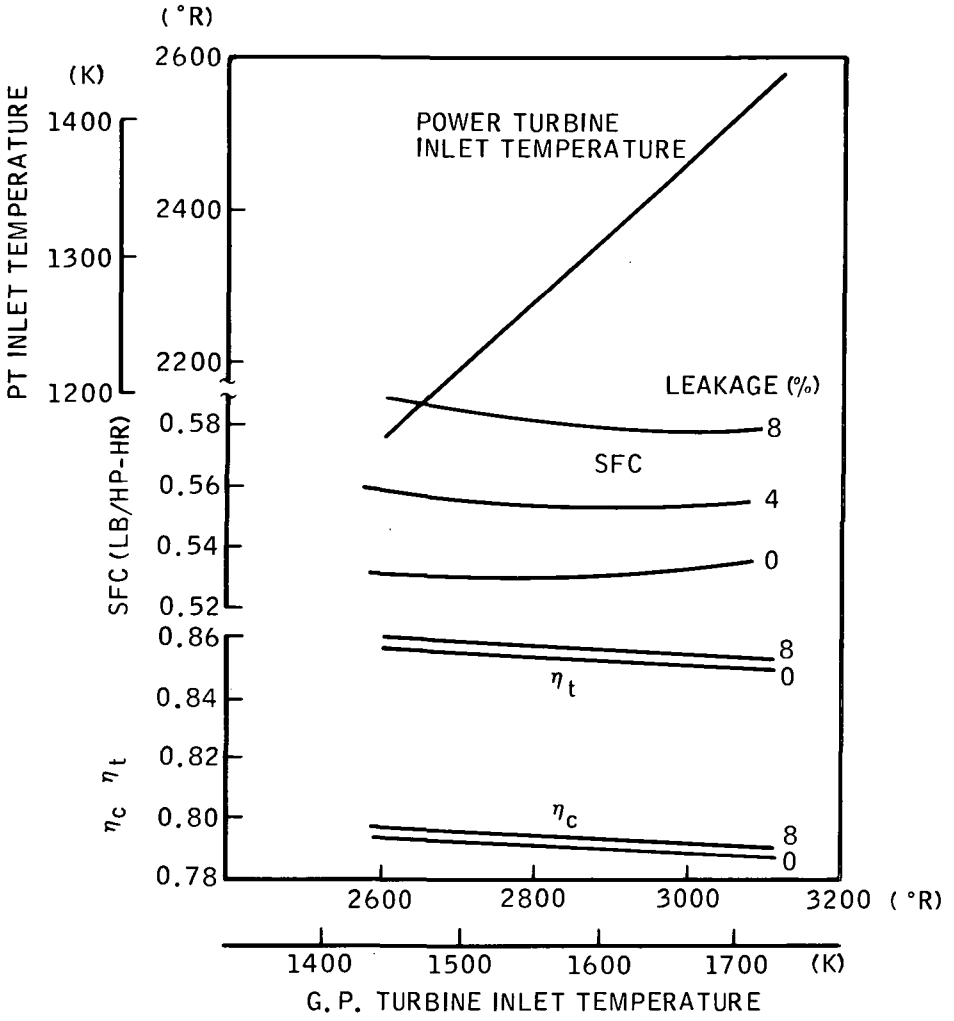

MR202B

Figure 2 - Cycle Optimization - Constant HP Pressure Ratio 10

On the basis of these results, it was decided initially to select the preliminary design conditions listed in Table I for further study. Assuming 7 percent internal tip leakage plus 5 percent external leakage, output power and sfc were estimated to be 314 hp and 0.24 kg/hp-hr (0.532 lb/hp-hr), respectively, for a pressure ratio of 10.0 and a turbine inlet temperature of 1478 K (2660°R). Note that 7 percent internal tip leakage will require a maximum burner temperature of 1536 K (2765°R) mixing to the 1478 K (2660°R) condition within the turbine rotor. Table I also indicates the apparent effect of internal heat transfer, in that the overall compressor adiabatic efficiency would apparently decrease 2 percentage points, and the turbine overall adiabatic efficiency would apparently remain unchanged if calculated from desired temperature and pressure conditions.

Cycle performance at higher turbine inlet temperatures was estimated assuming that additional cooling of the gas generator and power turbines would be required amounting to an equivalent 2 and 5 percent external leakage loss at the 1644 K (2860°R) and 1144 K (3060°R) turbine inlet temperatures. Comparative cycle performances at the three

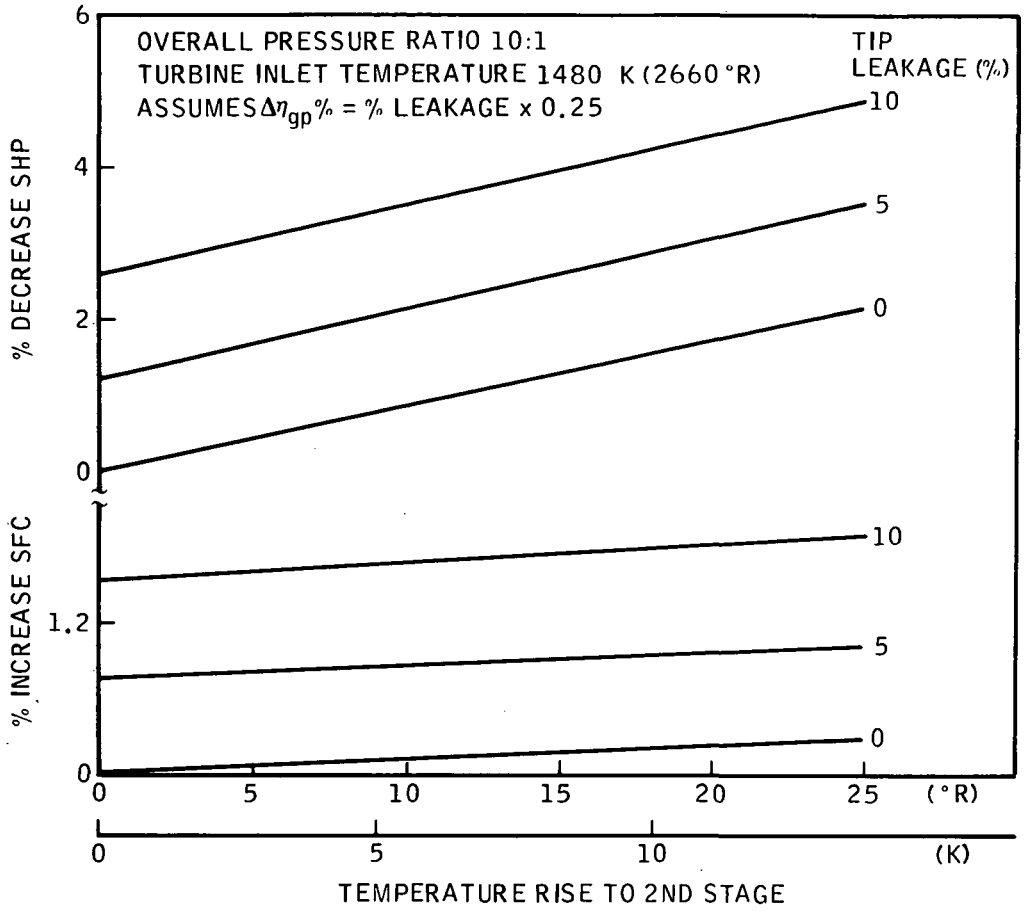

MR203A

Figure 3 - Estimated Effect of Monorotor Heat Transfer on SFC and Output Power

turbine temperatures are listed in Table II where, in addition to supplementary cooling losses, power turbine efficiency is slightly reduced as a consequence of operating at higher stage pressure ratios.

TABLE I - PRELIMINARY DESIGN POINT

Parameter	Units	Zero Temp Rise	8.3 K (15°R) Temp Rise
Compressor Airflow	kg (pps)	0.907 (2.0)	0.907 (2.0)
Compressor Pressure Ratio		10.0	10.0
Compressor Adiabatic Efficiency	%	79.5	77.5*
Compressor Specific Heat Ratio		1.393	1.393
Compressor Discharge Temperature	K (°R)	619 (1115)	627 (1130)
Burner Pressure Loss	%	5	5

Table Continued..

* Apparent adiabatic values from pressure ratio and enthalpy change

TABLE I - Continued

Parameter	Units	Zero Heat Flux	8.3 K (15°R) Heat Rise
Burner Efficiency	%	98	98
Tip Leakage	%	0	7
External Leakage	%	5	5
Burner Maximum Temperature	K (°R)	1478 (2660)	1536 (2765)
Turbine Rotor Inlet Temperature	K (°R)	1478 (2660)	1478 (2660)
Gas Generator Pressure Ratio		2.94	3.03
Gas Generator Turbine Adiabatic Efficiency	%	87.5	87.6*
Power Turbine Pressure Ratio		3.06	2.97
Power Turbine Adiabatic Efficiency	%	83	83
Overall Turbine Efficiency	%	86.8	87.0
Overall Turbine Specific Heat Ratio		1.31	1.31
Gas Generator Mechanical Efficiency	%	98	98
Output Gearbox Efficiency	%	98	98
Exhaust & Interstage Duct Pressure Loss	%	5	5
Output Power	kW (hp)	242 (324)	234 (314)
Fuel Consumption	kg/hr (lb/hr)	76.4 (168.5)	75.9 (167.5)
Specific Fuel Consumption	kg/kW-hr (lb/hp-hr)	0.316 (0.52)	0.324 (0.532)
Rotational Speed	rpm		71,222

* Apparent adiabatic values from pressure ratio and enthalpy change

TABLE II - HIGH TEMPERATURE CYCLE PARAMETERS

Parameter	Units	Values		
Turbine Inlet Temperature	K (°R)	1478 (2660)	1589 (2860)	1700 (3060)
2nd Stage Temperature Rise	K (°R)	8.3 (15)	11.1 (20)	13.9 (25)
Tip Leakage	%	7	7	7
External Leakage	%	5	7	9
Compressor Pressure Ratio		10	10	10
Compressor Efficiency	%	77.5	76.8	76.2
Burner Maximum Temperature	K (°R)	1536 (2765)	1655 (2980)	1775 (3195)
Gas Generator Pressure Ratio		3.03	2.84	2.68
Gas Generator Turbine Efficiency	%	87.6	88.2	88.8
Power Turbine Pressure Ratio		2.97	3.17	3.36
Power Turbine Efficiency	%	83.0	82.0	81.0
Overall Turbine Efficiency	%	87.0	86.6	86.1
Output Power	kW (hp)	234 (314)	262 (352)	288 (386.6)
Specific Fuel Consumption	kg/kW-hr (lb/hp-hr)	0.323 (0.532)	0.325 (0.534)	0.327 (0.538)

Compressor Performance

The 10:1 pressure ratio, two-stage centrifugal compressor to be used for the monorotor engine was a scaled version of the compressor developed by Solar for USA AMRDL. The measured performance of this compressor with "zero" clearance (abradable shroud rubbing operation) was as follows:

Pressure Ratio	10.0
Efficiency ($\gamma = 1.395$)%	80
Airflow, kg/s (lb/sec)	0.794 (1.75)
Rotational Speed, rpm	76,137

The compressor was to be scaled by a factor of $(2.0/1.75)^{0.5}$ to achieve the design flow rate of 0.91 kg/s (2.0 lb/sec). Cycle analysis, including the effects of 8.3 K (15°R) heat transfer from the turbine to the second-stage compressor, showed that the second-stage discharge temperature would increase likewise, resulting in an apparent reduction in overall adiabatic compressor efficiency to 77.5 percent at an average specific heat ratio γ of 1.393.

For the second-stage compressor to deliver the same pressure ratio of 2.5 with heat transfer, it would be necessary to increase its corrected tip speed such that the work factor, q = 0.71, would be maintained. This was calculated to require an increase in corrected tip speed from 381 to 391 m/s (1250 to 1284 ft/sec) and will be effected by increasing the tip diameter 2.7 percent.

Compressor performance parameters for the baseline AMMRDL and scaled monorotor configurations are shown in Table III. To deliver design flow and pressure with 8.3 K (15°R) heat transfer into the second stage, it will be necessary to design with a rotational speed of 71,222 rpm.

Normalized compressor performance is shown on Figure 4, which indicates the estimated effect of heat transfer. The engine equilibrium operating line is seen to pass through the island of peak efficiency and provide a substantial surge margin at all anticipated operating speeds.

A computer internal flow analysis of the second-stage impeller was completed to acquire flow path pressure and temperature data for the thermal network model.

Gas Generator Turbine

Tradeoff studies were made on a baseline NASA gas generator radial inflow turbine to optimize its geometry for operation as a monorotor with the baseline two-stage compressor. The turbine rotor was originally designed so that the specified blade thickness would allow internal cooling passages without excessive manufacturing cost. The design distribution of blade normal thickness is shown on Figure 5 and reached a maximum of 0.76 cm (0.30 in.) along the hub line to a minimum of 0.23 cm (0.09 in.) at the exducer tip. A compromise of the design blade geometry was permissible to facilitate cooling or alleviate stress or other mechanical problems.

The critical temperature region of the monorotor turbine blade was anticipated to be along the outer stream-tube; thus large blade thicknesses would promote

TABLE III - COMPRESSOR DESIGN PARAMETERS

Scale Factor on Baseline Compressor $= \sqrt{\frac{2.0}{1.75}} = 1.069$

$\gamma = 1.393$

Parameter	Units	Baseline	Monorotor
1st Stage			
Inlet Temperature	K (°R)	288 (520)	288 (520)
Inlet Pressure	Pa (lb/in^2)	101E+03 (14.7)	101E+03 (14.7)
Corrected Tip Speed	m/s (ft/sec)	511 (1681)	511 (1681)
Tip Diameter	cm (in)	12.9 (5.062)	13.8 (5.412)
Corrected Airflow	kg/s (lb/sec)	0.79 (1.75)	0.91 (2.0)
Pressure Ratio		4.0	4.0
Adiabatic Efficiency	%	81.0	81.0
2nd Stage			
Inlet Temperature	K (°R)	460 (828)	460 (828)
Inlet Pressure	Pa (lb/in^2)	405E+03 (58.8)	405E+03 (58.8)
Corrected Tip Speed	m/s (ft/sec)	381 (1250)	392 (1284)
Tip Diameter	cm (in)	12.1 (4.752)	13.3 (5.22)
Corrected Airflow	kg/s (lb/sec)	0.25 (0.55)	0.29 (0.63)
Pressure Ratio		2.5	2.5
Adiabatic Efficiency	%	84.0	79.6
Work Factor		0.710	0.710
Impeller Tip Static Pressure	Pa (lb/in^2)	744E+03 (108)	744E+03 (108)
Impeller Tip Exit Angle	deg	41	47
Overall			
Pressure Ratio		10	10
Adiabatic Efficiency	%	79.5	77.5
2nd Rotor Exit Temperature	K (°R)	619 (1115)	628 (1130)
Rotational Speed	rpm	76,137	71,222

heat conduction to the disc, providing the loss in aerodynamic performance was not unduly compromised by the large thickness.

Simplified estimates using the data from Figure 1 indicated that with a uniform burner exit temperature and no supplementary cooling, metal temperatures along the outer shroud could be as high as:

Turbine Inlet Temperature	K	1478	1589	1700
	°R	2660	2860	3060
Max. Metal Temperature	K	961	1072	1183
	°R	1730	1930	2130

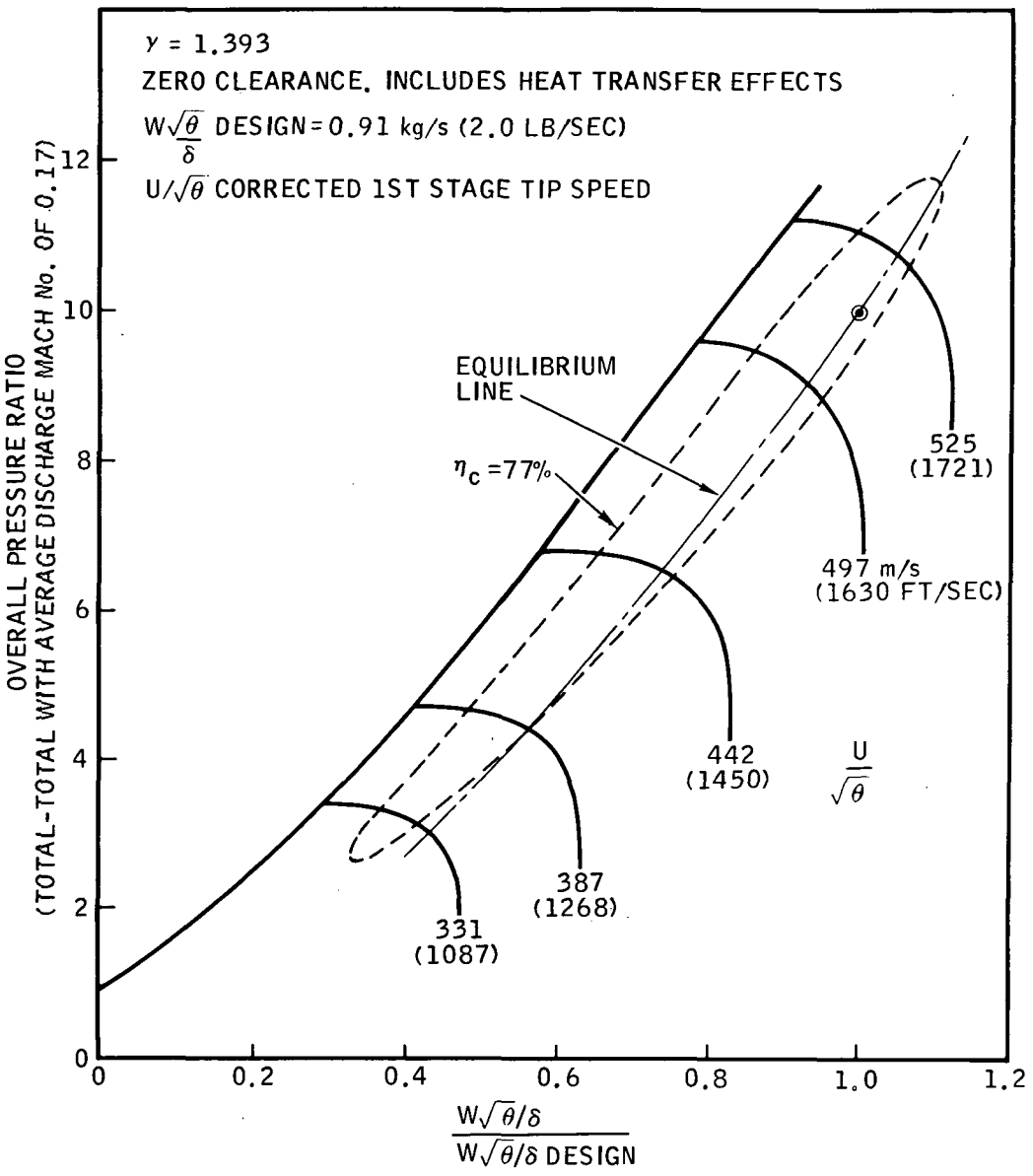

Figure 4 - Estimated Compressor Performance

Supplementary cooling is therefore mandatory at the higher turbine inlet temperatures.

Although increasing turbine inlet temperature reduces the gas generator turbine pressure ratio, rotor tip gas momentum (with zero exit swirl) must remain unchanged to provide constant compressor power. As a consequence, the rotor tip static pressure will remain essentially unchanged and rotor tip leakage will be constant. To maintain zero exit swirl, however, a change in exducer geometry from the baseline NASA configuration would be required.

The baseline NASA turbine configuration is shown in Figure 5 and features a rotor with 12 thick blades and a relatively large hub diameter to match an interstage

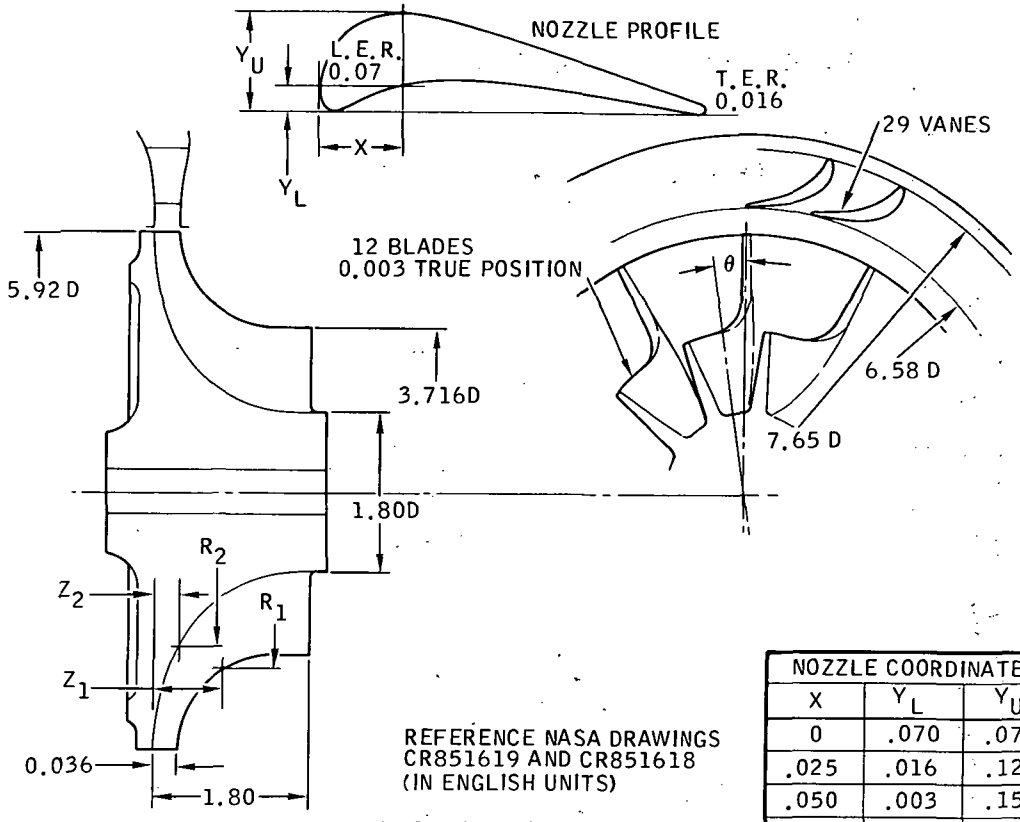

REFERENCE NASA DRAWINGS
CR851619 AND CR851618
(IN ENGLISH UNITS)

* NORMAL BLADE THICKNESS

ROTOR BLADE CAMBERLINE							
TIP				HUB			
Z_1	R_1	θ	N_1*	Z_2	R_2	θ	N_2*
.306	2.961	0	.094	0	2.961	0	.236
.306	2.889	0	.096	.001	2.858	0	.226
.309	2.800	0	.100	.008	2.652	0	.266
.318	2.700	0	.110	.028	2.448	0	.297
.336	2.600	0	.117	.067	2.243	0	.319
.365	2.492	0	.122	.131	2.047	0	.333
.414	2.370	0	.124	.215	1.858	0	.338
.485	2.252	0	.123	.316	1.678	0	.336
.576	2.143	0	.119	.435	1.510	0	.327
.686	2.052	0	.112	.575	1.357	0	.313
.810	1.980	0° 10'	.104	.733	1.223	0	.296
.943	1.926	0° 38'	.095	.906	1.112	0° 5'	.279
1.086	1.888	1° 37'	.085	1.093	1.023	1° 27'	.266
1.220	1.868	3° 24'	.085	1.289	.958	4° 27'	.259
1.365	1.860	6° 23'	.092	1.489	.918	9° 39'	.263
1.517	1.858	10° 34'	.102	1.593	.906	14° 23'	.308
1.658	1.858	15° 48'	.114	1.800	.900	21° 53'	.232
1.800	1.858	21° 53'	.070	1	–	–	–

NOZZLE COORDINATES		
X	Y_L	Y_U
0	.070	.070
.025	.016	.126
.050	.003	.155
.075	.000	.179
.100	.007	.198
.125	.016	.213
.150	.025	.223
.200	.040	.229
.250	.051	.227
.300	.058	.220
.350	.062	.209
.400	.063	.197
.450	.062	.183
.500	.059	.169
.550	.055	.154
.600	.050	.139
.650	.045	.124
.700	.038	.109
.750	.031	.094
.800	.024	.080
.850	.017	.068
.900	.010	.052
.950	.003	.040
.975	.000	.033
.993	.016	.016

MR205

Figure 5 - NASA Radial Turbine Geometry

power turbine duct arrangement. Integration of this design with the Solar second-stage compressor produces a monorotor geometry as shown on Figure 6 with a somewhat asymmetric disc profile that tends to induce compound bending stresses. The turbine tip diameter of the baseline NASA design is 15.04 cm (5.922 in.) compared with a second-stage compressor tip diameter of 13.25 cm (5.22 in.). Compressor tip static pressure is estimated at 744E +03 Pa (108 psia) which would increase to 786E +03 Pa (114 psia) at the 15.04 cm (5.922 in.) diameter with vaneless space diffusion. Estimated turbine rotor inlet static pressure was 572E +03 Pa (83 psia). Preliminary leakage studies of a three-lip labyrinth seal operating with these pressures showed that tip leakage could be as high as 7 percent with a radial clearance of 0.032 cm (0.0125 in.). Decreasing the turbine tip diameter to 14.7 cm (5.8 in.) was estimated to reduce compressor side seal entry pressure to 772E +03 Pa (112 psia) with a leakage of 7 percent. This would additionally reduce rotor stresses and weight at the expense of 0.5 percentage point reduction in turbine efficiency.

Cycle calculations showed that the gas generator radial flow turbine performance requirements at 1478 K (2660°R) inlet temperature to be as noted in Table IV. Assumed baseline adiabatic efficiency was 87.5 percent under zero heat transfer and zero tip flow conditions. Apparent efficiency with 8.3 K (15°R) heat transfer and 7 percent tip leakage is 87.6 percent, assuming a parallel flow turbine model in which the leakage flow enters the turbine rotor with a total pressure equal to the nozzle exit static pressure and a temperature equal to that of compressor discharge.

TABLE IV - GAS GENERATOR TURBINE PERFORMANCE

Parameter	Units	Values
Nozzle Inlet Flow	kg/s (pps)	0.82 (1.81)
Nozzle Inlet Total Temperature	K (°R)	1536 (2765)
Nozzle Inlet Total Pressure	Pa (psia)	962E +03 (139.7)
Rotor Inlet Flow	kg/s (pps)	0.88 (1.944)
Rotor Inlet Total Temperature	K (°R)	1478 (2660)
Pressure Ratio		3.03
Apparent Total Temperature Drop	K (°R)	292 (526)
Average Specific Heat Ratio		1.300
Output Power	hp	420
Datum Adiabatic Efficiency	%	87.5
Apparent Adiabatic Efficiency	%	87.6
Rotational Speed	rpm	71,222
Tip Diameter	cm (in.)	14.7 (5.8)
Tip Speed	m/s (ft/sec)	549 (1802)
Velocity Ratio		0.60
Exit Temperature	K (°R)	1186 (2134)

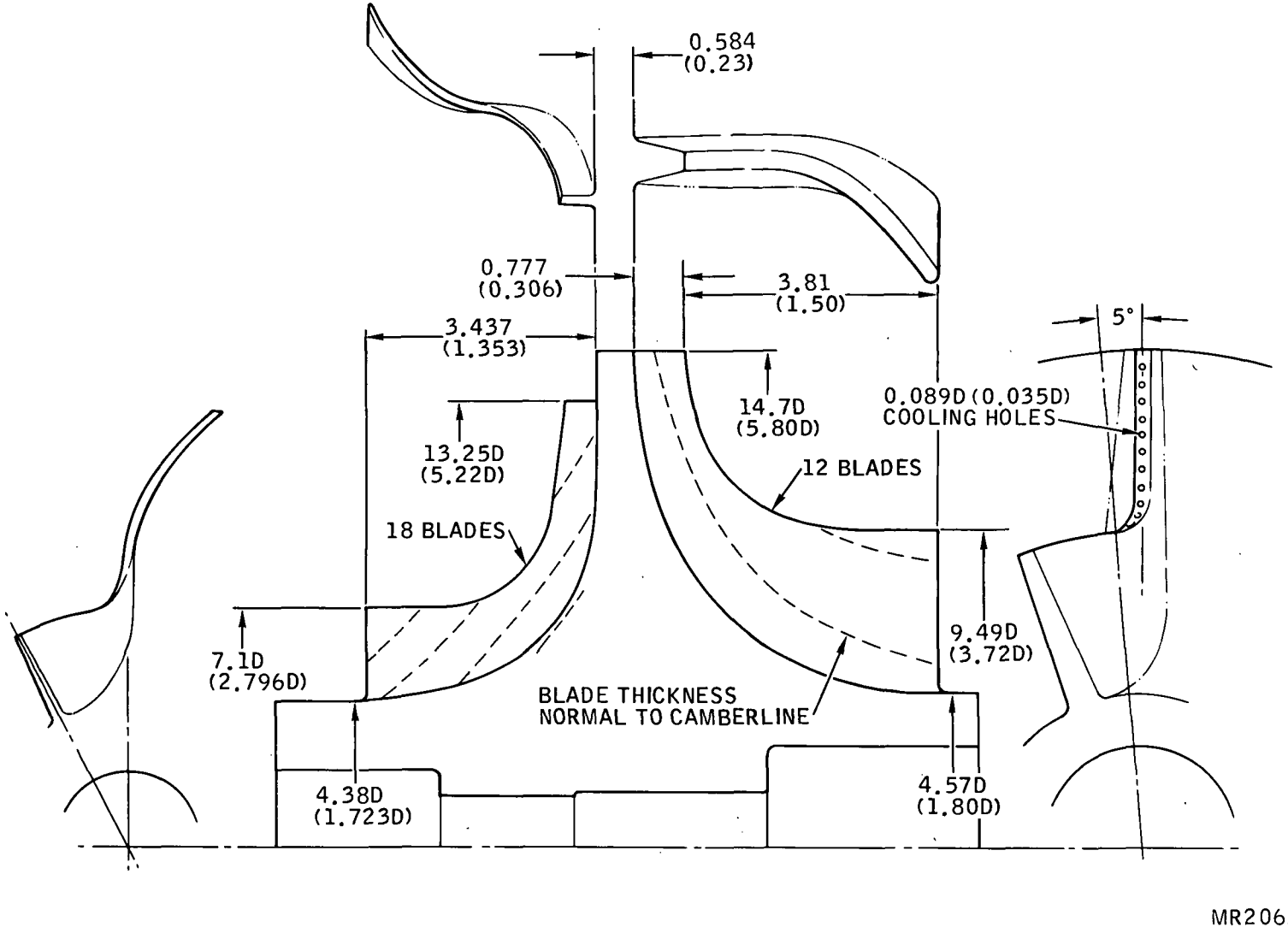

Figure 6 - Monorotor Baseline Geometry

Preliminary Design Configuration

Initial engine design studies revealed that it would not be practical to provide a satisfactory front drive arrangement within the confines of the existing Solar two-stage compressor design, because of the relatively small hub diameters. With the approval of NASA, it was elected therefore to proceed with a rear end output drive from the power turbine. The engine design was further complicated when interspan or straddle-mounted bearing systems were considered. Thus, an alternate overhung gas generator dynamic system was investigated.

Figure 7 shows a cross-section of the proposed preliminary engine configuration with the complete gas generator rotor cantilever-mounted from a front end bearing capsule. The first-stage compressor and monorotor are mated with a curvic coupling and held axially against the aft bearing race by the shaft torque nut. The two angular-contact ball bearings are axially preloaded and retained in an oil-damped capsule in similar manner to the Solar two-stage compressor turbo-drive rig. Dynamic studies of this overhung configuration showed only one critical speed in the engine operation range, at 12 percent design speed. Operation at this speed would result in a maximum radial excursion at the monorotor exducer of 0.031 cm (0.012 in.). Although this amount of rotor overhang appears excessive by gas turbine practice, a similar system is used on a commercially available, three-stage centrifugal air compressor.

The preliminary engine is assembled by an axial stack-up of the rotors and casings commencing with the first-stage compressor inlet housing. The monostator is attached after the monorotor and is axially bolted to the second-stage compressor front shroud. The monostator, consisting of the compressor diffuser, central plate, turbine nozzle vanes and aft shroud, will eventually be a single-piece casting.

A reverse-flow axial combustor is depicted, together with an uncooled single-stage axial power turbine. The axial power turbine is shown to discharge into a radial collector exhaust stack.

Dynamic analysis of the rotating assembly was completed with the rotors and shaft coupled to form a series of masses that respond as an integral assembly. The assembly is supported by flexible bearings and mounts.

A critical speed analysis was conducted which indicated that with two bearing spans and bearing stiffnesses in the range 3.6 to 18E +04 kg/cm (0.2 to 1.0E +06 lb/in), only one critical speed occurred in the operating speed range 0 to 120 percent design speed. Dynamic test data from the Solar two-stage compressor rig indicated that the bearing stiffness for the two preloaded angular-contact M204 ball bearings was of the order 18E +04 kg/cm (1.0E +06 lb/in). Using this bearing stiffness and a bearing span of 9.65 cm (3.8 in.), the first critical speed was calculated to occur at 8400 rpm (12 percent design speed).

An imbalance distribution was applied along the rotor span with light damping at the two bearing locations. Imbalance loads of 0.00025 cm/kg (0.003 in./oz) were imposed at two planes of the two rotors.

A single critical speed was calculated at 8400 rpm, with a computed steady-state running exducer radial excursion of 0.031 cm (0.012 in.). During actual transient start

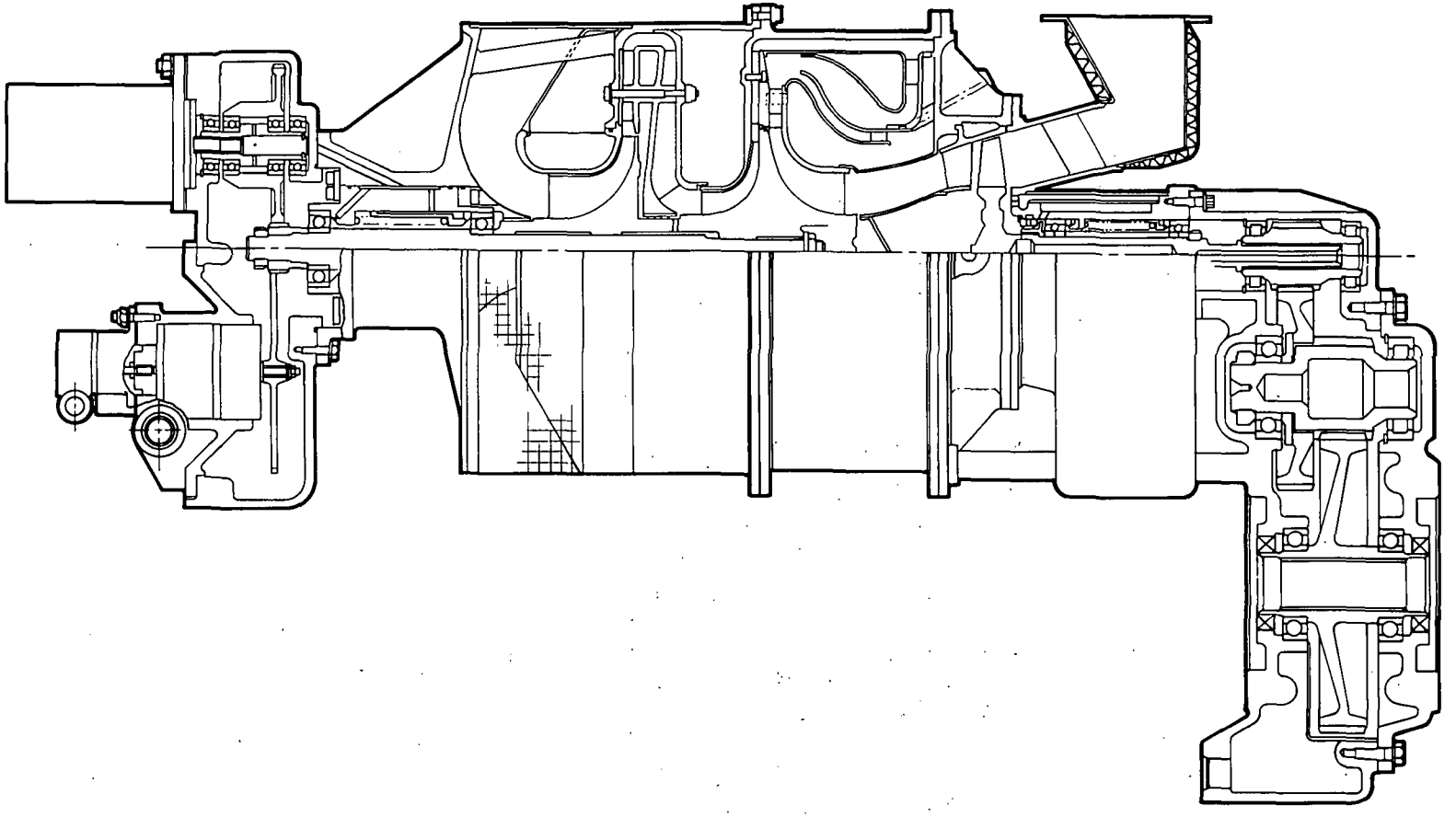

Figure 7 - Preliminary Engine Cross Section

conditions with an acceleration rate of the order 3000 rpm/sec, radial excursion would be less than 0.031 cm (0.012 in.). Maximum steady-state imbalance bearing load was estimated to be 154 kg (340 lb).

Preliminary Monorotor Thermal Analysis

Several thermal modes were made for the purpose of making the different thermal analyses. The basic model was two-dimensional (2D) in the sense that only radial and axial rotor and blade temperatures were calculated (i.e., no circumferential temperature variations), but 3D in the manner in which blade convection was accounted for. Metal node-to-node conductances were based on a complete (360°) rotor and the thicknesses of 18 compressor blades and 12 turbine blades, with the temperature-dependent thermal conductivity of INCO 718. The following boundary conditions were used:

- The shaft was given a 379 K (682°R) (vertical surface) temperature in a plane through the center of the first-stage compressor.
- The front of the rotor, through the spline coupling, is connected to a 478 K (860°R) sink taken at the aft face of the first-stage rotor.
- Adiabatic surfaces were used at the rotor tip seal, the rotor aft face and ID, and all blade tips.
- Turbine gas and compressor air convection on rotor and blade surfaces.

Convective heat transfer coefficient correlations are summarized below:

Part	Expression
Rotor disc surface, compressor and turbine, and outer shroud of the turbine	$N_{Nu} = 0.021\, N_{Re}^{0.8}\, N_{Pr}^{0.6}$
Compressor and turbine blades	$N_{Nu} = 0.0296\, N_{Re}^{0.8}\, N_{Pr}^{0.33}$
Rotor tip surface between compressor exit and diffuser inlet, stator surface between nozzle exit and turbine inlet, the surface downstream of the diffuser vanes to exit guide vanes	$N_{Nu} = 0.037\, N_{Re}^{0.8}\, N_{Pr}^{0.333}$
Diffuser vane channel walls, exit guide vane channel walls, nozzle vane channel walls	$N_{Nu} = 0.023\, N_{Re}^{0.8}\, N_{Pr}^{0.4}$

No film cooling effectiveness was allowed for the 7 percent rotor tip seal leakage. Because of the high convection heat transfer coefficients, radiation was not included.

As thermal results from the basic model were being obtained, it was decided that simple, internal convection cooling of the rotor and turbine blades could help alleviate the thermal stress problem. Accordingly, a separate thermal model was prepared for just such studies. The locations of the 0.089 cm (0.035 in.) diameter cooling air holes are shown in Figure 6. They were spaced 0.254 cm (0.10 in.) apart, the farthest one at 7.11 cm (2.8 in.) radius, with the exception of two holes on every other turbine blade to avoid compressor blade interference. Thus, the model averaged nine cooling air holes per turbine blade. It was intended to Elox these holes, which vary from 1.4 to 3.05 cm (0.55 to 1.2 in.) long. The estimated cooling flow rate through the holes totaled 4.9 percent of the compressor flow.

In the turbine blades, the cooling air has a uniform local effect and no "surface" nodes are required. However, in the disc, the circumferential distance from blade-to-blade in the region of the cooling holes is such that the metal conductances are on the order of the cooling air hole conductances, and here surface nodes are required. Accordingly, taking advantage of blade-to-blade symmetry, a 1/24 "pie" section 3D model was constructed utilizing almost all the capacity of the thermal analyzer program.

Results of the baseline geometry analysis are shown on Figure 8 for the various turbine inlet temperatures studied. As would be expected, the dominant rotor thermal gradients are in the axial direction; for the blades, they are in the hub tip direction. The sharpest gradients occur at the blade hubs. In spite of a nearly 111 K (200°R) inlet-to-outlet gas temperature drop, turbine rotor blades are cooler at the inlet than outlet, due to greater heat transfer through the thinner disc. For analogous reasons, compressor blade temperatures increase from inlet to outlet. When these results are integrated, it can be observed that the rotor hub, radially inward of the compressor blades, is hotter than the compressor blades, whereas the reverse is true of the turbine blades.

Results of the analysis for compressor blades three times thicker than those of the baseline geometry (all other values the same) are shown in Figure 9 for a T.I.T. of 1478 K (2660°R).

Comparing these results to the 1478 K baseline geometry results, the compressor blades are 56 to 83 K (100° to 150°R) hotter at the rotor tip, (tending to reduce axial temperature gradients) and progressively less hot toward the inlet. On average, the hub is 8.3 K (15°R) cooler and some parts of the turbine blading 11.1 K (20°R) cooler.

Results of the analyses for the supplementary cooled monorotor are also shown on Figure 8 for the various turbine inlet temperatures examined. In the region of the cooling air holes, significant temperature reductions are effected. For instance, for 1478 K (2660°R) T.I.T., average rotor temperatures are 72 to 86 K (130° to 155°R) lower and average turbine blade temperatures are 133 to 189 K (240° to 340°R) lower than the comparable uncooled design.

A disconcerting consequence of the cooling air holes, however, is the occurrence of rather large temperature differentials in the circumferential direction in the rotor. For the 1478 K (2660°R) case, typical cooling-hole-surface to rotor-average temperature differentials range from about 86 to 111 K (155° to 200°R) and are larger for the higher T.I.T. cases. Considering that the thermal model was only one (metal) node thick circumferentially, a more refined thermal model would be necessary if 3D stress considerations indicate such "thermal warping" is a problem.

TEMPERATURE CONVERSION																				
°F	500	600	700	800	900	1000	1100	1200	1300	1400	1500	1600	1700	1800	1900	2000	2100	2200	2400	2600
°R	960	1060	1160	1260	1360	1460	1560	1660	1760	1860	1960	2060	2160	2260	2360	2460	2560	2660	2860	3060
K	533	588	644	700	756	811	867	894	977	1033	1088	1144	1200	1255	1311	1367	1422	1477	1532	1588

NOTE: TEMPERATURE GRADIENTS SHOWN ARE °R. REFER TO TABLE FOR K AND °F.

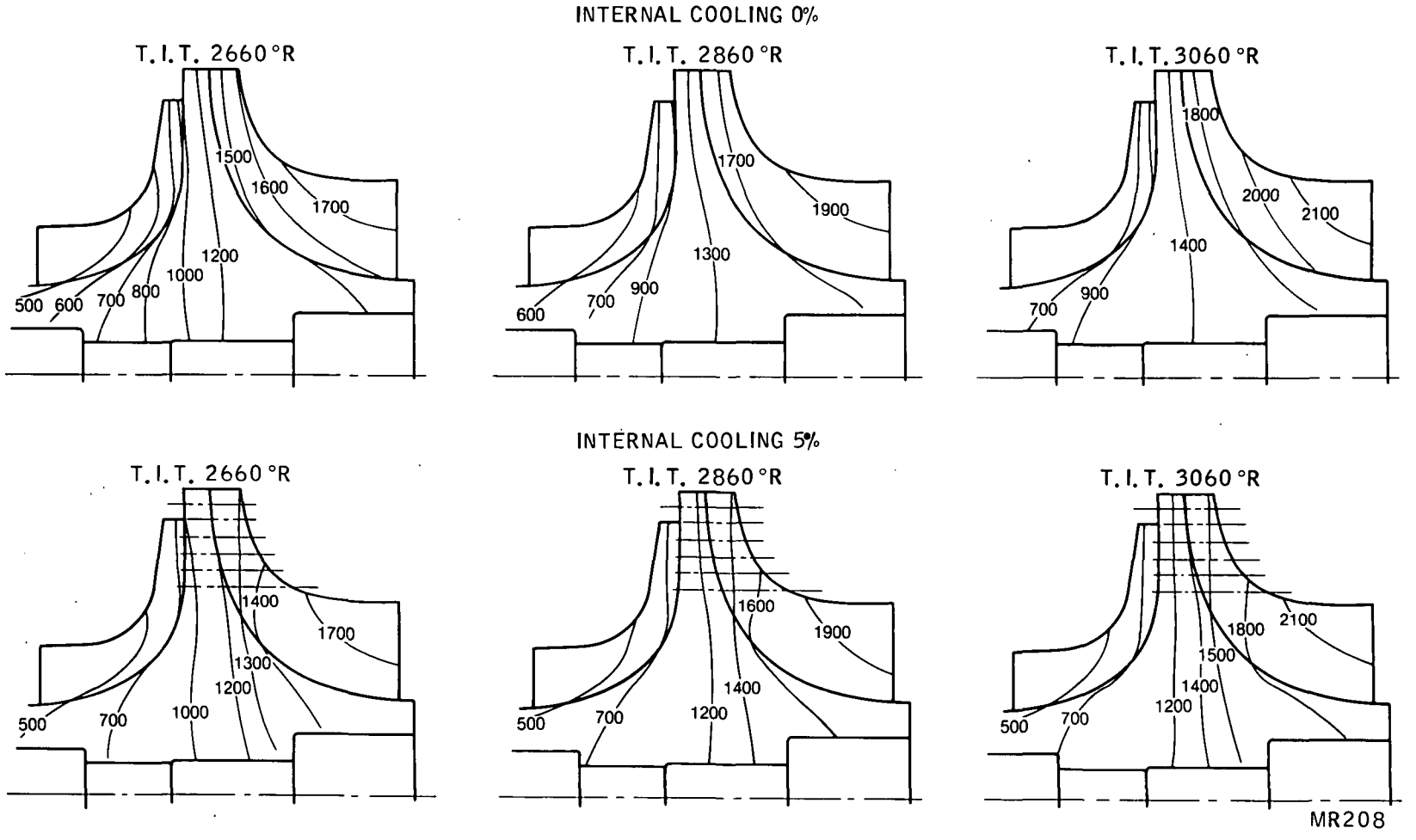

Figure 8 - Monorotor Temperature Distributions

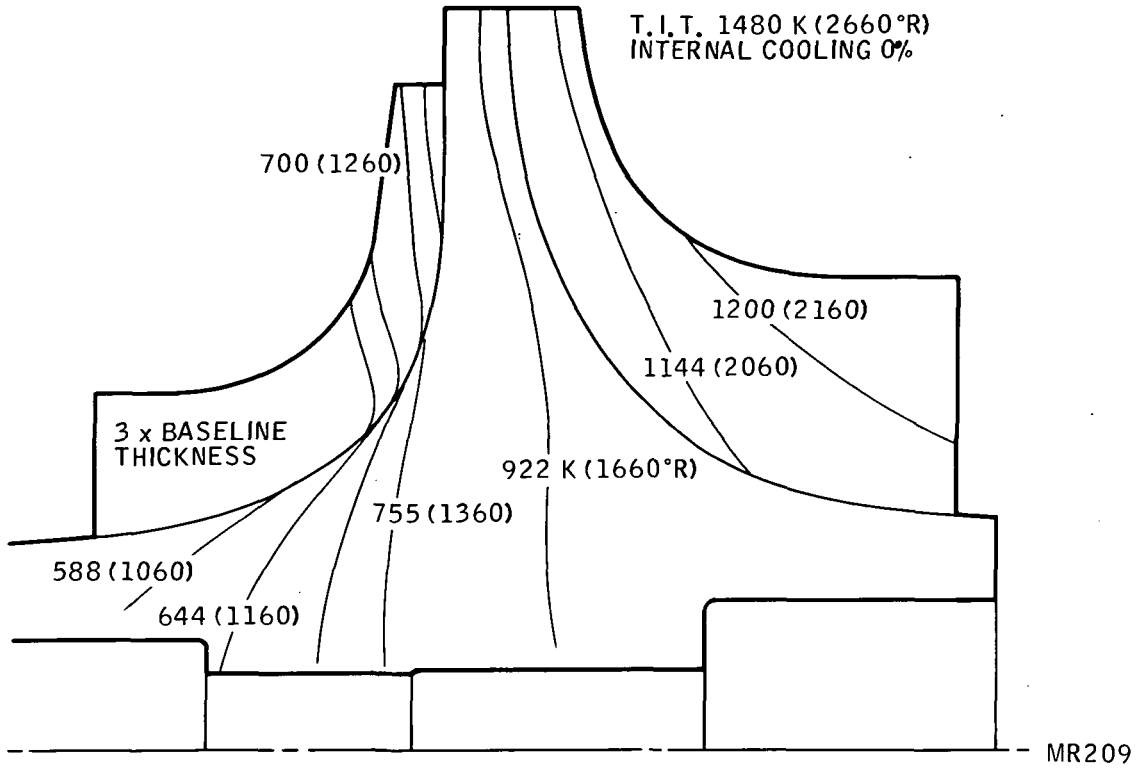

Figure 9 - Monorotor Temperature Distribution (Thick Compressor)

Preliminary Stress Analyses

Previous stress analyses of monorotor configurations had shown that large thermal stresses are generated in the compressor blade due to relatively high temperature gradients with direct conduction cooling. It was recognized that with non-radial elements in the compressor blade it would be necessary to utilize a three-dimensional (3D) finite stress analysis to obtain quantitative stress information. A preliminary 3D model was generated therefore for the baseline monorotor geometry comprising the Solar second-stage compressor and NASA radial inflow turbine geometries with a central disc of tip thickness 0.58 cm (0.23 in.).

Steady-state stresses were determined both with and without the thermal analyzer temperature gradients applied at the design speed with an average mixed rotor inlet temperature of 1478 K (2660°R).

The 3D model boundary is shown in Figure 10 and is a sector encompassing three compressor blades and two turbine blades. Initially, modeling revealed a danger of excessive bandwidth; thus, it was necessary to adopt relatively coarse elements within the central portion of the disc. Several computer runs were made, first with the baseline geometry and a normalized temperature gradient (based on previous monorotor thermal studies), followed by runs with thermal analyzer data applied and baseline blade thickness changed by a common multiple. All runs showed higher stresses than anticipated in the compressor blade, peaking to 1240E +06 Pa (180 ksi). Typical average 3D stresses are shown in Figure 11 with the temperature gradient applied.

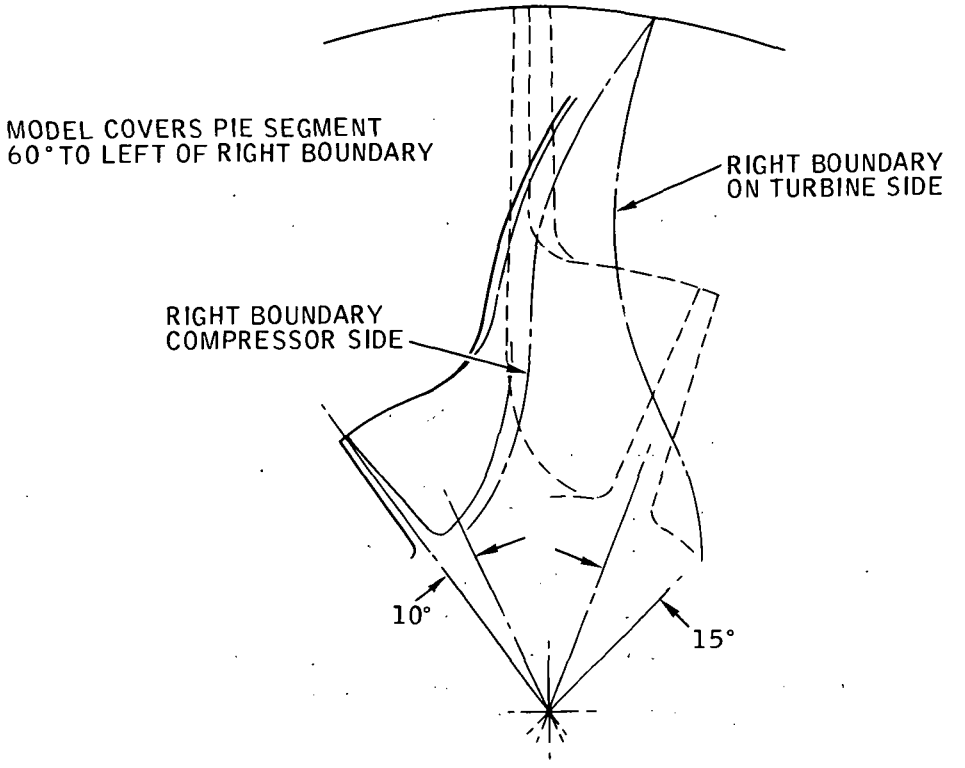

Figure 10 - Preliminary 3D Finite Element

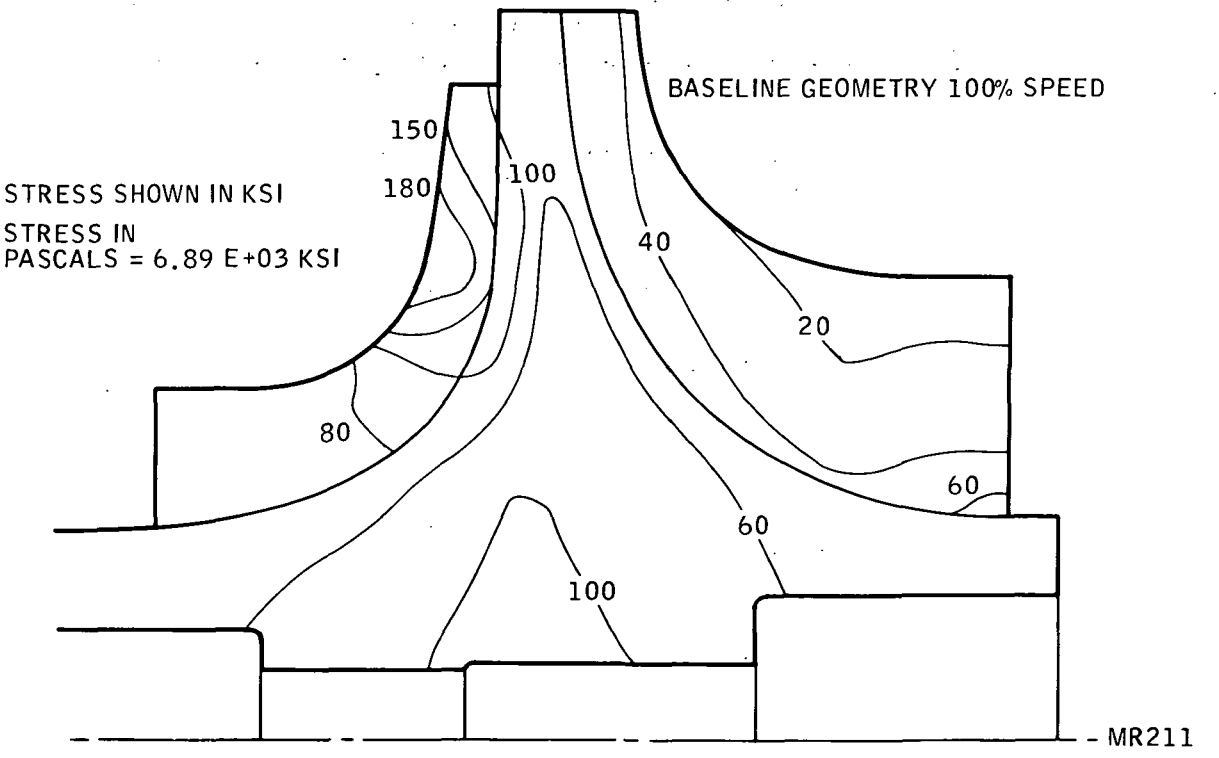

Figure 11 - Preliminary 3D Stresses, Baseline Geometry

Maximum stresses for some elements were 25 percent greater than average due to circumferential stress variations apparently arising from blade loading effects.

Comparative runs between 2D and 3D models were made, and although peak compressor blade stresses differed by 207E +06 Pa (30 ksi) (due to additional 3D model bending stresses), the average stress levels indicated similar trends and assisted in pinpointing the root cause of the high compressor blade stress. Examination of the monorotor temperature distributions, Figure 8, shows that along the longest radial extension of the compressor and turbine blades there is a radial temperature decrease on the compressor and a radial temperature increase on the turbine. These radial temperature distributions result in tensile and compressive stresses which are added to the centrifugal blade stress on the compressor and turbine blades respectively. Providing such stresses do not exceed the yield strength, this situation is to be desired since turbine blade stresses under higher temperature conditions are reduced, whereas compressor blade stresses are increased but occur in a region of relatively low metal temperatures. Additionally, during transients from and to idle conditions, the monorotor disc may remain as hot as the blades, and a small stress reversal range could be experienced on the highly stressed compressor blade; consequently, actual localized yielding of the compressor blade could be permissible.

Analysis of compressor stress results indicated that with refinements to the blade thickness distribution and a symmetrical disc profile, it should be possible to lower both the centrifugal and thermal maximum stress to below the yield strength for high quality forged material.

Examination of Figure 11 shows a critical stress rupture life-limiting element in the turbine lies at the exducer trailing edge root where the maximum effective 3D stress is 415E +06 Pa (60 ksi) with a metal temperature of 1144 K (2060°R). In order to obtain increased life, it will be necessary to modify the exducer trailing edge geometry by increasing the blade thickness taper ratio, leaning the trailing edge from radial, and reducing the exducer axial length to lower blade temperature.

Disc overspeed burst margin can be determined from the average equivalent stress in the disc by the relationship

$$\frac{\text{Burst Speed}}{\text{Design Speed}} \% = 100 \sqrt{\frac{\text{U.T.S. Min}}{\text{Average Equivalent Stress}}}$$

With a minimum ultimate tensile stress of 898E +06 Pa (130 ksi) at 850 K (1710°R), average disc temperature and average equivalent stress of 416E +06 Pa (60 ksi) at design speed, the burst speed is given by:

$$\text{Burst Speed} = 100 \sqrt{136/60} = 147 \text{ percent Design Speed}$$

Preliminary Study Phase Conclusions

Preliminary analyses of the monorotor configuration revealed the following:

- Operation at a turbine inlet temperature of 1478 K (2660°R) with direct conduction cooling induces relatively high thermal stresses in the compressor blades and disc. These high thermal stresses are, however, conveniently in low metal temperature zones, and with further optimization of the blade thickness, it is anticipated that the stresses could be placed below the yield limit.

- A potential stress rupture zone exists at the root of the exducer trailing edge where metal temperatures reach their highest level. Further optimization of the trailing edge taper ratio and geometry is required to attain design life requirements.

- A convective internal cooling arrangement was studied for operation at turbine inlet temperatures of 1589 and 1700 K (2860° and 3060°R) using approximately 5 percent supplementary air cooling. Very effective cooling was obtained at the turbine tip entry, but high exducer metal temperatures could not be avoided. Additionally, the internal cooling scheme studied would create a circumferential temperature variation within the disc, compounding the thermal stress problem.

- Cycle performance studies at the higher turbine inlet temperatures showed no improvement in specific fuel consumption, and the possibility of worse sfc if size effects were considered.

- Monorotor stress analysis shows that a 3D stress model will be required to obtain a realistic stress analysis of the monorotor configuration.

- Tip leakage of 7 percent results in burner exit and mixed rotor inlet temperatures of 1536 K (2765°R) and 1478 K (2660°R) respectively, making nozzle cooling a difficult problem.

As a result of the aforementioned, it was decided with NASA program manager concurrence to select burner exit and mixed rotor inlet temperatures of 1516 K (2730°R) and 1422 K (2560°R) respectively during detail design, and to modify the NASA radial turbine and Solar second-stage compressor blade thickness to minimize blade thermal stresses and also to provide if possible a symmetrical disc profile.

DETAILED DESIGN

The detail design phase of the program called for completion of the final aerodynamic, thermal, and stress analyses and modification to the turbine blade and disc shapes to reduce internal stresses and temperature gradients. Detailed mechanical and dynamic design of the component test rigs with all detailed fabrication drawings and a list of parts to be fabricated was also to be completed.

A redesign of both the baseline Solar compressor and NASA turbine was therefore commenced with the objectives of favoring the blading design to suit thermal and dynamic stress considerations. A symmetrical center disc profile with a common blading hub diameter equal to that of the baseline compressor geometry was preferred. This disc profile resulted in slight decreases and increases in the baseline compressor an turbine meridional hub curvatures respectively.

The baseline turbine exducer annulus area was maintained, and the blade thickness distributions were modified slightly to increase the blade taper ratio. Although the baseline compressor leading blade thicknesses were maintained, thicknesses from approximately the 15 percent chord position were increased by a factor of 2 to 3 to both reduce thermal gradients and provide a more robust blade to withstand the potentially high localized stresses.

Revised blade thickness distributions for both the compressor and turbine are shown on Figure 12 and were used together with the revised disc profile for reexamination of the compressor and turbine aerodynamic performances discussed in succeeding paragraphs.

Second Stage Compressor Redesign

The most significant compressor changes to the baseline configuration affecting internal blade loading were an increase in blade thickness and an increase in average blade discharge angle. The effective blade discharge angle was recalculated using the cosine blade opening/pitch ratio rule and was found to increase from 40 to 47 degrees; blade exit height was therefore adjusted to maintain the design pressure ratio. Thermal flow studies were then conducted with the intent of selecting blade geometry and shroud profiles that would essentially provide blade loadings similar to the baseline design. It became apparent that a reduction in blade number from 18 to 16 was necessary to achieve similar loadings, primarily due to increased meridional velocities with the larger blade thicknesses.

Finalized shroud blade loadings for the baseline and redesigned second-stage compressors are shown on Figure 13 and indicate that aerodynamic design objectives were realized. Note that these loadings essentially influence the boundary layer growth, exit flow profile, and trailing edge mixing losses. Thus, while the influence

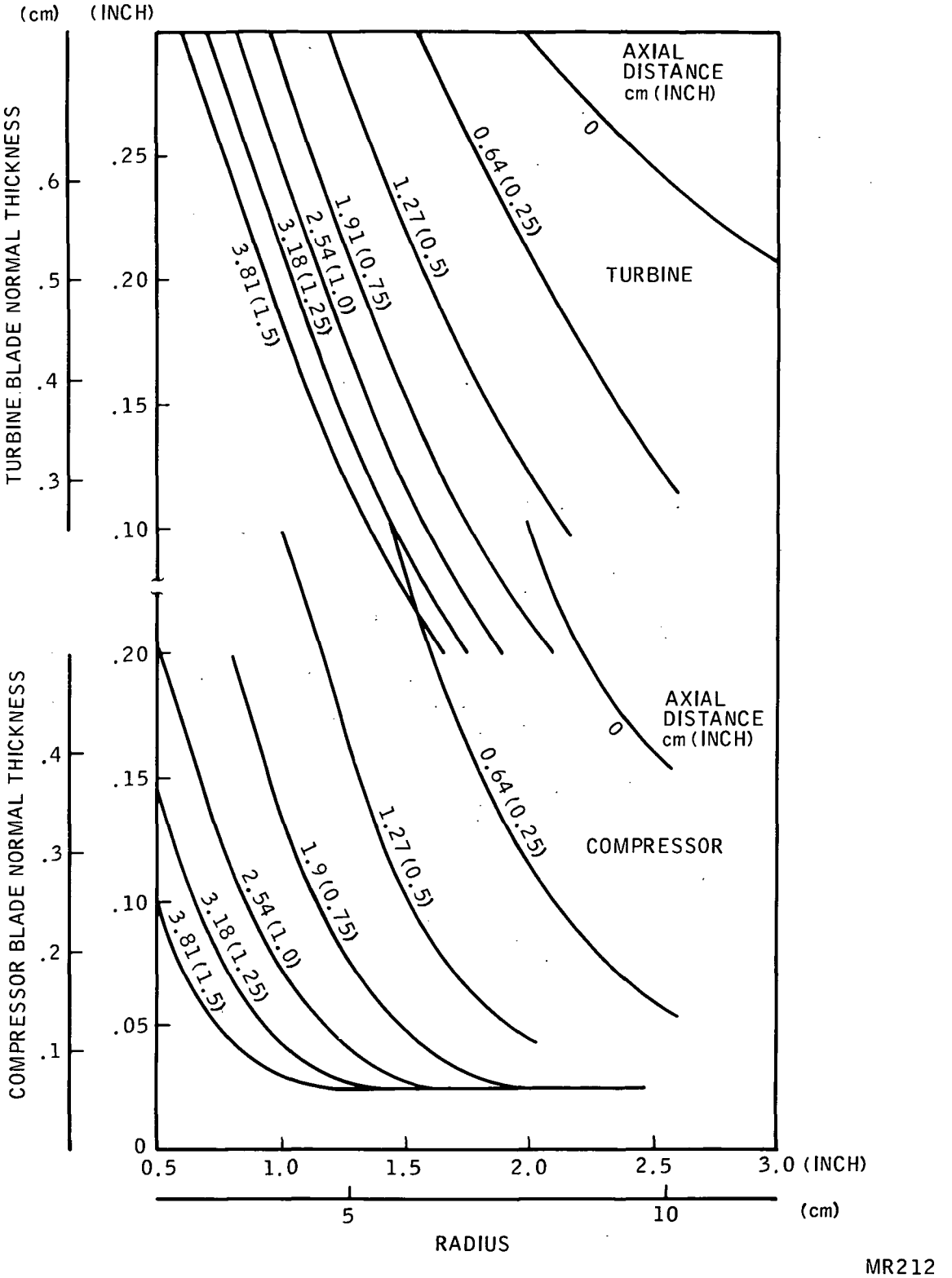

Figure 12 - Monorotor Blade Thicknesses

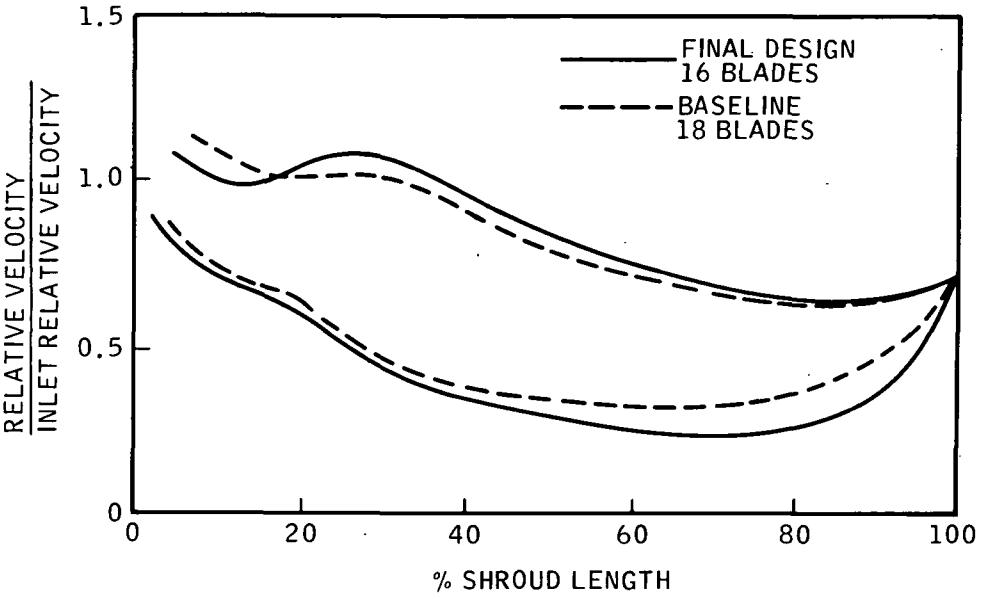

Figure 13 - Second-Stage Compressor Shroud Relative Velocities

of blade trailing edge thickness as such could not be analyzed directly, it is reasonable to expect that blading performances should be similar. Having generated the redesigned geometry, comparative performance studies were completed wherein the estimated efficiency of the redesigned compressor was within 1 percentage point of the baseline compressor, excluding the effect of larger trailing edge thickness. Design performance parameters for both compressor configurations are listed in Table V; compressor blade section profiles are shown on Figure 14.

TABLE V - SECOND STAGE COMPRESSOR DESIGN PARAMETER COMPARISON

Parameter	Units	Baseline	Redesign
Inlet Temperature	K (°R)	460 (828)	460 (828)
Inlet Pressure	Pa (lb/in^2)	405E +03 (58.8)	405E +03 (58.8)
Corrected Tip Speed	m/s (ft/sec)	381 (1250)	392 (1284)
Corrected Airflow	kg/s (lb/sec)	0.25 (0.55)	0.29 (0.63)
Pressure Ratio		2.5	2.5
Adiabatic Efficiency*	%	84.0	83.0
Work Factor		0.71	0.71
Tip Diameter	cm (in.)	12.1 (4.752)	13.3 (5.22)
Tip Width	cm (in.)	0.46 (0.18)	0.51 (0.20)
No. of Blades		18	16
Avg. Tip Thickness	cm (in.)	0.095 (0.037)	0.267 (0.105)
Avg. Exit Blade Angle	deg	40	47
Impeller Tip Static Pressure	Pa (lb/in^2)	744E +03 (108)	744E +03 (108)
Impeller Exit Temp	K (°R)	619 (1115)	628 (1130)
Diffuser Exit Temp	K (°R)	619 (1115)	655 (1180)

* Apparent adiabatic values from pressure ratio and impeller enthalpy change

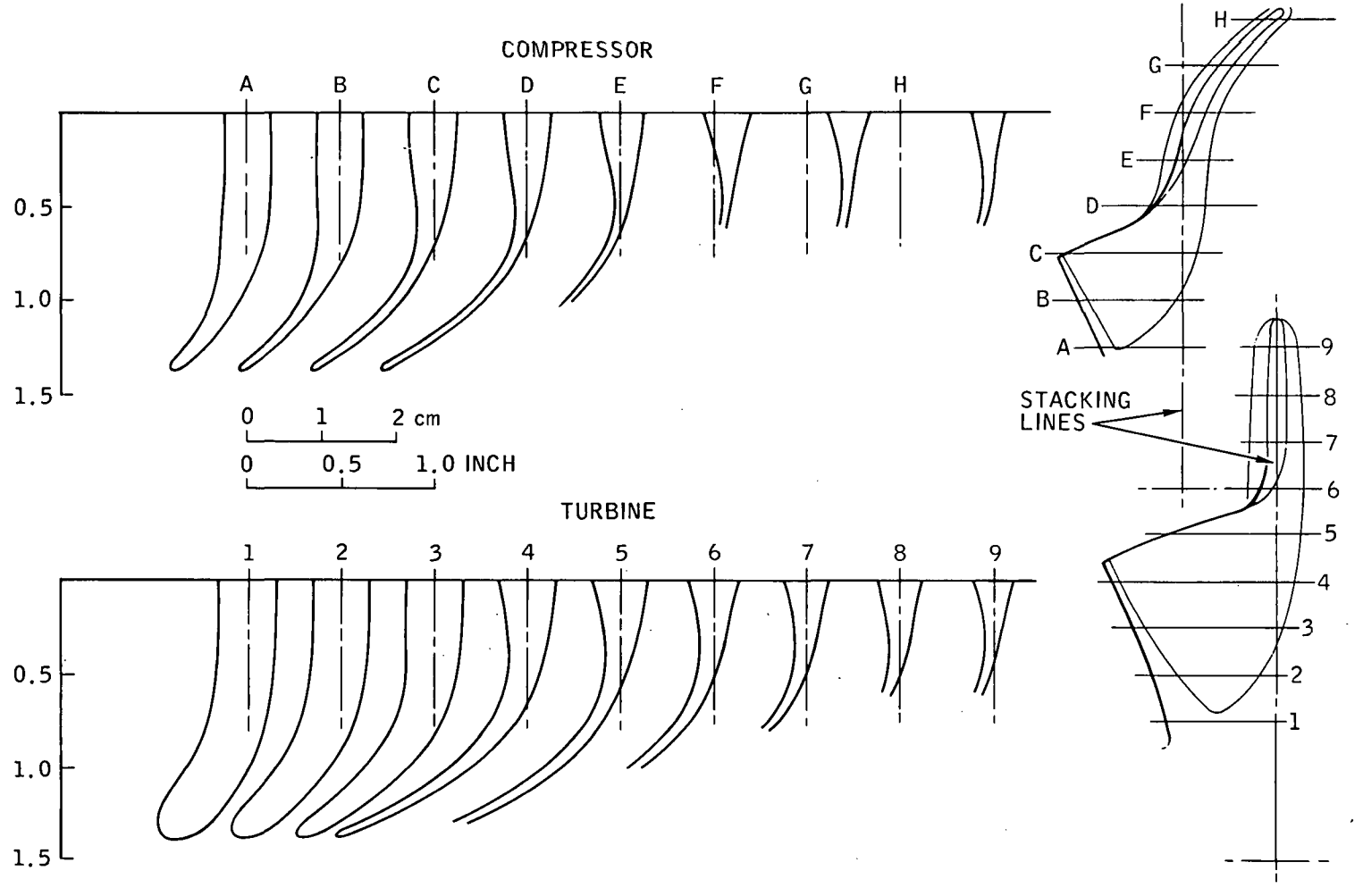

Figure 14 - NASA Monorotor Blade Geometry

Turbine Redesign

Thermal stress studies showed that metal temperatures peaked in the exducer tip and could, accordingly, be slightly reduced by decreasing the exducer tip diameter and axial chord. Accordingly, the following modifications to baseline rotor geometry were investigated:

	Baseline		Modified	
	cm	(in.)	cm	(in.)
Exducer Tip Diameter	9.45	3.72	9.14	3.6
Exducer Hub Diameter	4.57	1.80	4.37	1.723
Blade Axial Chord	4.57	1.80	3.77	1.487

Additionally, a mirror image compressor hub profile was selected with the revised distribution of blade thickness of Figure 12 to benefit centrifugal stresses.

Turbine performance studies incorporating these modifications were conducted to determine design features that would provide the best compromise between efficiency, stress, and tip leakage flow, as controlled by the compressor and turbine rotor tip static pressures. Computer optimized turbine adiabatic (total-total) performance for the revised geometry is shown on Figure 15, indicating an efficiency potential of 88.3 percent at the design velocity and pressure ratios of 0.614 and 3.04 respectively.

The estimated efficiency of 88.3 percent is based on nozzle and exducer (RMS) trailing edge thickness-to-throat opening ratios of typical Solar small radial turbine designs ranging from 0.254 to 0.38 cm (0.10 to 0.15 in.). Nozzle vane and blade thicknesses for the gas generator turbine were increased to 0.48 and 0.61 cm (0.19 and 0.24 in.) respectively to provide heat conduction to the "cold" sinks and internal cooling of the nozzle vane. Nozzle performance data from U.S. Avlabs Technical Report 68-69 indicated a possible reduction in turbine efficiency of the order 0.2 percent for the increased nozzle trailing edge thickness; no test data are available for the effect of exducer trailing edge thickness on radial turbine performance, but it is expected to be less sensitive than comparable size axial turbines. An overall adiabatic turbine efficiency of 87.5 percent was arbitrarily adopted to allow for the thicker trailing edge conditions.

The exducer effective blade leaving angle at the RMS section was determined assuming zero deviation between the relative air angle and cosine throat opening/pitch ratio. This required a RMS blade angle of 58 degrees. Radial element constraints thereby defined the rest of the exducer blading. Turbine blade section profiles are shown on Figure 14.

The optimized turbine geometric features were subsequently used to determine the internal blade loading patterns, shown on Figure 16, from the NASA "MERDIL" and T-Sonic" computer programs. A minor refinement to the blade tangential turning schedule was made in the vicinity of the bend from radial to axial in the course of these computer runs so that a smooth shroud loading progression could be obtained.

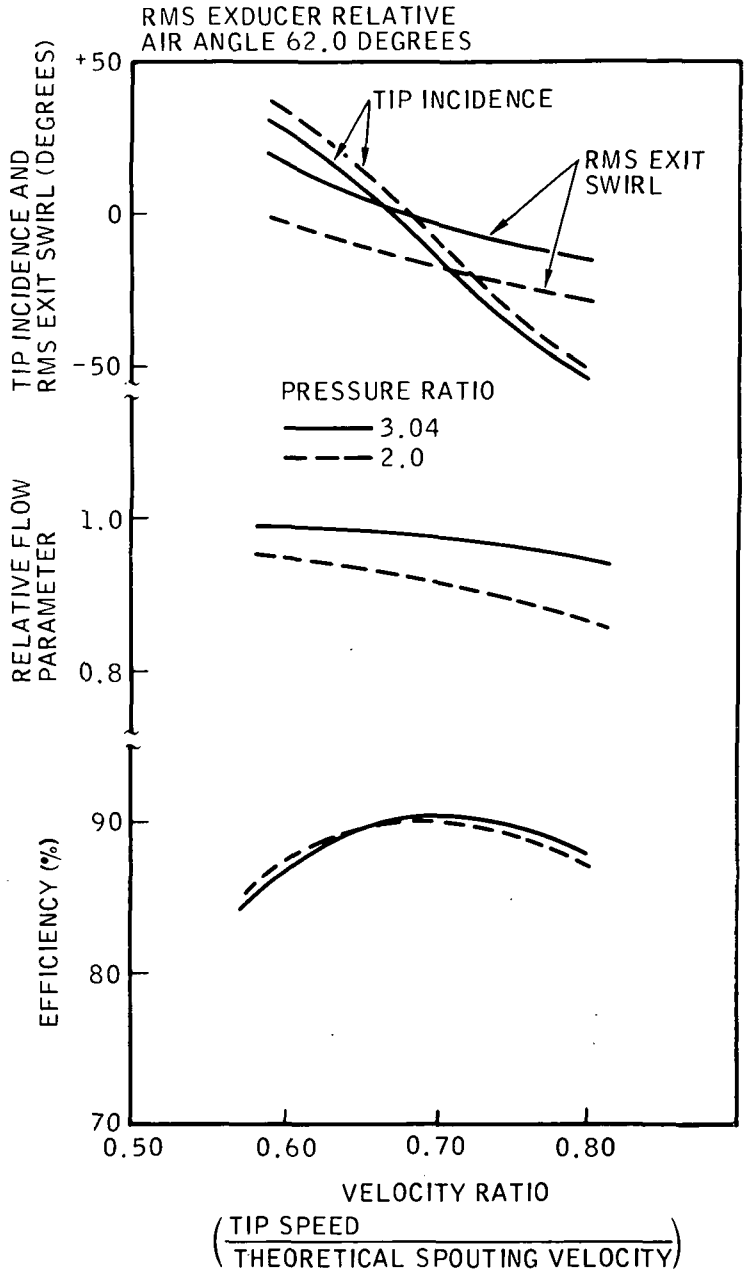

MR213

Figure 15 - Estimated Turbine Performance

Study of the baseline NASA turbine nozzle configuration revealed that it was desirable to increase the vane cross-sectional area to conduct more heat from the hotter aft shroud to the cooler central diaphragm, and at the same time, to reduce the vane number, thereby curtailing possible trailing edge thermal problems. The nozzle configuration shown in Figure 17 was therefore selected for thermal aerodynamic and stress studies of the monostator arrangement. This nozzle employs 17 vanes of similar profile to most Solar radial flow turbine nozzle designs and was anticipated to operate with an absolute inlet gas angle of 45 degrees, based upon typical swirl traverses from a reverse-flow combustor and centrifugal compressor.

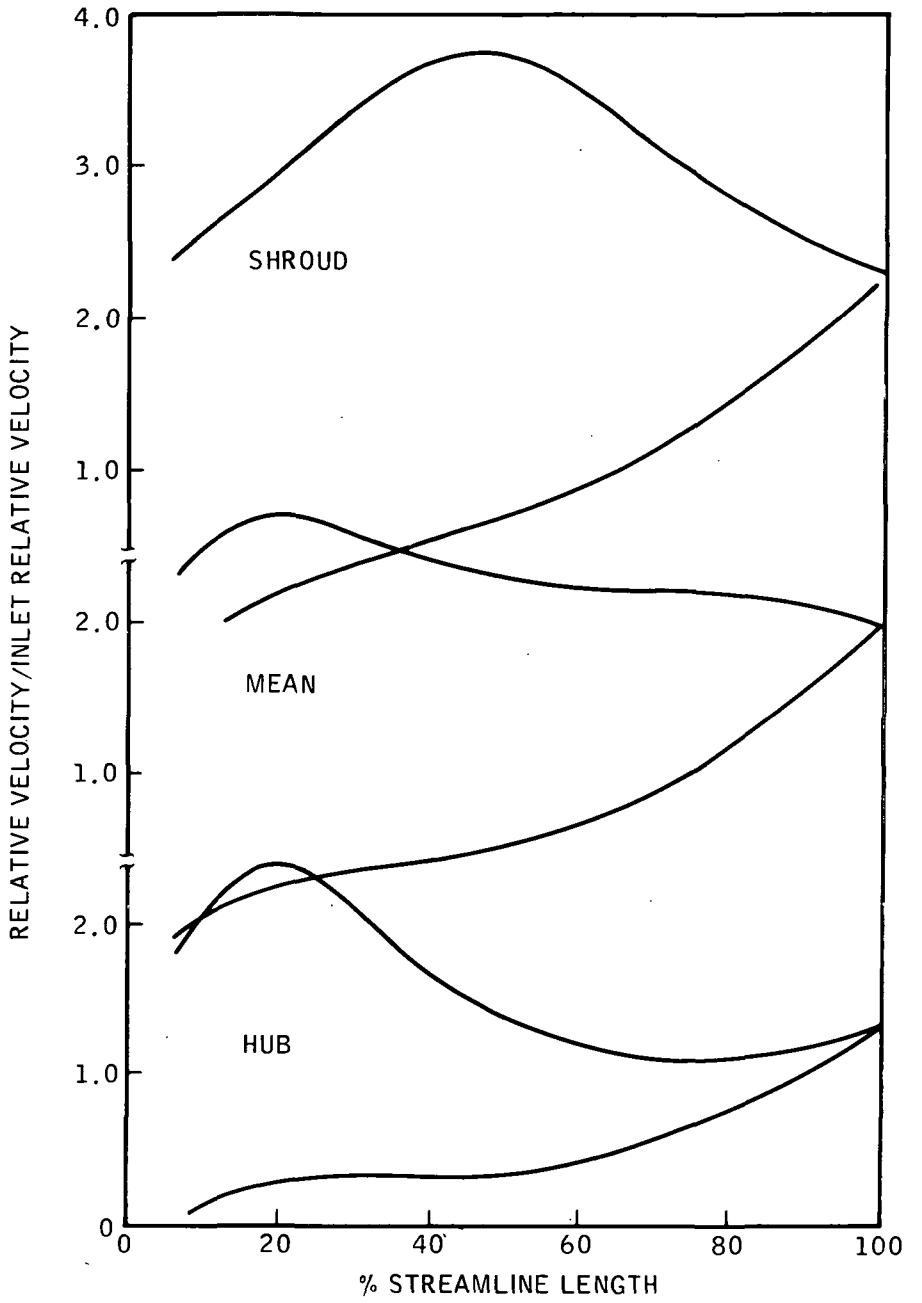

MR216

Figure 16 - Turbine Blade Relative Velocities

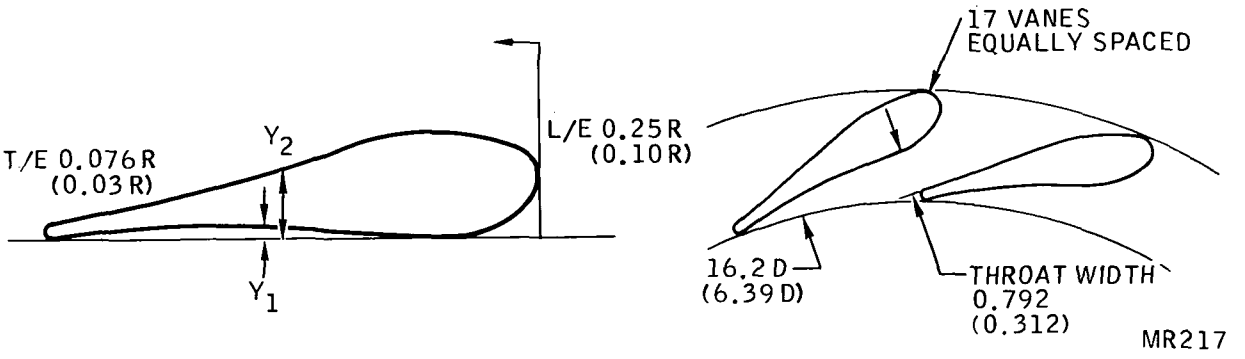

Figure 17 - Monostator Nozzle Redesign

Results of nozzle vane loading studies for this configuration are plotted on Figure 18, which shows an acceptable loading progression with positive velocities on all surfaces. Final determination and the appropriate nozzle vane height and total throat area depended on the last iteration of nozzle vane and shroud cooling flows.

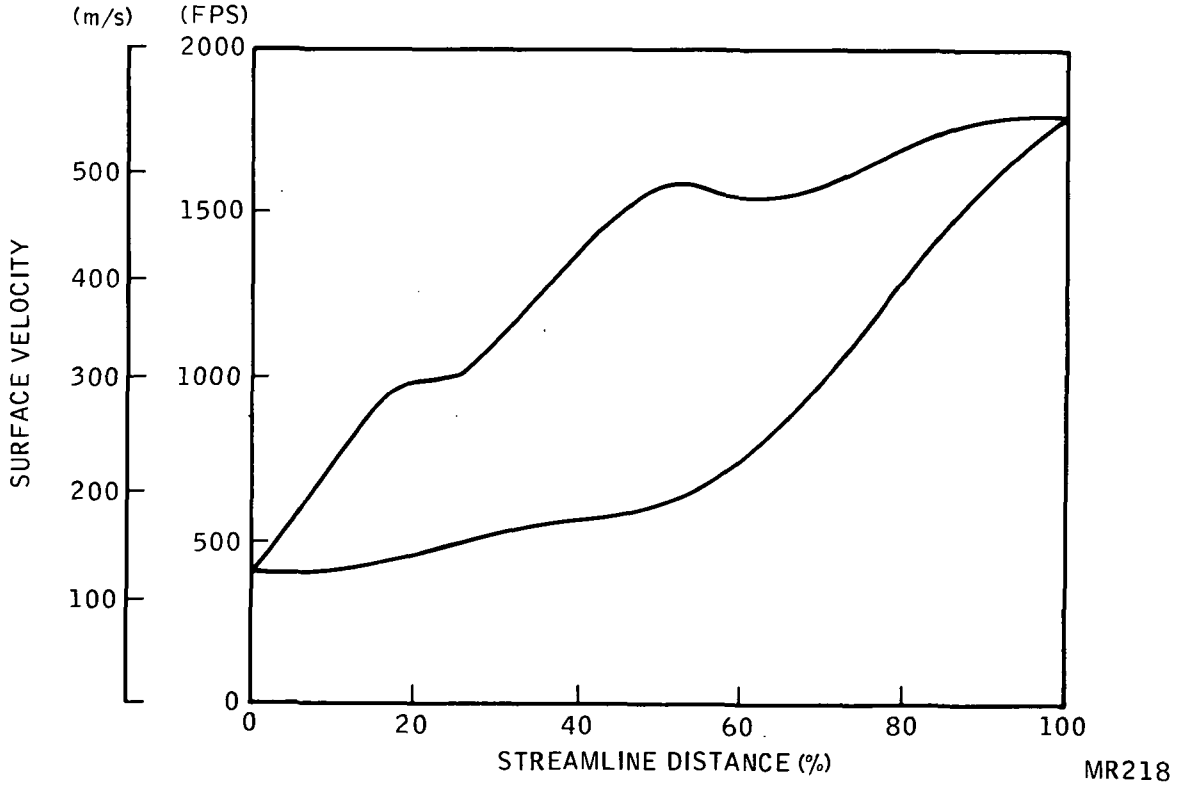

Figure 18 - Nozzle Vane Surface Velocities

Major performance parameters for the redesigned radial inflow gas generator turbine nozzle and rotor are listed in Tables VI and VII, assuming zero heat transfer and full flow through both the nozzle and rotor. The effects of monorotor tip leakage, combined with supplementary nozzle cooling flows, were treated in the cycle analysis routine, where both flows are assumed to have a momentum effectiveness at the turbine inlet of 75 percent compared to the core flow.

TABLE VI - MAJOR PERFORMANCE PARAMETERS OF GAS GENERATOR NOZZLE

Parameter	Units	Values
Throat Inlet Flow	kg/s (lb/sec)	0.864 (1.906)
Inlet Total Temperature	K (°R)	1516 (2730)
Inlet Total Pressure	Pa (lb/sq-in.)	962E +03 (139.7)
Inlet Gas Angle	deg	45.0
Vane Height	cm (in.)	0.698 (0.275)
Vane Number		17
Total Throat Area	sq cm (sq in.)	9.42 (1.46)
Exit Diameter	cm (in.)	16.3 (6.39)
Gas Leaving Angle (Rel. to radial)	deg	75.4
Throat Mach Number		0.79
Throat Static Pressure	Pa (lb/sq in.)	646E +03 (93.7)

Cycle Conditions

Final cycle conditions are listed in Table VIII and show an estimated output power and specific fuel consumption of 236 kW (317 hp) and 0.313 kg/kW-hr (0.514 lb/hp-hr) respectively. With the burner exit temperature fixed at 1517 K (2730°R), mixed rotor inlet temperature is 1422 K (2560°R). Note that a conservative increase in second-stage compressor temperature rise (due to monorotor heat transfer) of 8.3 K (15°R) was used, compared with final iteration heat transfer estimates of 6.1 K (11°R).

Estimated engine off-design performance under steady-state or equilibrium conditions is shown in Figure 19 plotted against an abscissa of compressor speed. The off-design characteristics are based on a fixed power turbine nozzle. Approximate idle speed would be 54 percent design speed assuming zero gas generator power take-off. Anticipated transient acceleration characteristics of the engine are shown on Figure 20 based on a fuel schedule modulated to provide a constant turbine exhaust temperature. Estimated start time to idle speed is 15 seconds. Acceleration time from idle to 100 percent speed is estimated to be 4.5 seconds.

TABLE VII - MAJOR PERFORMANCE PARAMETERS OF GAS GENERATOR TURBINE

Parameter	Units	Values
Rotor		
Mixed Inlet Temperature	K (°R)	1422 (2560)
Inlet Total Pressure	Pa (lb/sq-in)	940E +03 (136.4)
Inlet Static Pressure	Pa (lb/sq-in)	572E +03 (83)
Inlet Flow	kg/s (lb/sec)	0.93 (2.046)
Rotational Speed	rpm	71,222
Tip Diameter	cm (in.)	14.7 (5.8)
Tip Width	cm (in.)	0.71 (0.28)
Tip Speed	m/s (ft/sec)	551 (1802)
Inlet Incidence	deg	24
Exducer Tip Diameter	cm (in.)	9.32 (3.68)
Exducer Hub Diameter	cm (in.)	4.37 (1.723)
Exducer RMS Rel Air Angle	deg	62
Number of Blades		12
RMS Exit Swirl (against rotation)	deg	16
Overall		
Turbine Pressure Ratio (total-total)		3.04
Velocity Ratio (total basis)		0.614
Adiabatic Efficiency	%	87.5

Design Configurations

Two separate monorotor configurations were carried through concurrently in the mechanical design phase, i.e.:

- Control layout of complete small turboshaft engine with gas generator, power turbine gearbox, and accessories.
- Detailed design configuration of component test rig with separate compressor and turbine flow paths using a hot air supply at 978 K (1760°R).

The analytical design of the monorotor was directed toward obtaining the contract life and performance requirements for the complete engine, and as much as possible of the engine configuration was incorporated into the component test rig considering program limitations. For example, the complete shaft dynamic system and rotor assembly were identical, and while the stationary casings were designed for ease of fabrication and robustness, careful attention was paid to simulate engine airflow paths.

Engine Layout

Initial engine design studies revealed that it would not be practical to provide a satisfactory front drive arrangement within the confines of the existing Solar two-stage

TABLE VIII - NASA MONOROTOR DESIGN POINT

Parameter	Units	Values
Compressor Airflow	kg/s (pps)	0.91 (2.0)
Compressor Pressure Ratio		10.0
Compressor Adiabatic Efficiency	%	77.5
Compressor Specific Heat Ratio		1.393
Second Stage Compressor Heat Rise	K (°R)	8.3 (15)
Compressor Rotor Discharge Temp.	K (°R)	628 (1130)
Burner Pressure Loss	%	5
Burner Efficiency	%	98
Tip Leakage	%	7
Monostator Cooling Flow	%	5
Burner Maximum Temperature	K (°R)	1517 (2730)
Turbine Rotor Inlet Temperature	K (°R)	1422 (2560)
Gas Generator Pressure Ratio		3.04
Gas Generator Turb. Adiabatic Eff.	%	86.6
Power Turbine Pressure Ratio		2.96
Power Turbine Adiabatic Efficiency	%	83
Overall Turbine Efficiency	%	86.5
Overall Turbine Specific Heat Ratio		1.31
Gas Generator Mechanical Efficiency	%	98
Output Gearbox Efficiency	%	98
Exhaust and Interstage Duct Pressure Loss	%	5
Output Power	kW (hp)	236 (317.1)
Fuel Consumption	kg/hr (lb/hr)	75.2 (165.9)
Specific Fuel Consumption	kg/kW-hr (lb/hp-hr)	0.318/(0.523)
Rotational Speed	rpm	71,222

compressor design due to the relatively small hub diameters. With the approval of NASA, it was elected to proceed with a rear end output drive from the power turbine. Engine design was further complicated when interspan or straddle-mounted bearing systems were considered; thus, an alternate,overhung gas generator,dynamic system was selected.

Figure 21 shows a cross-section of the proposed engine configuration with the complete gas generator rotor cantilever-mounted from a front-end bearing capsule. The first-stage compressor and monorotor are mated with a curvic coupling and held axially against the aft bearing race by the shaft torque nut. The two angular contact ball bearings are axially preloaded and retained in an oil-damped capsule in similar manner to the Solar two-stage compressor turbo-drive rig. Dynamic studies of this overhung configuration showed only one critical speed in the engine operation range, at 10 percent design speed. Operation at this speed would result in a maximum radial excursion at the monorotor exducer of 0.028 cm (0.011 in.). Although this amount of rotor overhang appears excessive by gas turbine practice, a similar system is used on a commercially available three-stage centrifugal plant air compressor.

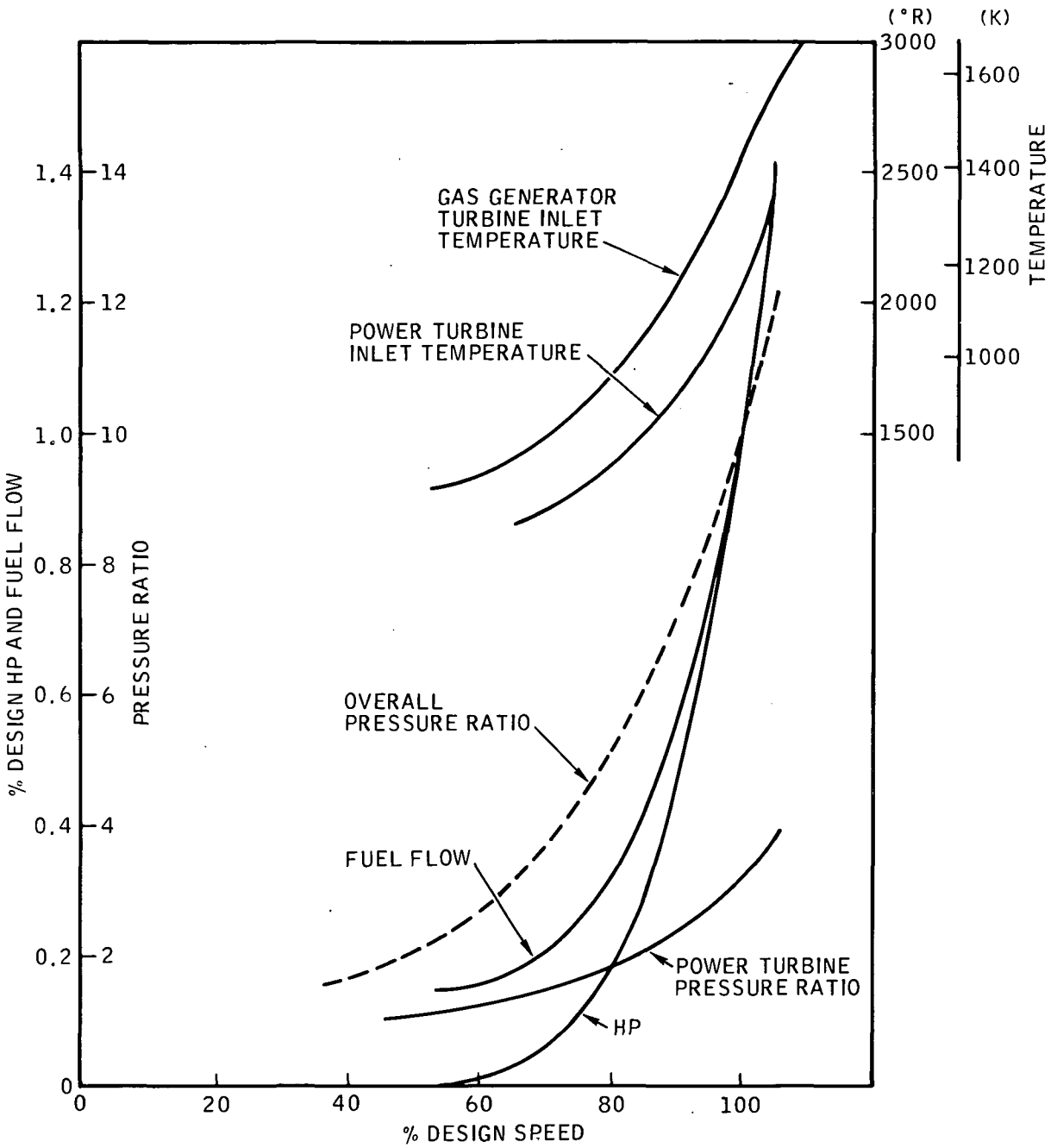

MR219A

Figure 19 - Estimated Monorotor Steady-State Performance

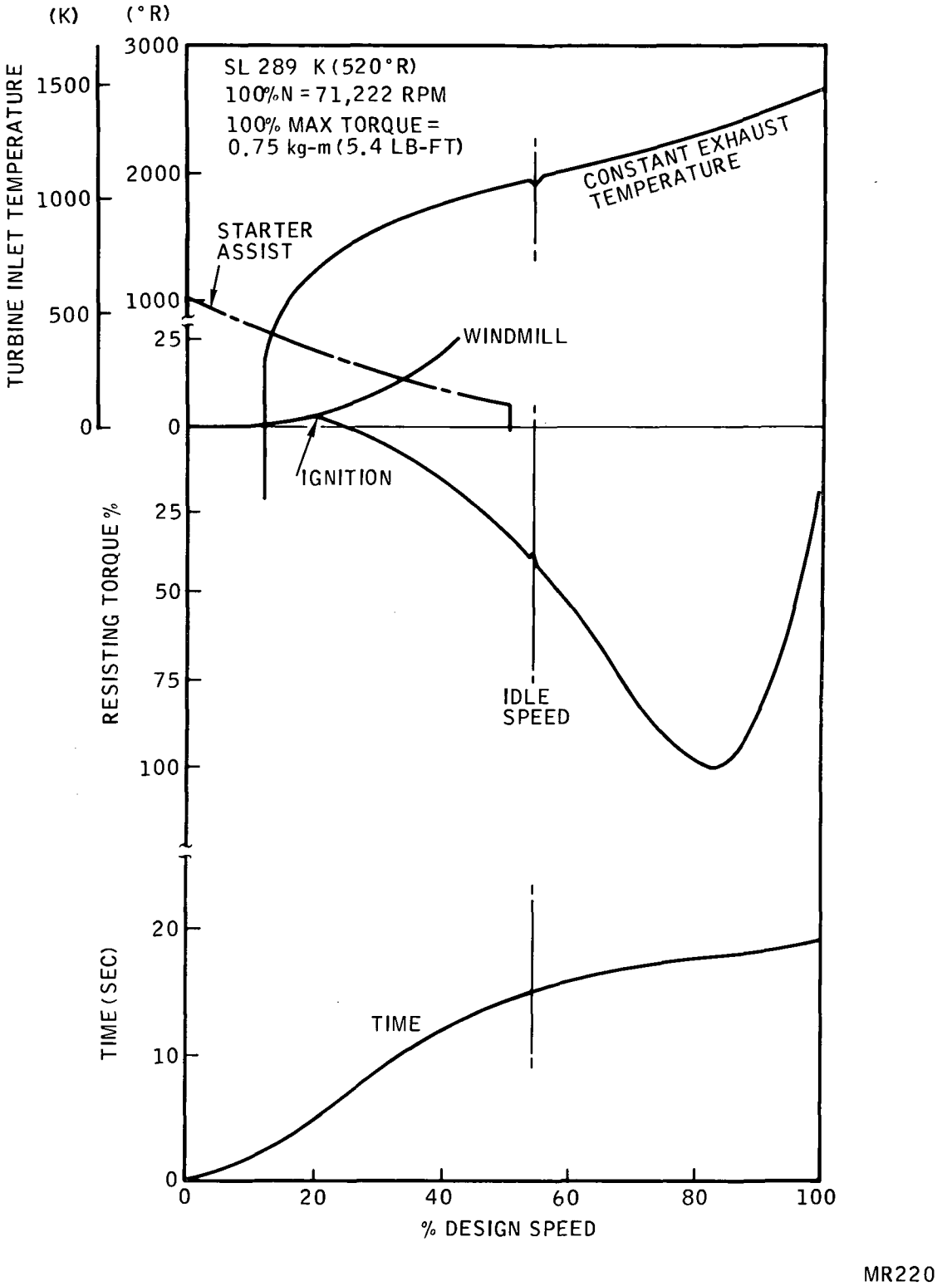

Figure 20 - Estimated Start Characteristics

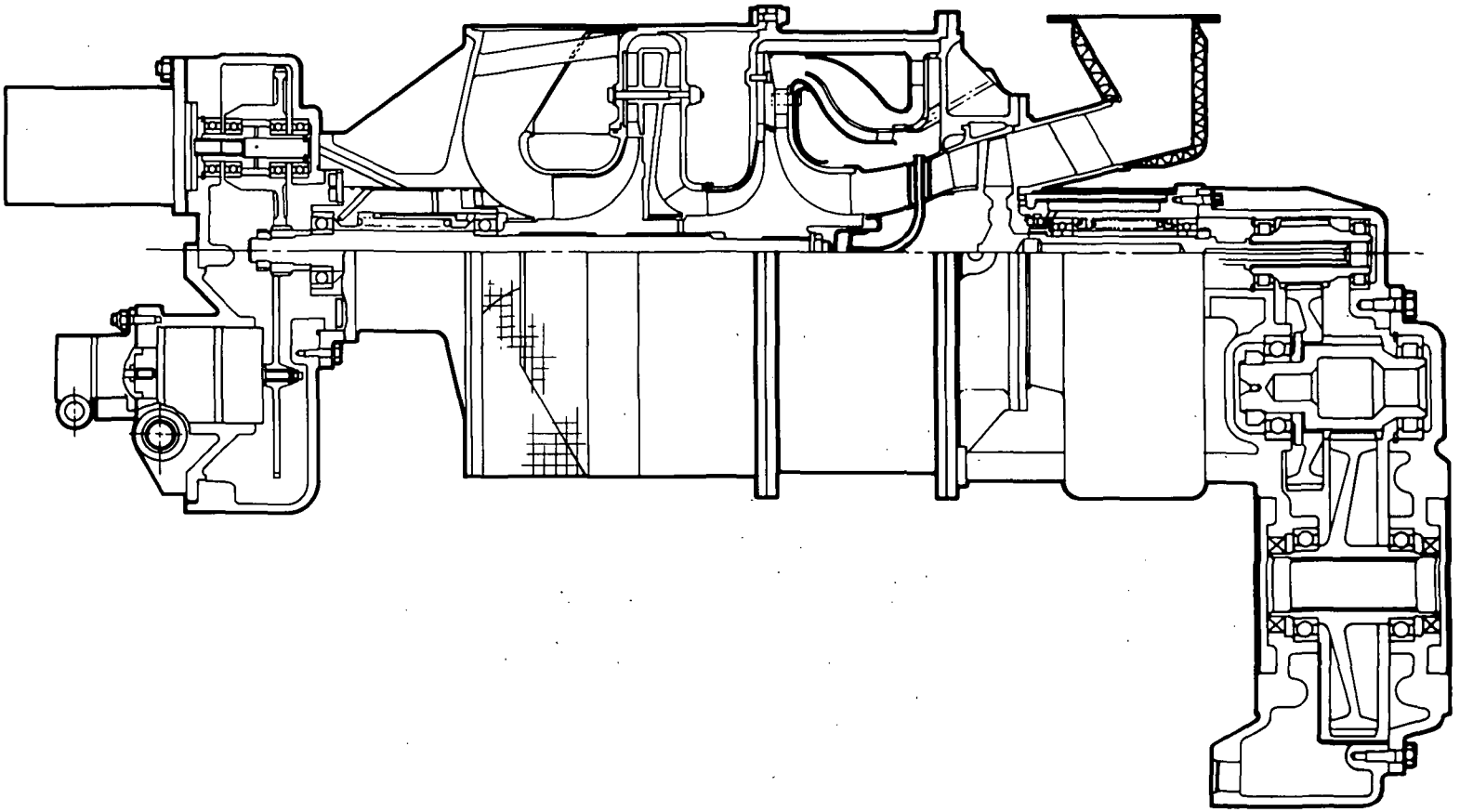

MR221A

Figure 21 - Engine Cross Section

The engine is assembled by an axial stack-up of the rotors and casings, commencing with the first-stage compressor inlet housing. The monostator is attached after the monorotor and is axially bolted to the second-stage compressor front shroud. It is envisioned that the monostator comprising the compressor diffuser, central plate, turbine nozzle vanes, and aft shroud would be a single-piece casting.

A reverse-flow axial combustor is depicted together with an uncooled single-stage axial power turbine. The axial power turbine is shown to discharge into a radial collector exhaust stack.

Supplementary cooling of the monostator is required since the shroud is convection cooled by means of radially outward airflow injected into the mainstream ahead of the nozzle vane leading edge in a thin film to protect the inner shroud. An impingement insert is accurately positioned in each nozzle vane core, metering cooling air to the leading and trailing edges of the vane. A small amount of cooling air is also fed from the combustor outer liner through the interstage turbine inlet to locally cool the shaft torque nut.

Component Test Rig Design

A cross-section of the component test rig is shown in Figure 22, which features separate compressor and turbine flow paths to facilitate mapping of both the compressor and turbine performance characteristics. Turbine air supply to drive the two-stage compressor would be 978 K (1760°R) at 1240E +03 Pa (180 lb/sq-in.). The first-stage compressor, monorotor, shaft, and bearing capsule form a complete balance assembly, and only the monorotor needs to be removed for final assembly into the rig. The planned spin test rig will require either manufacture of the first-stage compressor or the use of a simulated disc mass.

Rotating Assembly Dynamic Analysis

Dynamic analysis of the rotating assembly was completed with the rotors and shaft coupled to form a series of masses that respond as an integral assembly,which, in turn, is supported by flexible bearings and mounts.

A critical speed analysis was conducted which indicated that with two bearing spans and bearing stiffnesses in the range 0.09 to 0.18E +06 kg/cm (0.5 to 1.0E +06 lb-in.), only one critical speed occurred in the range 0 to 120 percent design speed. Dynamic test data from the Solar two-stage compressor rig indicated that the bearing stiffness for the two preloaded angular-contact M204 ball bearings was of the order 0.18E +06 kg/cm (1.0E +06 lb/in.). Using this bearing stiffness and a bearing span of 9.65 cm (3.8 in.), the first critical speed was calculated to occur at 7200 rpm (10 percent design speed).

An imbalance distribution was applied along the rotor span with light damping at the two bearing locations. Imbalance loads of 0.00025 kg-cm (0.003 oz-in.) were imposed at two planes of the two rotors.

Output from the computer dynamic response program consists of rotor radial excursion along with dynamic bearing loads as a function of speed. Figure 23 shows

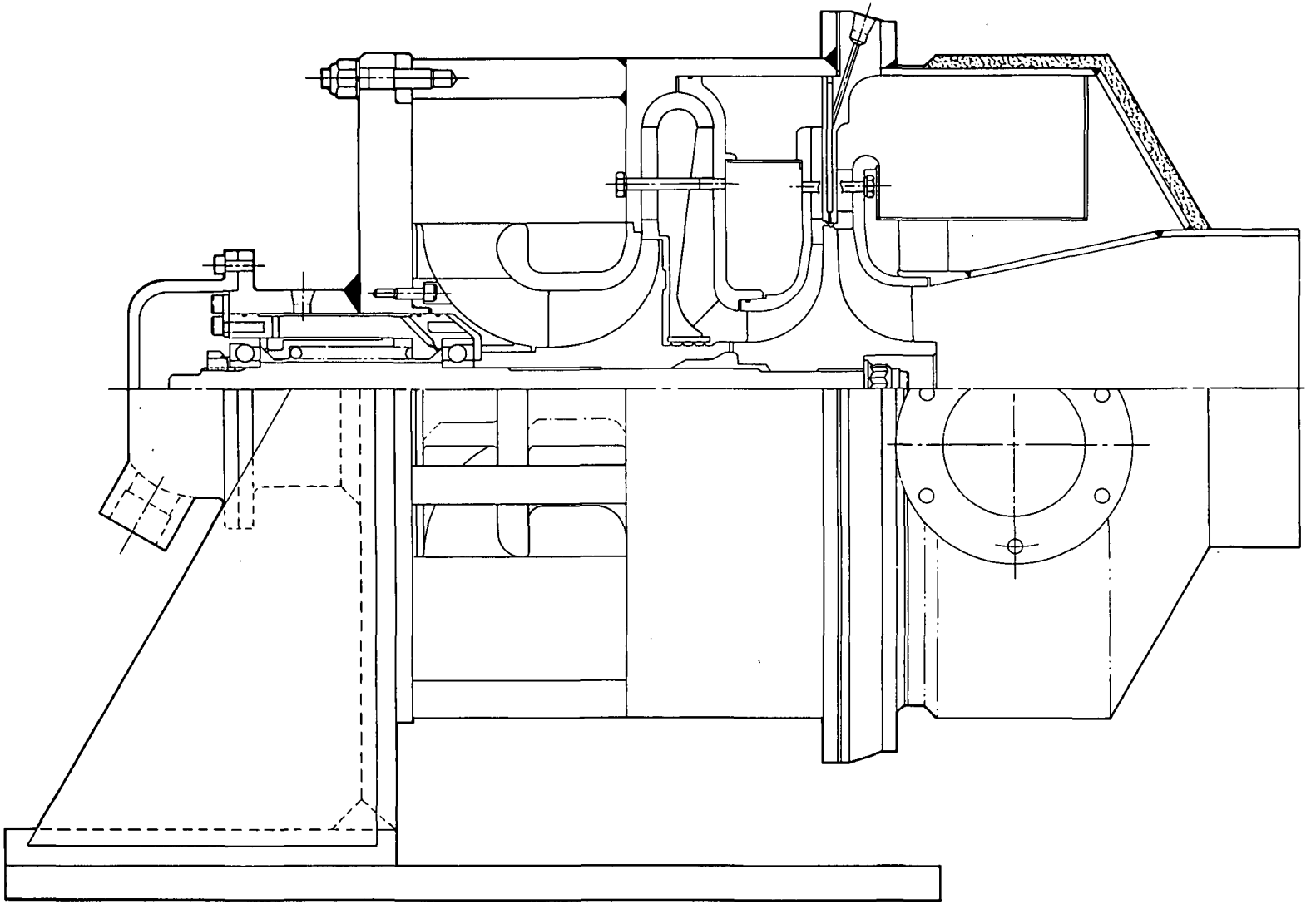

MR222A

Figure 22 - Test Rig Cross Section

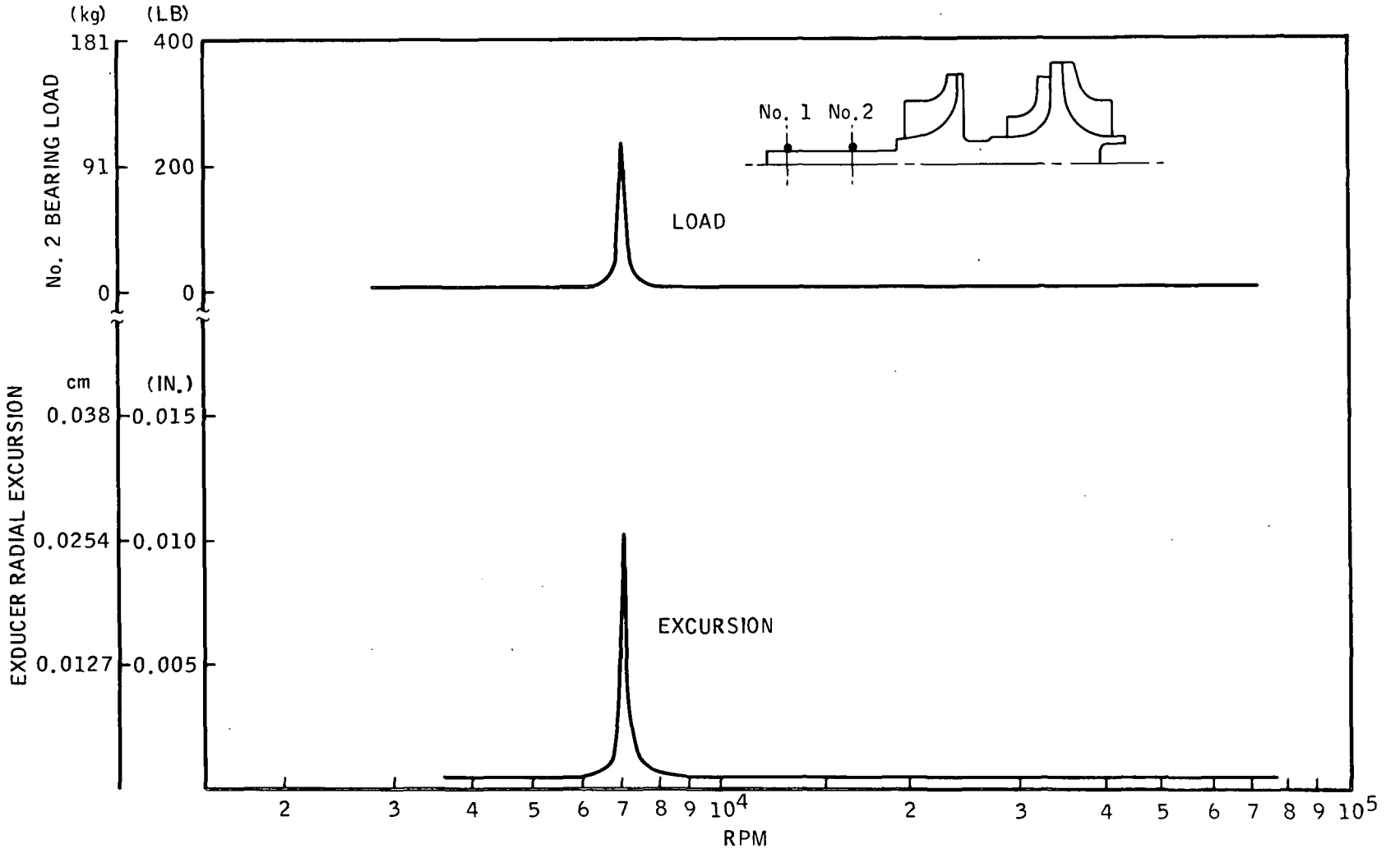

Figure 23 - Estimated Dynamic Response

the response for an in-phase imbalance condition. The critical speed appears at 7200 rpm; and at this speed, a computed steady-state running exducer radial excursion was 0.028 cm (0.011 in.). During actual transient start conditions with an acceleration rate of the order 3000 rpm/sec, radial excursion would be less than 0.028 cm (0.011 in.). Maximum steady-state imbalance bearing load was estimated to be 109 kg (240 lb). The rotating assembly end thrust to satisfy a bearing B_{10} life (M-50 material) of 1000 hours at 100 percent design speed was calculated to be 104 kg (230 lb) compared to a predicted aerodynamic end thrust of 250 pounds.

The estimated first flap static vibration modes of the monorotor compressor inducer and turbine exducer were estimated to be 12.5 and 13.5 kHz respectively. The interference plots of Figure 24 indicate that the diffuser and nozzle could cause excitation at approximately 70 percent speed; however, the basic blade stress levels and operating time at this speed would be relatively low.

Monorotor Thermal Analysis

During detail design, both the monorotor and monostator were analyzed for steady-state and transient temperature distributions. As a result of these preliminary study efforts, it was initially decided to concentrate monorotor thermal analysis efforts on a new, symmetrical rotor with 1422 K (2560°R) rotor inlet temperature without supplementary cooling.

The new monorotor design is shown in Figure 25. In this configuration, the rotor compressor and turbine surfaces have the same radius of curvature and are symmetrical about a plane through the rotor center. As the number of compressor and turbine blades are changed to 18 and 12 respectively, new aerothermodynamic data were generated for the revised flow paths. The turbine side inlet conditions are based on completely mixed nozzle flow and 7 percent rotor tip seal leakage flow, yielding a mixed gas temperature of 1422 K (2560°R) total absolute, i.e., relative to the stator structure. The mixing model is a pessimistic assumption for the turbine rotor, but could be optimistic for the turbine casing.

Compressor and turbine surfaces heat transfer coefficients were calculated on the basis of 0.91 kg/s (2.0 pps) total flow and relative local conditions. Thermal conductivity, viscosity, etc., were based on the thermal properties of air as a function of temperature. Blade heat transfer coefficients were calculated for length using flat-plate theory, rotor heat transfer coefficients from duct theory using local flow areas and hydraulic diameters. Blade surface areas (as well as metal node-to-node conductances) were calculated from actual blade dimensions, i.e., accounting for twist; rotor surface convection areas have the blade root areas subtracted.

The first series of thermal calculations indicated that the shaft end and nut would develop temperatures to 950 K (1710°R) due to added heat input from the rotor bore and exhaust afterbody, even with a 4340-type low alloy (high conductivity) carbon steel. Accordingly, it was deemed necessary to force-convection-cool these parts. The method currently contemplated is impingement on the shaft end with a guide-sleeve to route the air up into the shaft/rotor cavity before discharging to turbine exhaust. The air source would be throttled precombustor compressor air, strutted to the exhaust afterbody. As little flow as 0.25 percent allowed to heat to 700 K (1260°R) would be more than adequate for the purpose.

All local compressor air and turbine gas temperatures were input as the adiabatic wall temperature, calculated from the previously mentioned aero program output. While no thermal analysis was made of the first-stage compressor rotor, it was assumed the spline-coupling experiences 469 K (845°R) at the first rotor rear face, and that the shaft temperature is 379 K (682°R) at the first rotor center plane. Radiation interchange between the monorotor and casings was deliberately omitted owing to the predominant effect of the high convection coefficients and because the relevant temperature differences are not likely to be great. Radiation was accounted for, however, between the rotor and shaft; the exhaust afterbody was assumed to be cooled low enough (by heating the cooling air to 700 K (1260°R)) so as not to present a heat source to the monorotor assembly.

Monorotor temperature calculations were made possible through the use of the thermal analyzer computer program. The thermal models were based on 1/12 of a monorotor to correspond to a section having just one turbine blade (1-1/2 compressor blades). The monorotor, shaft, and nut were all considered to be made of INCO 718.

Thermal analyses were extended to include the possible film cooling effect of tip seal leakage flow along the monorotor turbine hub surface. The local adiabatic film cooling effectiveness at a distance (x) from the injection point was defined by

$$\eta_{f,x} = \frac{T_{g,x} - T_{aw,x}}{T_{g,x} - T_{oc,\,in}}$$

where

$T_{g,x}$ = local relative total gas temperature

$T_{aw,x}$ = local adiabatic wall film temperature at distance x

$T_{oc,in}$ = relative total coolant temperature at injection location (x = 0) = 589 K (1060°R).

The cooling effectiveness equation used was

$$\eta_{f,x} = \frac{1.59\ m^{0.34}}{\left(\frac{x}{ms}\right)^{0.68}}$$

where

m = blowing parameter $= \dfrac{(\rho W)\ c}{(\rho W)_g}$

s = injection slot height = 0.012 inch (0.031 cm)

c = coolant

g = gas

The blowing parameter, m, at the injection point was based on relative velocities (W) and was calculated to be m = 1.514 for a leakage flow rate of 0.064 kg/s (0.14 pps). Maximum film effectiveness of the injection location was $\eta_{f,x} = 0.44$.

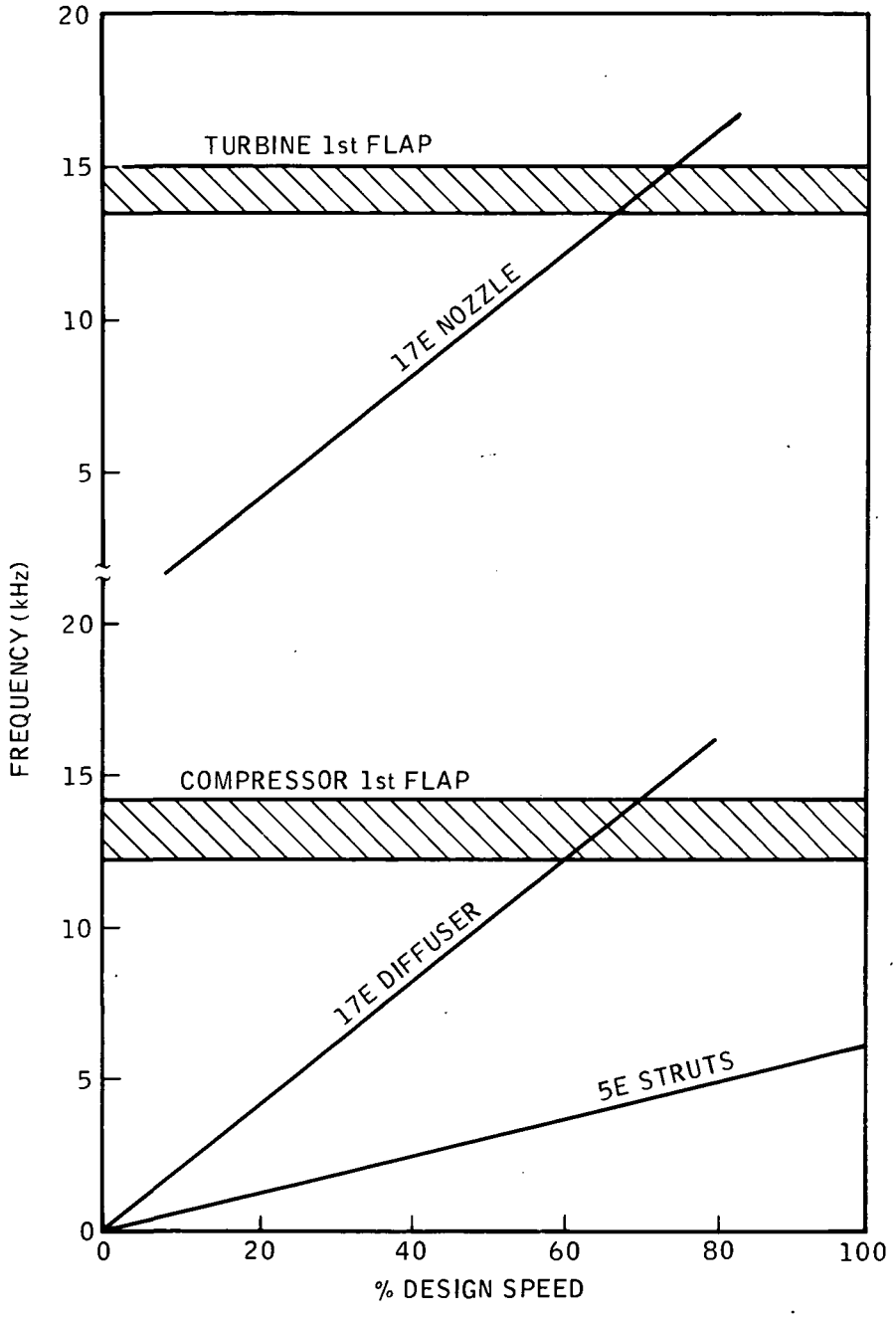

MR224A

Figure 24 - Blade Resonances

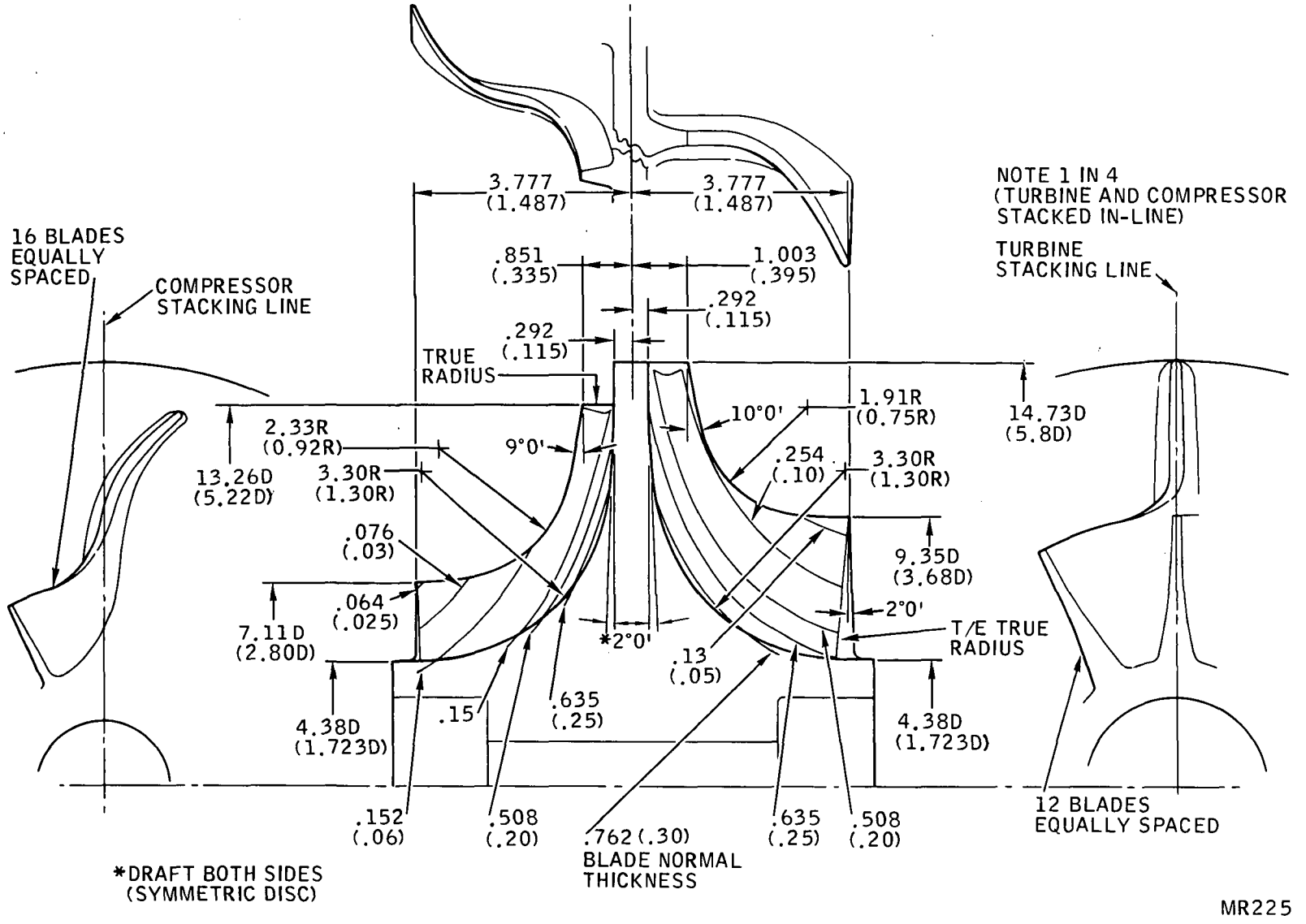

Figure 25 - Monorotor Detail Design

Monorotor temperature distribution at steady-state design point conditions is shown in Figure 26, both excluding and including the effects of tip leakage flow film cooling. As might be expected from previous analyses, the primary temperature gradients are in the axial direction with the center plane of the rotor being almost isothermal at 811 K (1460°R). The turbine blades are approximately 56 K (100°R) hotter at the exducer than at the inlet. The effect of tip leakage is to reduce turbine hub temperatures at the inlet and exit by 83 and 7.2 K (150° and 13°R) respectively. Aft-end impingement cooling of the shaft is quite effective, reducing local metal temperatures to 756 K (1360°R), sufficiently below a maximum allowable thread temperature of 922 K (1660°R).

Both start and shutdown transient temperature conditions for the monorotor were also analyzed. As the shutdown transient (maximum power to idle) reduces temperature greatly, the resulting temperature gradients are relaxed and become less of a problem than start transients. The starting schedule of speed vs. time has a significant effect on these transient thermal gradients, and since no particular schedule was delineated, it was pessimistically assumed to follow:

- Zero to idle speed (55 percent) in 15 seconds.
- Momentary 45-second checkout at idle speed.
- Idle to design power in 4 seconds.

Monorotor metal temperatures at selected nodes during this start transient are shown on Figure 27 and indicate that all axial and radial temperature gradients reach their maximum values 85 seconds after initiation of the start sequence. Transient stresses were therefore analyzed at this critical 85-second condition.

The convective heat transfer from the monorotor to the second-stage compressor air was calculated for the design conditions and found to be equivalent to an additional 6.1 K (11°R) rise in rotor exit temperature.

Monostator Thermal Analysis

Thermal studies were initially conducted for a monostator configuration with no supplementary air cooling, relying solely on direct heat conduction to the central disc. These studies revealed the following:

- Unacceptable aft shroud metal temperatures of up to 1412 K (2542°R) with mixed burner exit temperature of 1536 K (2765°R), and apparently 44 K (80°R) higher with hot spot burner exit temperature of 1670 K (3006°R).
- Nozzle vane trailing edge temperatures as high as 1589 K (2860°R) were calculated even though the vane height was relatively small with a cooler adjacent sidewall.

Both film cooling of the aft shroud and increasing nozzle vane trailing edge thicknesses up to 0.20 cm (0.08 in.) were tried, but peak centerspan vane metal temperatures with burner exit hot spots were still unacceptable at the 1400 K (2520°R) level, so it

TEMPERATURE CONVERSION																				
°F	500	600	700	800	900	1000	1100	1200	1300	1400	1500	1600	1700	1800	1900	2000	2100	2200	2400	2600
°R	960	1060	1160	1260	1360	1460	1560	1660	1760	1860	1960	2060	2160	2260	2360	2460	2560	2660	2860	3060
K	533	588	644	700	756	811	867	894	977	1033	1088	1144	1200	1255	1311	1367	1422	1477	1532	1588

NOTE: TEMPERATURE GRADIENTS SHOWN ARE °R. REFER TO TABLE FOR K AND °F.

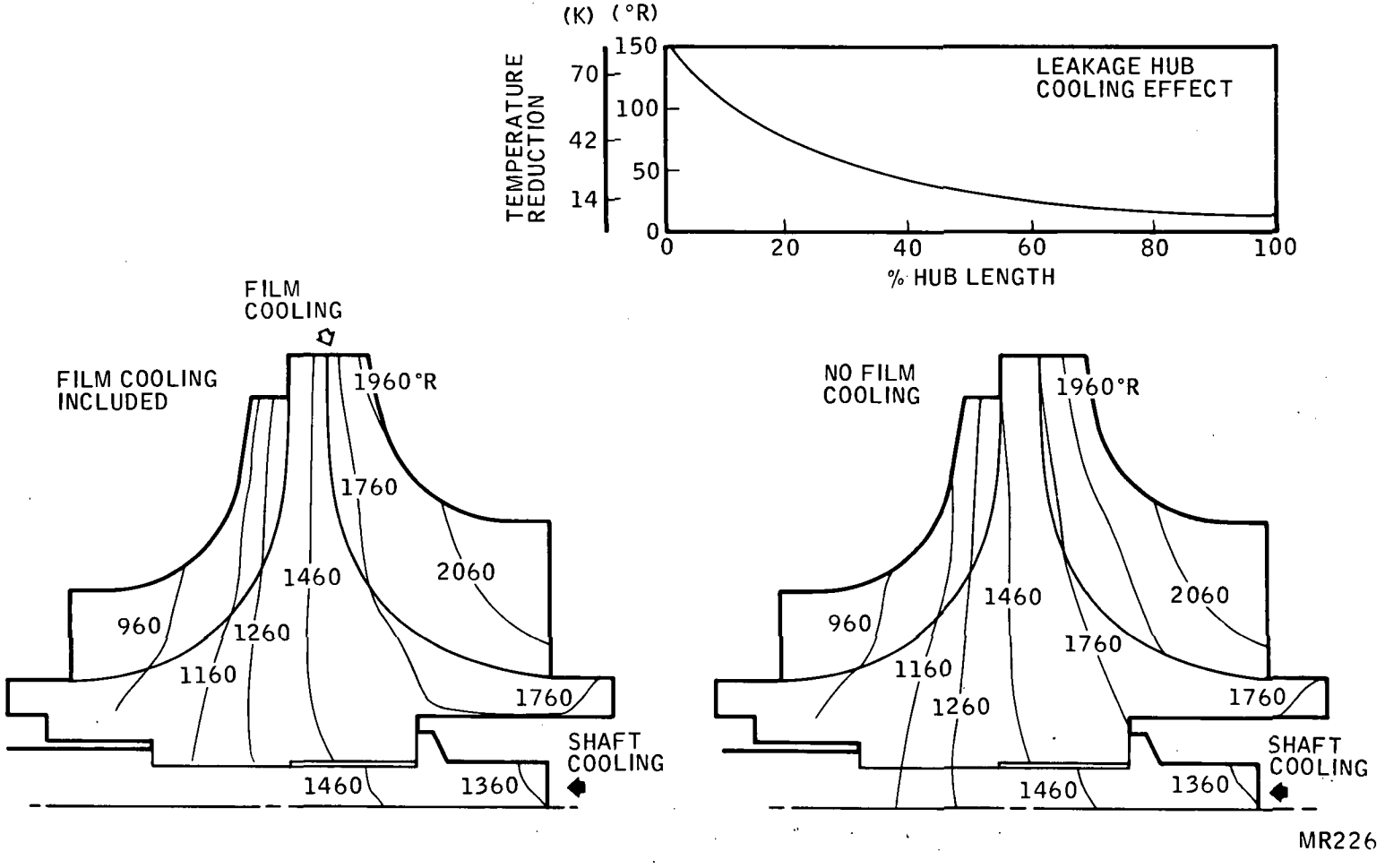

Figure 26 - Monorotor Temperature Distributions

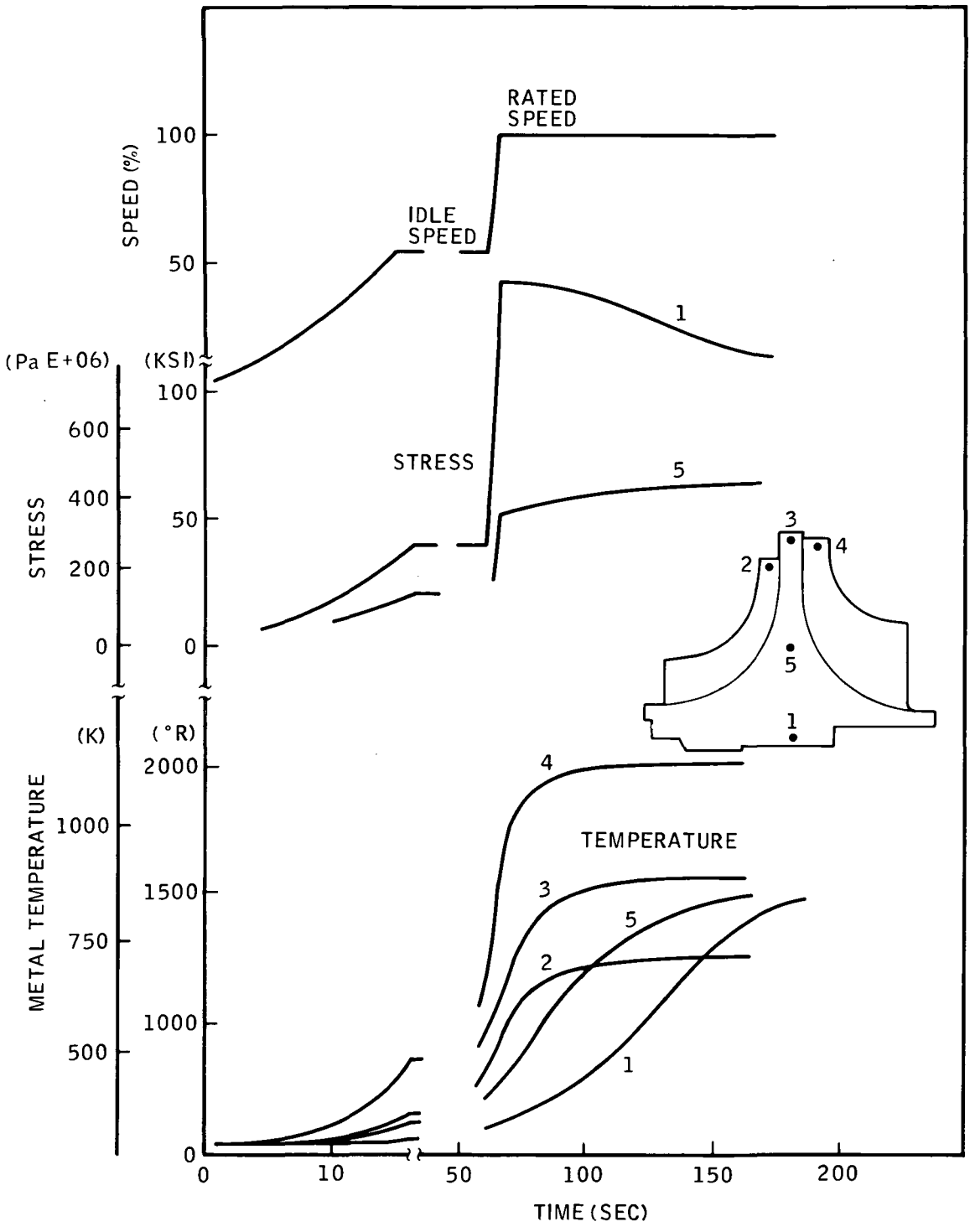

Figure 27 - Start Transient Temperatures

was necessary to abandon conduction cooling as the sole monostator cooling approach and to commence examination of a cooled monostator configuration.

Thermal network studies were carried out on the supplementary air-cooled monostator configuration shown in Figure 28. The shroud is convection-cooled by combustor dilution air flowing radially outward along the aft shroud boundary and subsequently injected into the mainstream ahead of the nozzle leading edge, thereby providing film-cooling protection along the inner shroud boundary.

Each nozzle vane comprises an internal insert in the vane core, metering cooling air through fore and aft holes; the vane front portion is thus impingement-cooled at the leading edge and convection-cooled on the pressure and suction surfaces. The vane rear section is convection-cooled with the coolant exiting the vane through the trailing edge orifices. The central disc does not require more cooling than provided by direct conduction to the "cold" compressor sink.

Table IX summarizes the principal data used in thermal analyses. The design goal was to limit the maximum monostator metal temperature to 1339 K (2410°R). Relatively modest minimum and average vane cooling effectiveness values of 0.326, i.e., $\frac{2546-1950}{2546-720}$, and 0.354, i.e., $\frac{2546-1900}{2546-720}$, were sought which could be obtained by the classical leading edge impingement, pressure and suction side convection, and trailing edge ejection cooling scheme. Nozzle vane heat load is governed by the parameters listed in Table X.

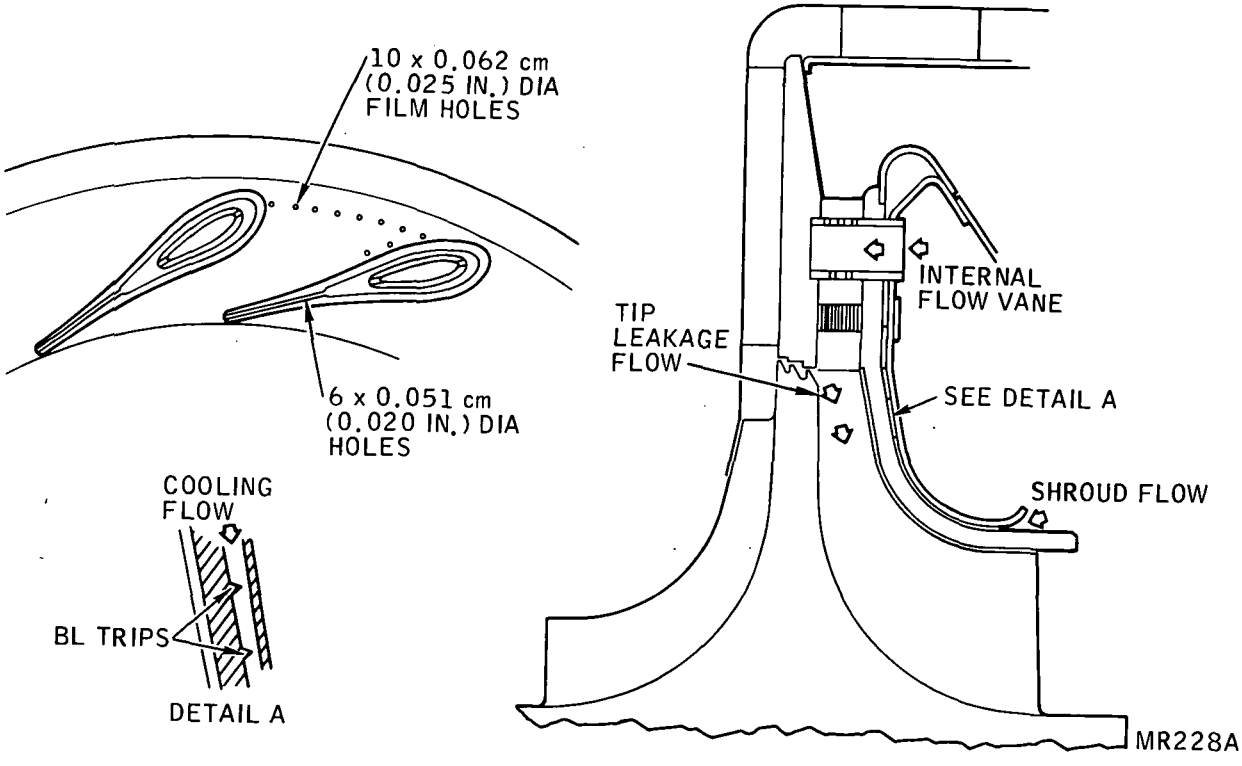

Figure 28 - Cooled Monostator Configuration

TABLE IX - COOLED MONOSTATOR, PRINCIPAL DESIGN DATA

Parameter	Units	Values
Compressor Discharge Total Temperature	K (°R)	633 (1140)
Average Diffuser Air Total Temperature		642 (1155)
Burner Exit Total Temperature		
Average	K (°R)	1517 (2730)
Hot Spot	K (°R)	1647 (2965)
Corresponding Pattern Factor: P.F. $= \frac{2965-2730}{2730-1180} = 0.151$		
Turbine Stator Inlet Gas Flow	kg/s (pps)	0.82 (1.81)
Turbine Stator Inlet Pressure		
Total	Pa (psia)	963E +03 (139.70)
Static	Pa (psia)	946E +03 (137.30)
Coolant-to-Gas Flow Ratios Used		
Nozzle vanes: $\phi_v = 0.039/1.81 = 0.0215$ (2.15 percent)		
Turbine shroud: $\phi_s = 0.057/1.81 = 0.0315$ (3.15 percent)		
Center plate: $\phi_p = 1.86/1.81 = 1.0276$ (102.76 percent)		

TABLE X - NOZZLE VANE HEAT TRANSFER PARAMETERS

Parameter	Units	Values
Number of Vanes		17
Span	cm (in.)	0.70 (0.275)
Ext. Exposed Perimeter/Vane	cm (in.)	8.75 (3.45)
Avg. Ext. Heat Transfer Coefficient	$\frac{\text{Btu}}{\text{hr ft}^2\ °\text{F}}$	429
Leading Edge Ext. Stagnation Heat Transfer Coefficient	$\frac{\text{Btu}}{\text{hr ft}^2\ °\text{F}}$	600
Leading Edge Diameter	cm (in.)	0.51 (0.20)
Trailing Edge Thickness	cm (in.)	0.152 (0.060)
Vane Chord	cm (in.)	4.11 (1.62)

The impingement cooling scheme to be used presents several advantages:

- Reduces chordwise metal temperature gradient to a maximum difference of about 82 K (148°R)

- Gives possibility of modifying the fore and aft insert jet angles to obtain nearly equal pressure and suction side temperatures via a method already tested at Solar

- Provides well-cooled trailing edge

- Keeps vane internal pressure higher than the external gas static pressure to prevent ingress of hot gases should a shell crack develop

- Minimizes external flow field perturbation and reduces trailing edge wake losses.

Turbine shroud cooling takes place predominantly by convection and impingement in a narrow gap (Figure 28) with eventual selective local impingement cooling and heat transfer promotion with circumferential boundary layer trip tabs. The spent air is then reinjected into the mainstream through angled film holes positioned to account for end wall cross-flow from the passage of higher pressure toward the lower pressure region. A conservative adiabatic film cooling effectiveness of 0.275 was used in the heat transfer model.

A 1/17 pie-shaped thermal network computer model of the cooled monostator was analyzed with both a uniform burner exit temperature of 1517 K (2730°R) and with a hot spot entry condition of 1647 K (2965°R) with coolant flowing along the shroud passage and vane insert at 656 K (1180°R). The computed operating environment of the monostator at the 1517 K (2730°R) temperature level is shown in Figure 29, indicating a maximum metal temperature in the shroud at the rotor tip of 1289 K (2320°R).

Estimated nozzle vane temperatures along the pitch section are shown in Figure 30 for average entry temperatures of 1517 and 1647 K (2730° and 2965°R). Actual metal temperatures would be between the two temperatures levels, probably peaking at 1344 K (2420°R).

Transient studies were also completed for the monostator with the 1/17 section thermal network during the critical start condition 85 seconds after start initiation. Figure 31 shows the thermal response of selected nodes at this interval, indicating a matched thermal response in the important tip seal region similar to that of the monorotor.

Monorotor Stress Analysis

Preliminary stress analyses showed large thermal stresses generated in the compressor blade in the vicinity of the bend from axial-to-radial directions due to the hotter adjacent disc applying shear loading to the blade. It was for this reason that efforts were made in detail design to reduce the temperature gradients and basic blade dynamic stresses by modifying blade geometry and allowing for tip leakage film cooling effects. Accordingly, blade thicknesses were increased to promote more conduction and reduced temperature gradients, besides adjusting taper ratios to reduce centrifugal stresses. The steady-state monorotor temperature distribution of Figure 26 (leakage cooling effect included) was subsequently applied to the 3D finite element models of the modified geometry.

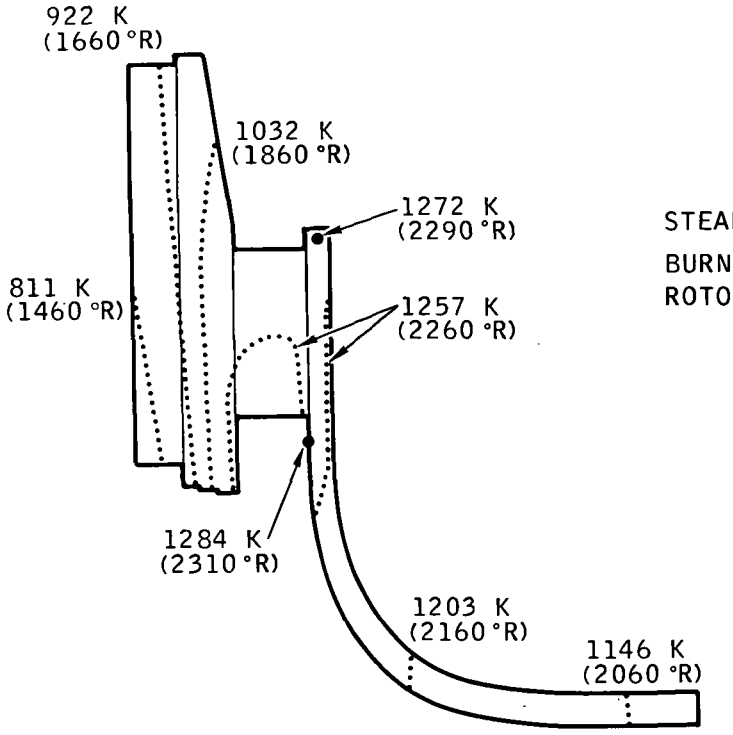

Figure 29 - Monostator Temperature Distribution

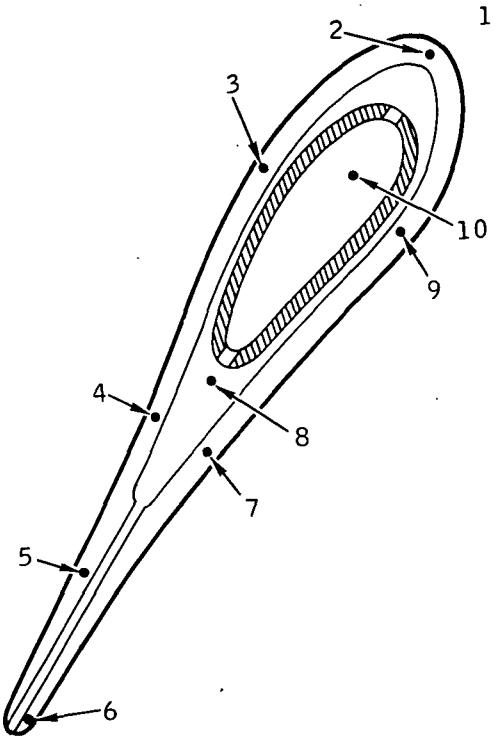

NODE	AVERAGE TEMPERATURE		HOTSPOT* TEMPERATURE	
	°R	K	°R	K
1	2730	1517	3006	1670
2	2215	1230	2370	1316
3	2237	1242	2392	1328
4	2306	1281	2469	1371
5	2310	1283	2475	1375
6	1851	1028	1949	1082
7	2363	1312	2532	1406
8	1493	829	1539	855
9	2311	1283	2474	1373
10	1180	655	—	—

*BASED ON WORST-CASE FLAT PROFILE

MR230A

Figure 30 - Nozzle Vane Pitch Section Temperature

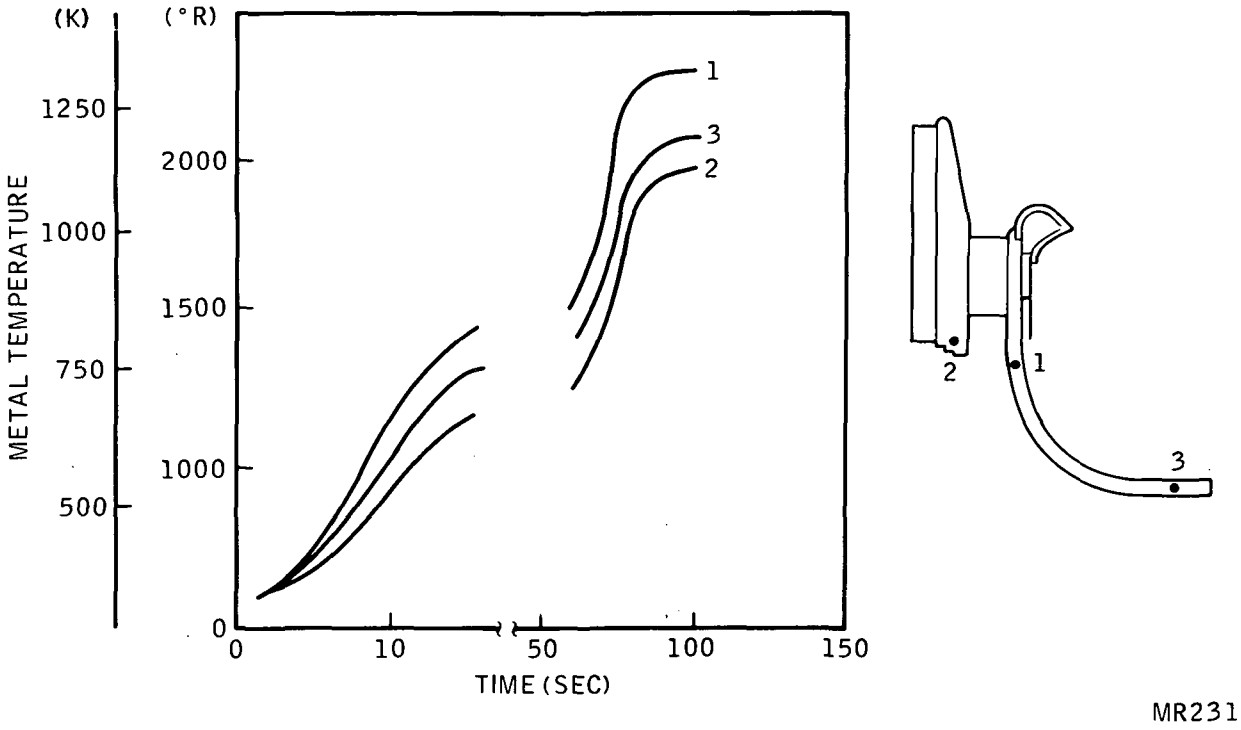

Figure 31 - Monostator Start Transient Temperatures

The finite element network for 3D models shown in Figure 32 employed an increased number of elements in the outer periphery, and the model covered a 90-degree sector of the monorotor with four compressor blades, three turbine blades, and the disc composed of some 1200 elements. Computed steady-state design condition 3D effective stresses in the compressor blade are shown in Figure 33 and reveal a significant reduction in blade stress to 964E +06 Pa (140 ksi) at a local metal temperature of 639 K (1150°R).

The lines of constant stress were computed for the Von-Mises combined stress criteria, σ_e, defined by the expression

$$\sigma_e = 1/\sqrt{2}\,[(\sigma_r - \sigma_t)^2 + (\sigma_t - \sigma_z)^2 + (\sigma_z - \sigma_r)^2 + 6\tau_{rz}^2]^{0.5}$$

where σ_r, σ_t, and σ_z are the radial, tangential, and axial normal stress components and τ_{rz} is the shear stress component.

Figures 33 and 35 show the interaction between the compressor blade and disc. It appears that the blade and disc are both loaded, since 3D disc stresses adjacent to the critical compressor stress regions exceed 689E +06 Pa (100 ksi) with a corresponding metal temperature of 800 K (1440°R). Effective 3D stress in the turbine blades is shown in Figure 35 with a critical stress of 482E +06 Pa (70 ksi) with an average metal temperature of 1000 K (1800°R).

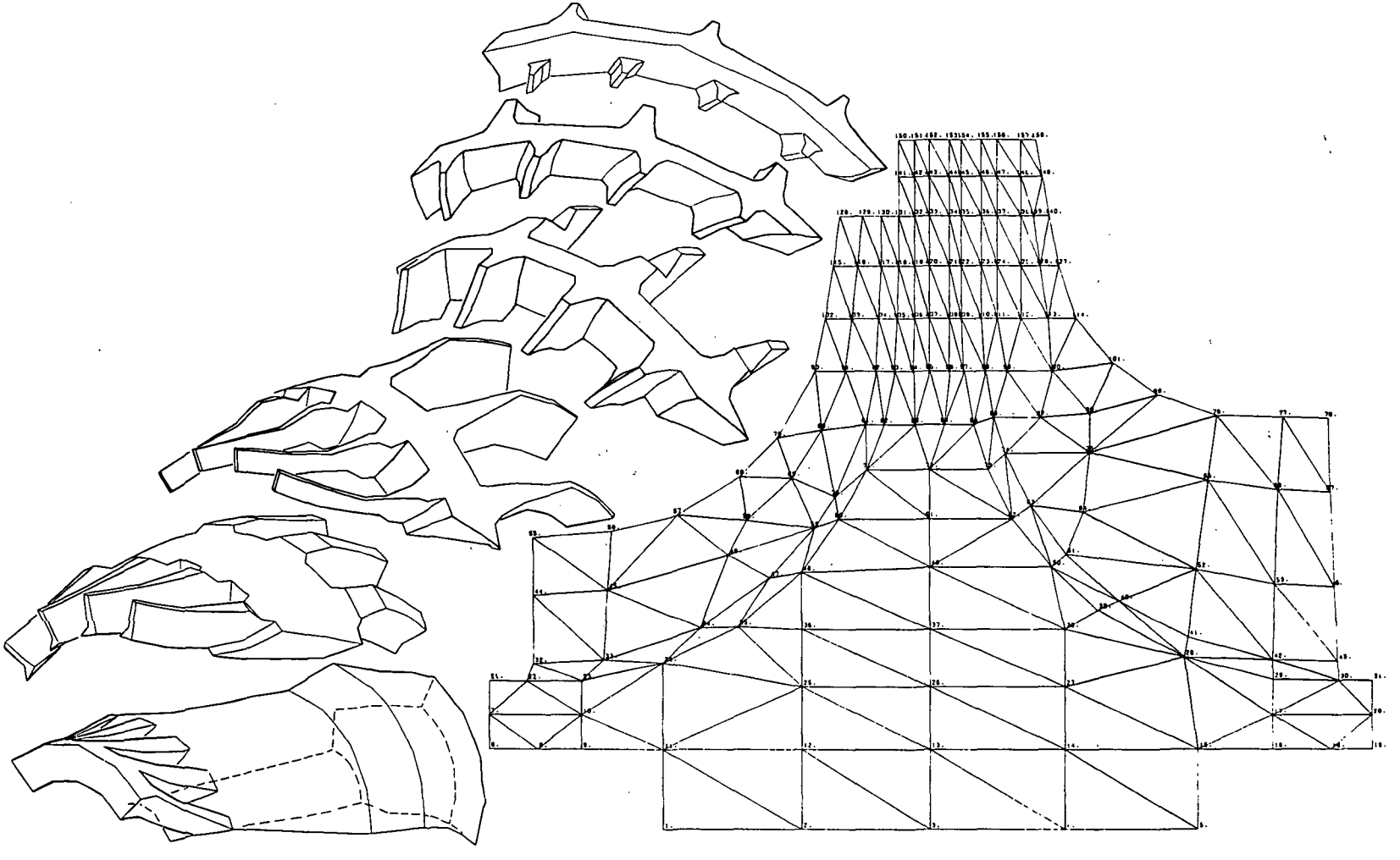

MR232

Figure 32 - Monorotor 3D Stress Model

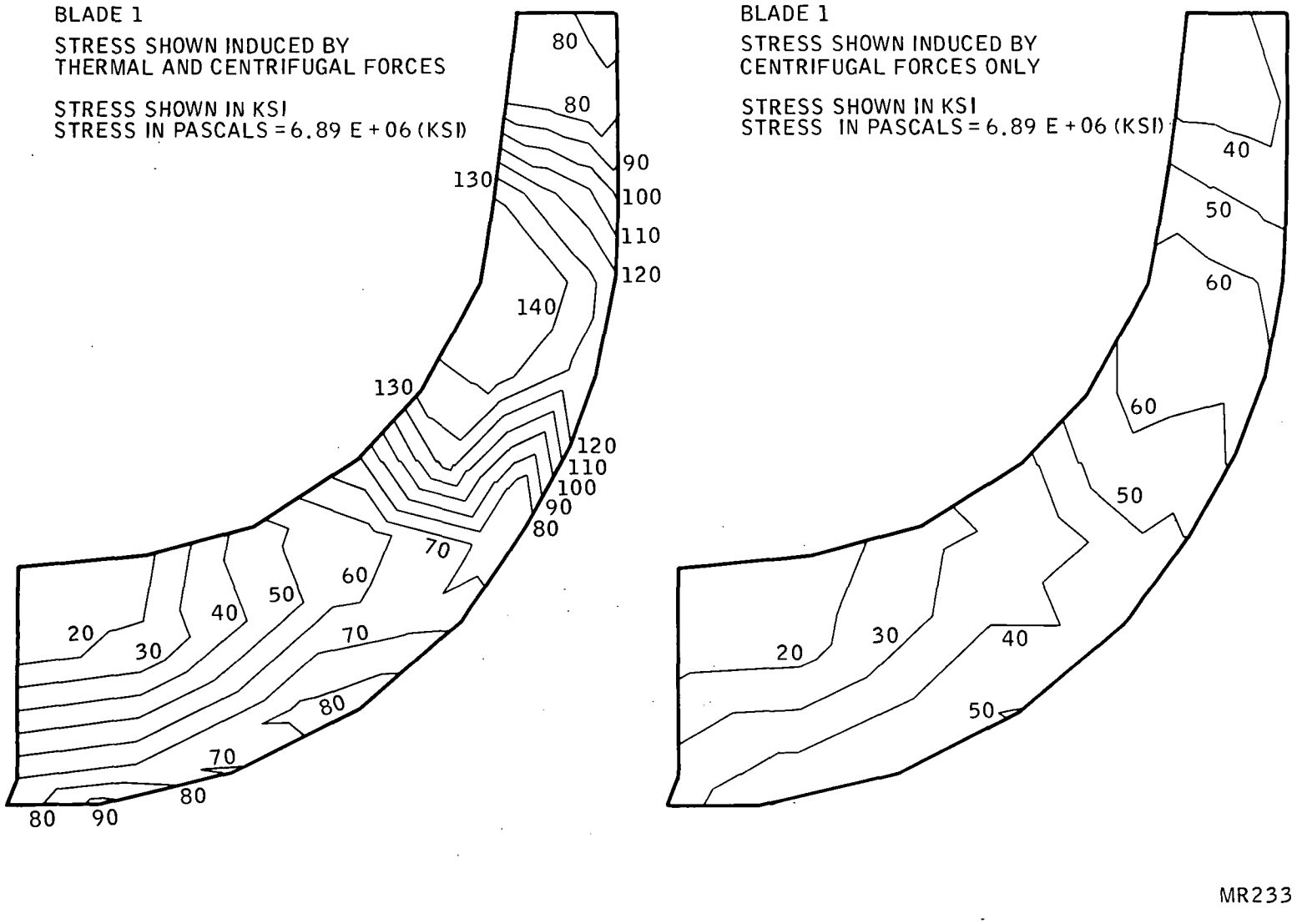

Figure 33 - Compressor Blade Constant Stress Lines

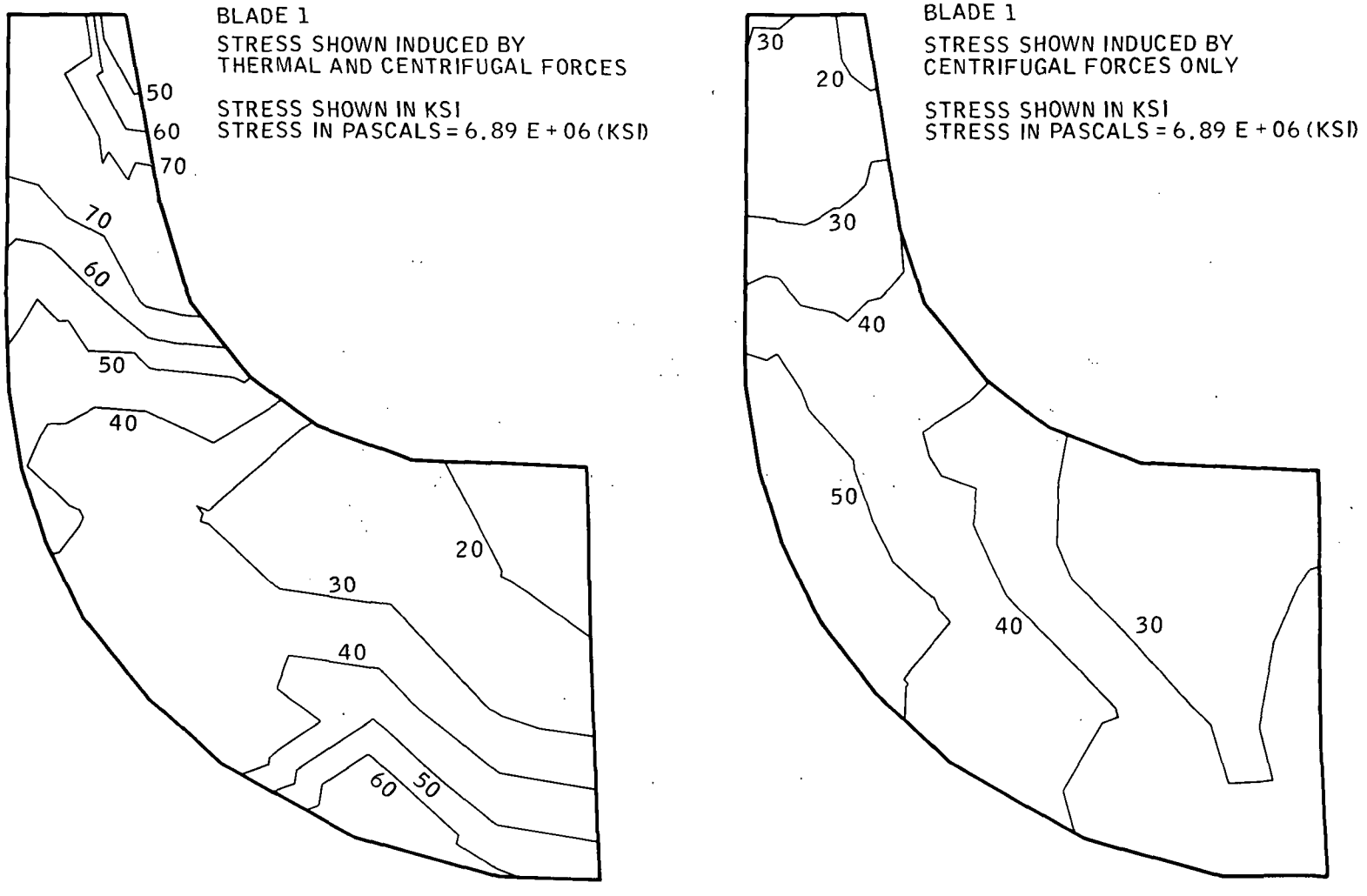

Figure 34 - Turbine Blade Constant Stress Lines

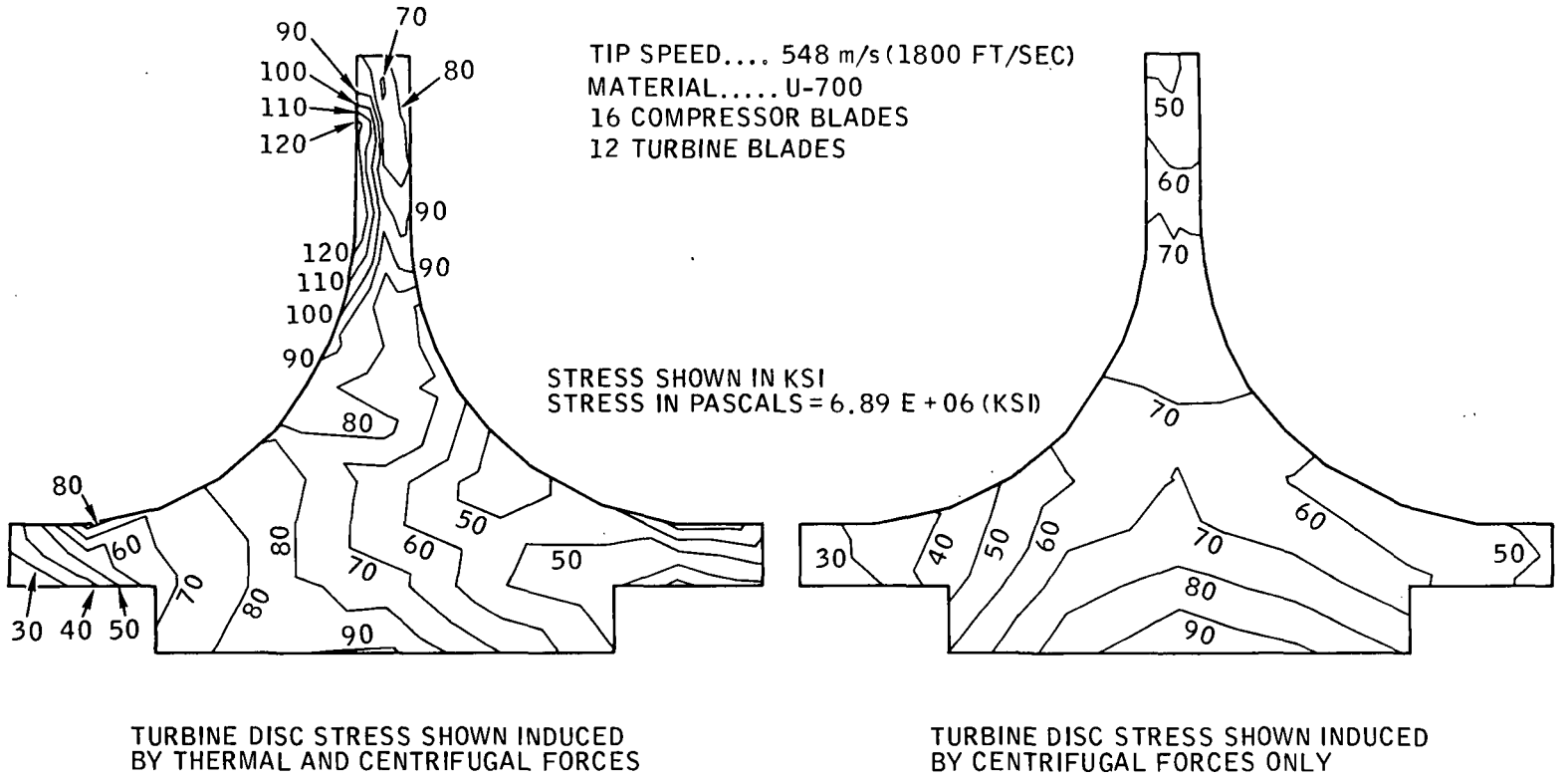

MR235

Figure 35 - Turbine Disc Constant Stress Lines

Approximately two-thirds of the high compressor blade stress in the vicinity of the shroud knee stems from differential thermal expansion between the blade and the disc; thus, optimization of internal temperature distribution is the key factor. The average equivalent stress in the disc was 440E +06 Pa (64 ksi) with a corresponding estimated burst speed of approximately 145 percent design speed. Computed distortion of the monorotor operating at the design conditions showed a maximum tip radial growth of 0.096 cm (0.038 in.). Compressor flowering was 0.41 cm (0.016 in.)

Monorotor transient stresses during the start sequence are shown on Figure 27 and indicate that hub stresses attain their maximum values at the 85-second interval, whereas the average tangential stress peaks at equilibrium conditions. It is interesting to note that the most difficult term to evaluate in thermal problems is the actual heat transfer coefficient. However, thermal stresses are dependent on temperature gradients, which are influenced to a lesser degree by the heat transfer coefficient. For example, a 50 percent change in heat transfer coefficient for the monorotor would result in approximately a 10 percent change in temperature gradient and stress.

Because of the severe thermal environment, resulting in a highly stressed monorotor, Udimet 700 was selected as a candidate material, having superior creep properties combined with competitive tensile and fatigue properties at elevated temperature.

Referring to Figures 26 and 34, and noting that up to 1033 K (1860°R) the 0.2 percent yield strength of Udimet 700 is essentially constant at 827E +06 Pa (120 ksi) minimum, a maximum disc effective stress of 689E +06 Pa (100 ksi) precludes short-time disc yielding at the maximum temperature design condition. Figure 27, however, shows a peak start transient stress of 964E +06 Pa (140 ksi) at 352 K (635°R) for a highly localized area in the disc bore region. If such does indeed occur — as is often the unavoidable situation in rotor design — the resulting local stress redistribution during the first rotational cycle will preclude subsequent rotor yield.

Monorotor blade stresses are all within the 0.2 percent minimum yield strength at the maximum temperature condition except for the localized area of 964E +06 Pa (140 ksi) compressor blade stress shown in Figure 33. The maximum blade temperature for this blade location is 639 K (1150°R) with a 0.2 percent minimum yield strength of 827E +06 Pa (120 ksi). As previously mentioned, this stress results primarily from blade shear loading imposed by the hotter adjacent disc and, therefore, can be reduced by improved disc temperature distribution.

The requirement of 30,000 idle-to-maximum cycles (which includes 15,000 start cycles) imposes a consideration of fatigue capability. For the discs, the bore is the critical area. The start cycle imposes a stress range cycle of 964E +06 Pa (140 ksi) at 325 K (585°R) and 792E +06 Pa (115 ksi) at 811 K (1460°R). The idle-to-maximum stress range cycle is 689E +06 Pa (100 ksi) at 811 K (1460°R) assuming no bore cooling in going from maximum to idle to maximum. Based on consideration of bore stress redistribution if yielding conditions occur, a design fatigue stress range of 827E +06 Pa (120 ksi) is a fair assumption. Published data (SAE Paper No. 670336) in fatigue life testing of Udimet 700 gives a nominal life of 20,000 cycles at 325 K (585°R) and 3000 cycles at 811 K (1460°R) for a stress range cycle of 827E +06 Pa (120 ksi). This life estimate becomes 7000 cycles at 811 K (1460°R) and stress range (the maximum-idle-maximum cycle). This estimate does not show conformance with the 30,000 cycle

requirement; however, the stress range cycle values used are pessimistic from the standpoint of localized bore stress redistribution.

Considering all factors that influence stress, calculation of an absolute value for stress-rupture life becomes complicated. A particular complication is the fact that creep, over a period of time, reduces the effects of thermal and bending stresses. This fact is very important when considering stress rupture life of the monorotor turbine blades since disc thermal interaction with the blade contributes most significantly to the calculated blade stress.

The monorotor disc stress-rupture life based on the temperature and stress values given in Figures 26, 33, 34 and 35 is in excess of 100,000 hours based on suppliers published data. The only area that appears marginal to meet a 1000-hour stress-rupture life requirement is the 428E +06 Pa (70 ksi) stress at a 1000 K (1800°R) blade temperature. The calculated stress-rupture life for this condition is approximately 700 hours. However, as stated above, this is an unduly pessimistic prediction.

Compressor blade temperatures are not high enough to include creep or stress rupture consideration.

Monostator Stress Analysis

A 2D finite element model of the cooled monostator was generated, and the thermal analyzer model results were applied to enable computation of the thermal stresses. Figure 36 shows the results of the 2D stress calculations and indicates a relatively high thermal stress in the monostator aft shroud of 241E +06 Pa (35 ksi) with a corresponding metal temperature of 1267 K (2280°R). Higher stress concentration levels were indicated at the intersections between the central diaphragm, nozzle, and diffuser vanes. Although the modeling was relatively coarse in these regions, stress concentrations are expected and could result in localized cracking with subsequent stress relief. The transient thermal gradients of the monostator shrouds during start are shown on Figure 31 and indicate the largest gradients occur under stabilized equilibrium conditions. The internal cooling arrangement of the vane minimizes the chordwise temperature gradients so that the maximum suction-to-pressure surface gradient during start is only 17 K (30°R) higher than the steady-state differential.

IN100 was selected for the monostator material, having adequate tensile strength and comparatively good stress rupture life and fatigue resistance.

At the maximum temperature of 1267 K (2280°R), IN100 0.2 percent yield strength is greater than 276E +06 Pa (40 ksi), so no short-time yield deformation is anticipated.

Creep deformation and stress rupture life under 1000 hours are predicted based on a constant stress value as given in Figure 36. At 1256 K (2260°R) a 2000-hour stress-rupture life limits the stress to 83E +06 Pa (12 ksi), and for a 2000-hour life at 1089 K (1960°R) the limiting stress is 276E +06 Pa (40 ksi). Therefore, creep deformation resistance and stress-rupture life appear marginal for this temperature distribution.

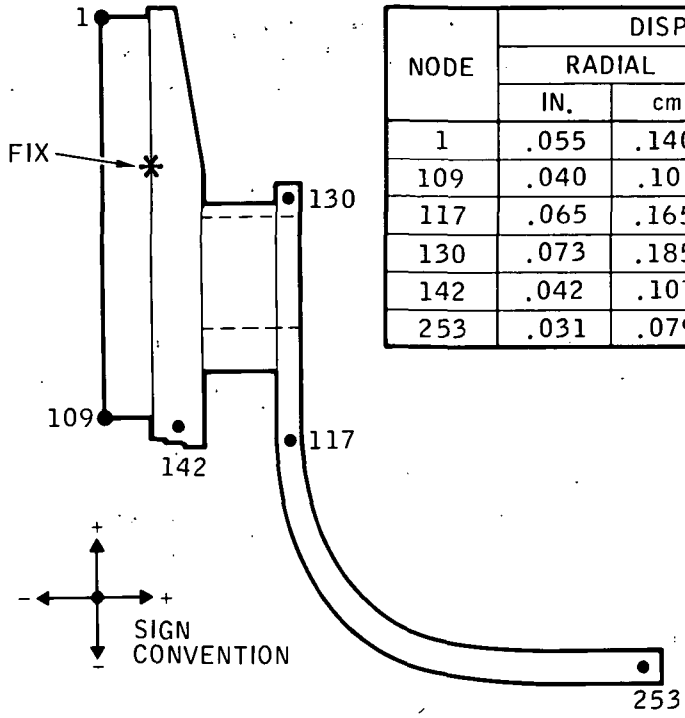

NODE	DISPLACEMENT				STRESS	
	RADIAL		AXIAL		KSI	Pa E+06
	IN.	cm	IN.	cm		
1	.055	.140	-.024	-.061	6.6	45.6
109	.040	.10	.027	.069	7.8	53.8
117	.065	.165	.023	.058	35.0	241.
130	.073	.185	.017	.043	16.4	113.
142	.042	.107	.031	.079	40.0	286.
253	.031	.079	.068	.172	13.0	89.8

BURNER TEMPERATURE
1536 K (2765°R)

MR236

Figure 36 - Monostator Operating Environment

Shaft Design

The rotating assembly is formed by the first-stage compressor and monorotor mounted on the central shaft and held together axially by the shaft torque nut and curvic coupling.

Since the rotor drive torques from the turbine are taken through the monorotor and curvic coupling to the first-stage compressor, the basic purpose of the shaft is to mount the rotors and prevent axial separation of the curvic. Axial separation may be caused by differential thermal expansion of the rotors and shaft, or dynamic imbalance; and it is necessary, therefore, to determine the torque nut preload that will maintain axial integrity throughout the operating range.

A critical axial separation condition could exist if the rotors were to reach thermal equilibrium conditions before the shaft makes any response. The additional shaft extension would be 0.066 cm (0.026 in.) with a corresponding increase in stress (above the initial locking stress) of 372E +06 Pa (54 ksi).

This stress condition would not actually be attained since the shaft would react thermally (to a small degree) during response of the rotors, and the majority of engine starts would be made with condition-monitoring at idle speed before accelerating to maximum power. Recommended torque value for the nut was 2.76 kg-m (20 ft-lb) with a corresponding initial preload of approximately 590 kg (1300 lb). The maximum shaft

axial growth at the steady-state design condition was estimated to be 0.118 cm (0.47 in.) relative to the "cold" forward bearing. Radial growth of the shaft and monorotor at the pilot bore position and steady-state design condition was estimated to be equivalent at 0.008 cm (0.003 in.).

Differential dynamic growth (assuming no thermal response) between the shaft and monorotor was 0.003 cm (0.0011 in.).

Tip Seal Design

A non-rubbing seal is required at the monorotor tip to control the air leakage from the compressor to the turbine. Large amounts of leakage result in mismatching the compressor and turbine components, in addition to producing potentially unsafe burner temperatures for a specific operating exhaust gas temperature. A metered, small quantity of leakage from a non-contact type labyrinth seal can, however, be used to slight advantage in providing a film cooling effect at the hot turbine tip and improving the efficiency of the compressor by reducing recirculation effects at the impeller tip. Tip leakage metering is determined by:

- Static-pressure differential across the blade tips
- Labyrinth seal design
- Differential thermal expansion of the monorotor and monostator

Rotor tip static pressures are influenced by blading reaction, which also affects aerodynamic axial end thrust. The type of tip seal design selected is shown on Figure 37, which indicates the anticipated thermal growths when operating at the design turbine inlet temperature of 1422 K (2560°R) at rated speed. A cold axial misalignment of 0.038 cm (0.015 in.) is required to attain line-to-line hot positioning of the monostator and monorotor. The third labyrinth tip shape directs the leakage air in a film down the turbine hubline.

Estimated leakage characteristics of a three-lip seal are shown in Figure 38 for the anticipated range of seal operating pressures with a hot radial clearance of 0.031 cm (0.012 in.). With compressor and turbine static pressures of 772 and 572E +06 Pa (112 and 83 psia), estimated internal leakage rate is 7 percent of the compressor airflow.

Detail Design Phase Conclusions

Detail analyses of the monorotor cooling principle reveal that:

- Low metal temperatures can be attained with the monorotor by direct conduction cooling, but the resulting relatively high temperature gradients cause large thermal stresses, particularly in the compressor blading near the shroud knee.
- In the high stress zones, approximately two-thirds of the stress level stems from thermal loading, thus calculation accuracy of the temperature distribution is a key design factor.

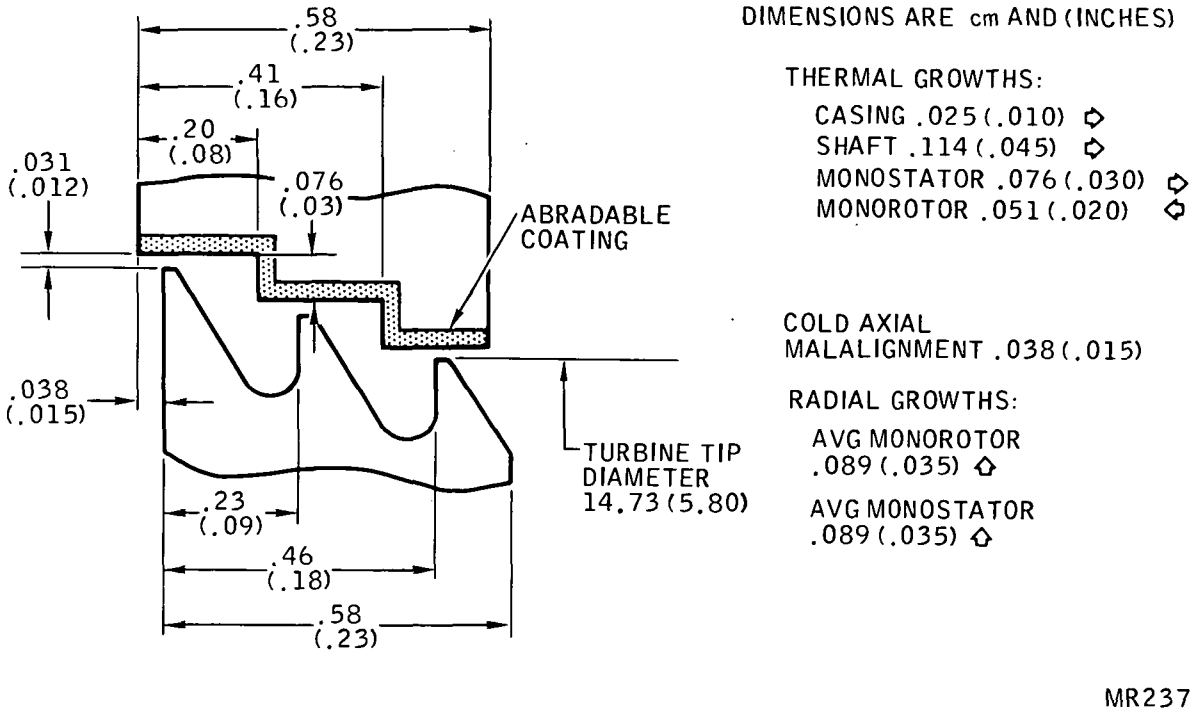

Figure 37 - Tip Seal Design

- Current monorotor geometry is considered the best compromise between aerodynamic performance and turbine life. Computed internal temperature gradients (and thus stresses) are considered conservative.
- Burner exit and monorotor gas inlet temperatures of 1517 and 1422 K (2730° and 2560°R) restrict turbine stress rupture life to less than 1000 hours.
- Estimated design life at maximum rated power was conservatively calculated at 700 hours compared with the design requirement of 1000 hours.
- Low-cycle fatigue life considerations limit transient power excursions from idle to maximum power to 7,000 compared with the design requirement of 30,000 cycles. The stress range cycle values used for these transients were, however, pessimistic from the standpoint of localized bore stress redistribution.

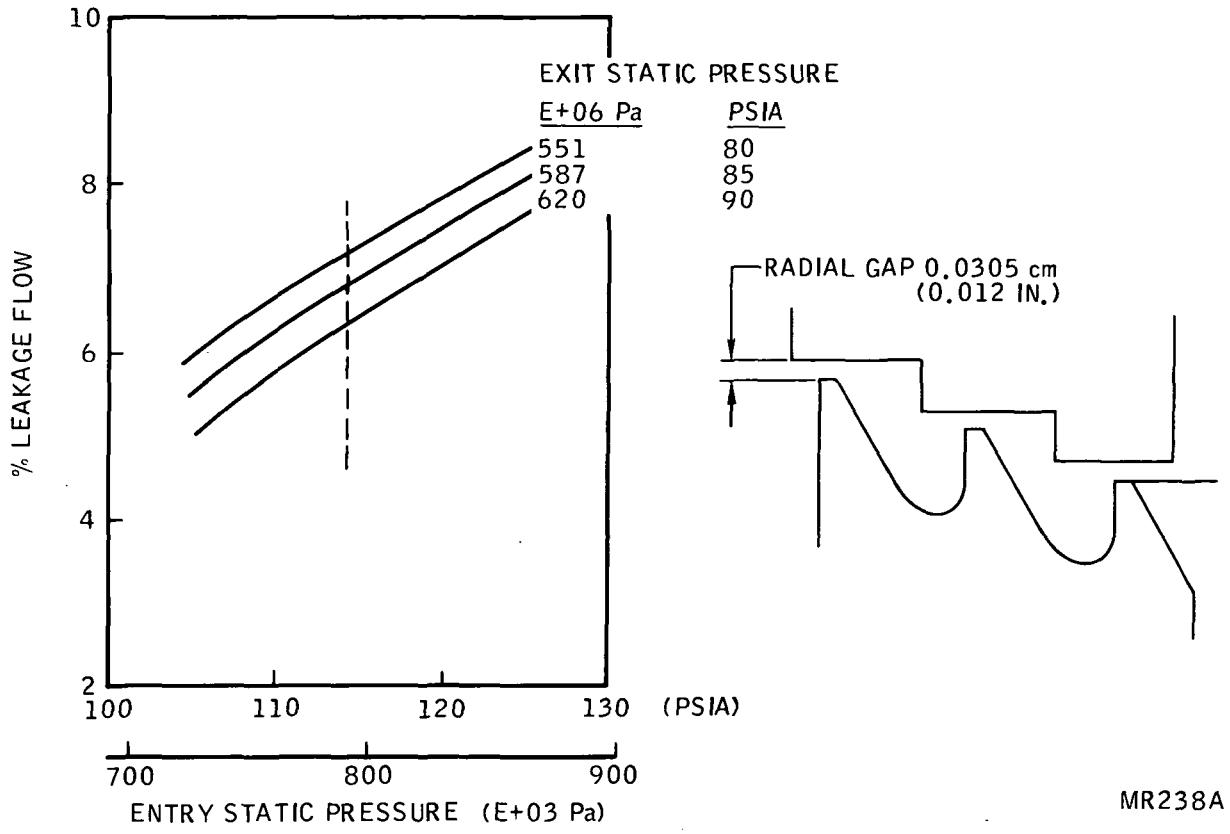

Figure 38 - Tip Seal Leakage

FABRICATION OF PARTS AND ROTOR ASSEMBLY

The finalized monorotor design, first-stage compressor impeller, shaft and bearing capsule, shown in Figure 39, was approved for fabrication and spin pit proof testing. In addition, the program was modified to include fabrication and dynamic verification with a dummy rotor mass system prior to proof spin tests of the actual rotating group.

The dummy rotor masses were designed to simulate the actual rotor weights and centers of gravity and were also coupled with the design curvic configuration.

Two monorotors were integrally machined from Udimet 700 (Astroloy) forgings. Tensile bar test specimens machined from the forgings were submitted to mechanical testing and revealed a room temperature U.T.S. of 991E ±06 Pa (144 KSI), satisfying design strength requirements. Figure 40 shows a machined monorotor prior to assembly.

The first-stage compressor impeller was integrally machined from a titanium 6A1 4V forging using existing tooling, with the pantograph arm adjusted to provide the required geometric scale ratio.

All rotors and the shaft were individually balanced on arbors before final balancing of the dummy and actual rotating groups mounted on the final rotor bearings. Pilot bore diameters, blade-tip diameters, and runout of the monorotor exducer hub diameter extremity were recorded.

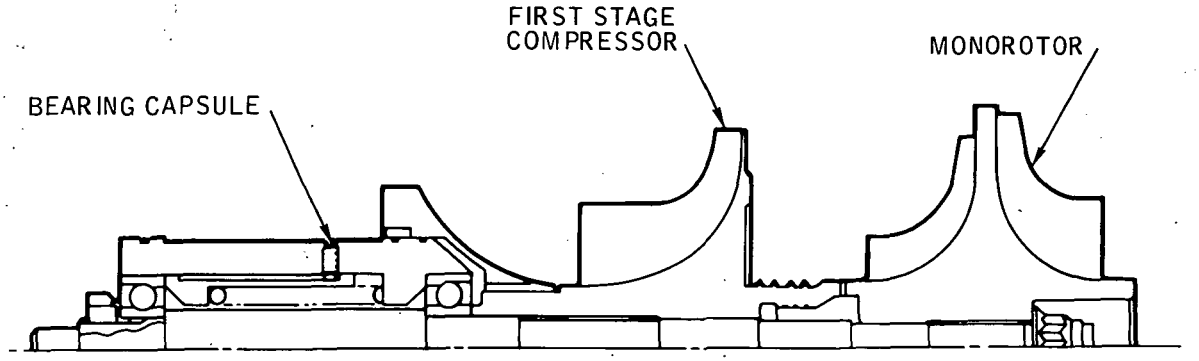

Figure 39 - Monorotor Rotating Assembly

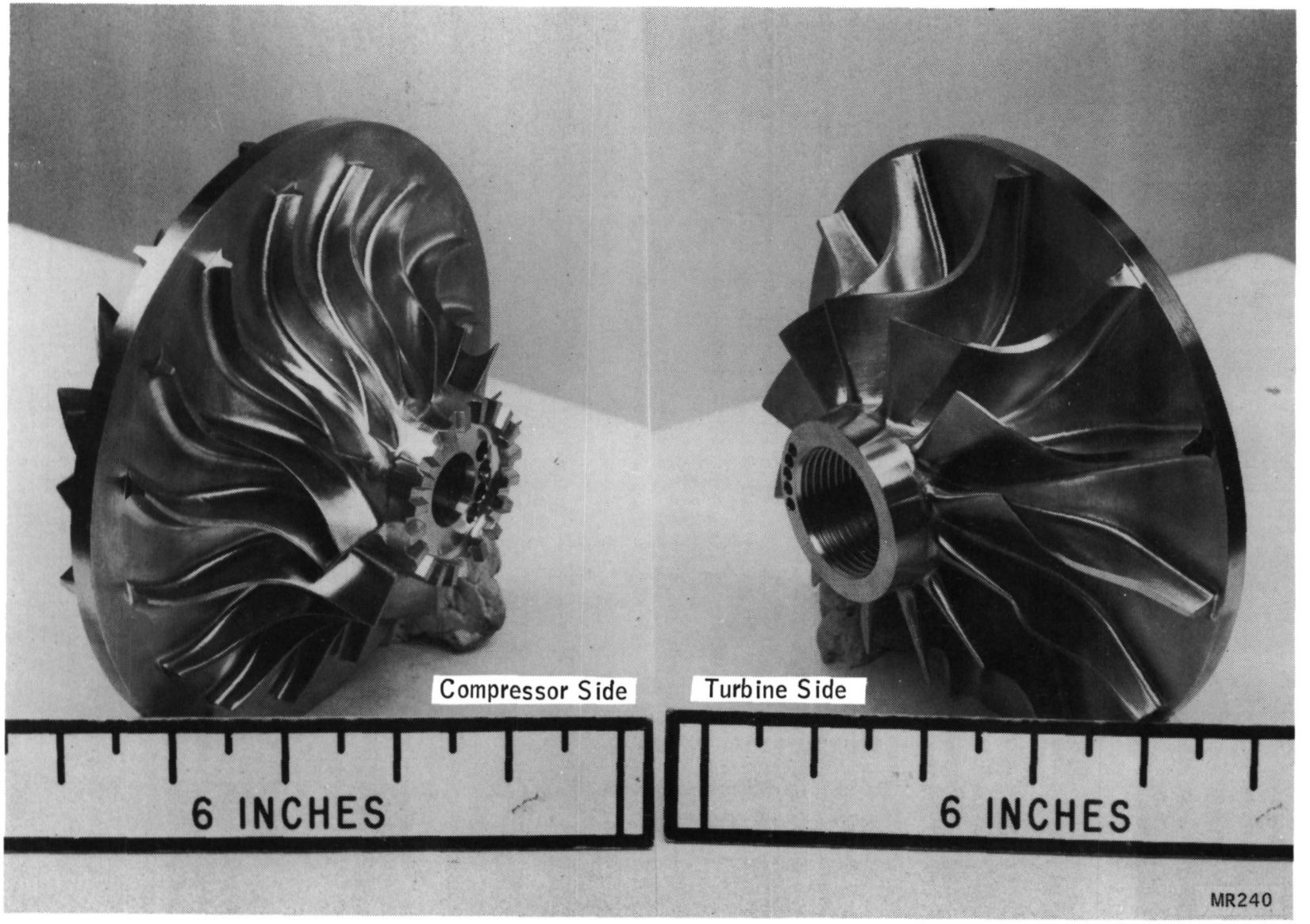

Figure 40 - Integrally Machined Monorotor

MECHANICAL TESTING

Mechanical testing of the monorotor was conducted in three phases. First, the natural resonant vibration frequencies of the monorotor test article were determined through a series of vibration tests. Next, spin rig operation was verified and the instrumentation was calibrated using the dummy rotor assembly. Finally, the actual monorotor test article was spun to obtain bearing temperatures and dynamic strain measurements.

Blade Vibration Tests

Vibration tests were conducted on the first stage compressor and monorotor blades to determine their natural blade flap resonant frequency. The turbine rotor assembly was held stationary while the component rotor blades were excited to induce their resonant frequency. Each blade of both compressor and monorotor components was analyzed by scanning the blade frequency output signal with a Spectral Dynamics analyzer to identify the first flap resonance.

Instrumentation for the component blade vibration test consisted of a microphone to pick up the output signal from an excited blade and a Spectral Dynamics real-time analyzer to store the output signal in memory.

Fundametal resonant blade frequencies were easily identifiable, and a summary of test results is shown in Table XI.

TABLE XI - NASA ROTOR COMPONENT BLADE RESONANT FREQUENCIES

Blade Number	Resonant Frequencies (Hz) 1st Stage Compressor (Long Blades)	2nd Stage Compressor (Long Blades)	1st Stage Turbine
1	2330	10,780	11,720
2	--	--	12,040
3	2280	10,660	12,180
4	--	--	11,940
5	2210	10,740	11,920
6	--	--	12,062
7	2350	10,520	11,840
8	--	--	11,660
9	2370	11,180	11,660
10	--	--	11,680
11	2350	11,400	11,780
12	--	--	11,720
13	2290	10,920	--
14	--	--	--
15	2220	11,260	--
16	--	--	--

Dummy Rotor Spin Tests

The balanced dummy rotor system was installed in the spin pit and the instruments connected as shown in Figure 41. An external lubricating system provided jet lubrication to the rotor ball bearings and the oil pressure was regulated at 172 ±03 Pa (25 psia). This pressure level proved satisfactory with minimum flow to the bearings to prevent flooding of the lower ball bearing.

Lower ball bearing outer race temperature, temperature in the spin pit, and rotor speed were recorded on an oscillograph strip chart recorder. Two proximity probes were installed 90 degrees apart at the simulated monorotor turbine exducer. Probe output signals and rotor speed were fed to the Spectral Dynamics analyzer. The proximity probe output signals were also displayed on an oscilloscope for real-time monitoring of the rotor dynamics. Probe calibrations indicated the simulated exducer static runout to be 0.0025 cm (0.001 in.).

The dummy rotor system was run in the spin pit chamber while maintaining a vacuum near 101E ±03 Pa (30 in. Hg).

The initial run brought the rotor through its first critical speed to 50 percent design speed. As shown in Figure 42, critical speeds were observed at 10 and 14 percent design speed with a well-controlled total deflection of the rotor at the turbine simulated exducer of 0.0038 cm (0.0015 in.). The presence of two criticals indicated different criticals in each of the proximity planes due to varying system stiffness. The multiple traces shown on the figures represent both acceleration and coast-down with the analyzer recording (a) all frequencies and (b) rotor rotational frequency.

The second run brought the rotor to 100 percent speed (71,222 rpm) with a repeat of the critical speed excursion characteristics and a maximum runout of 0.0015 cm (0.0006 in.) at 100 percent speed.

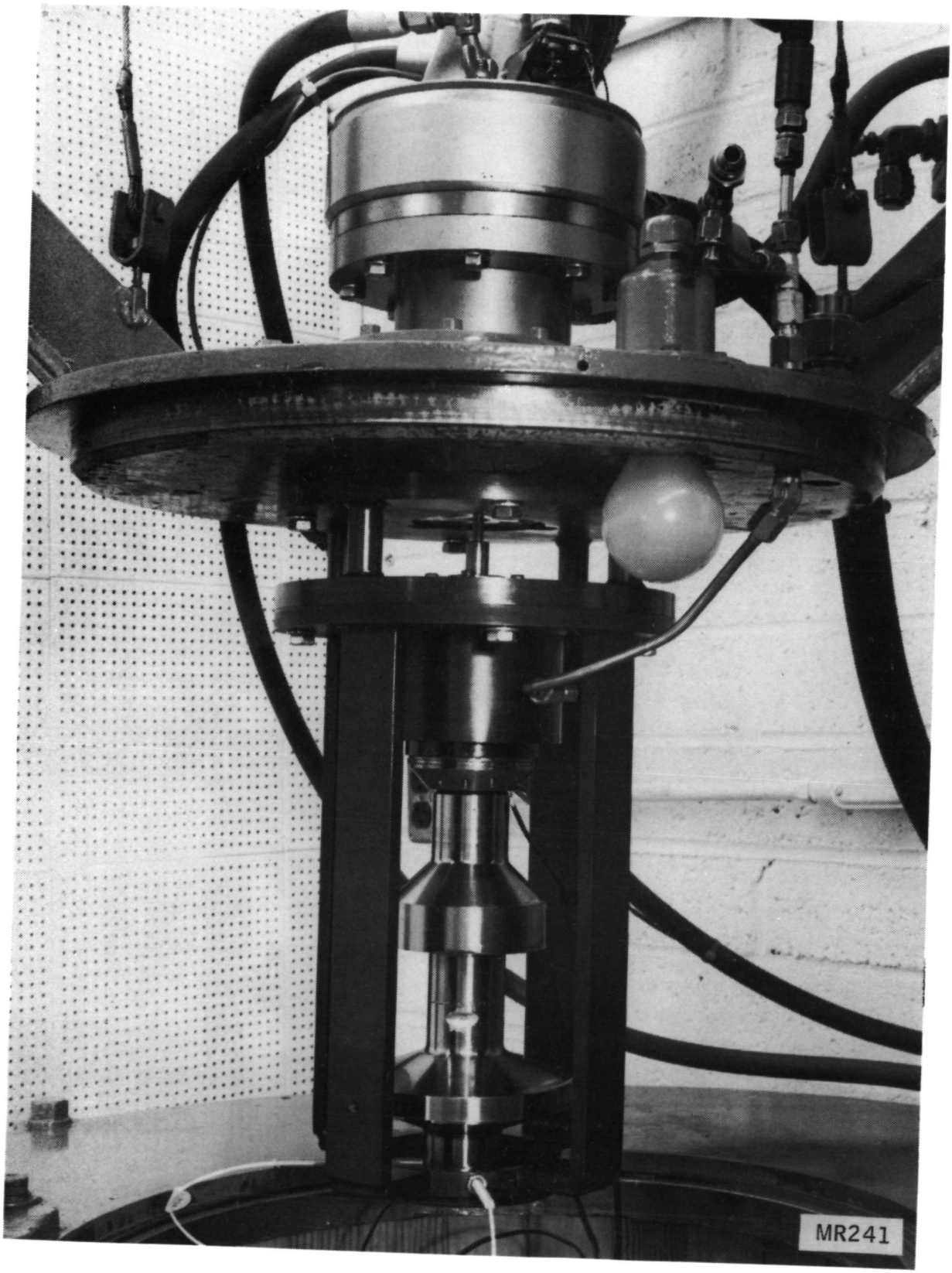

Figure 41 - Dummy Monorotor in Spin Test Rig

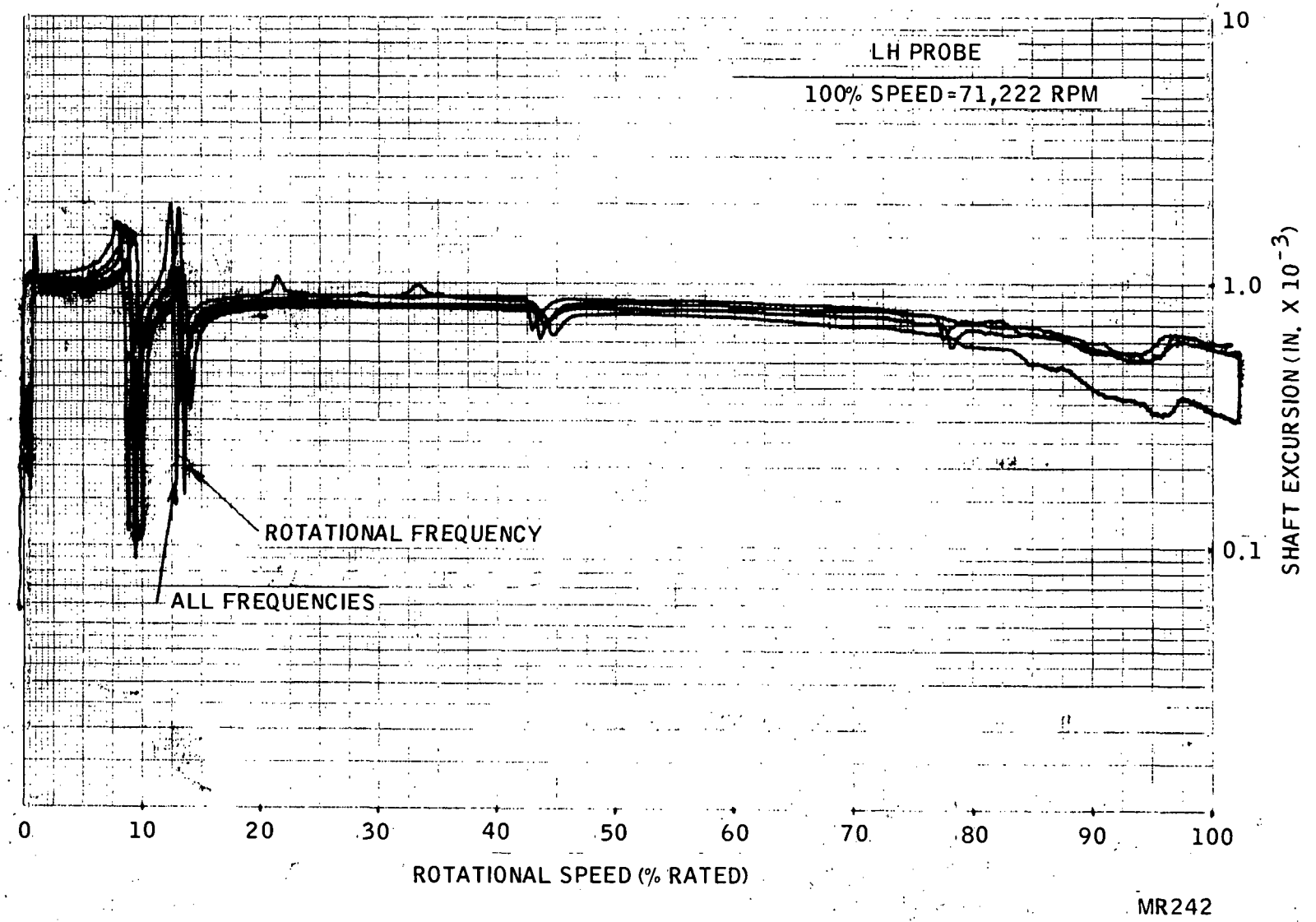

Figure 42 - Dummy Exducer Hub Excursion to 100 Percent

The third run brought the rotor to 120 percent speed (85,466 rpm). As shown in Figure 43, total rotor exducer runout was 0.0025 cm (0.001 in.).

The fourth run brought the rotor to 40 percent speed with no oil flow to the rotor bearings, bearings being lubricated by the residual oil in the system. During this run, the bearing outer race temperature increased from 310 K (99°F) to 328 K (130°F). The test demonstrated the feasibility of running Stress Coat tests on the actual monorotor assembly with only bearing capsule residual oil. This was desirable to prevent oil contamination of the Stress Coat lacquer film.

For all runs, satisfactory bearing temperatures, rotor shaft deflections, and vibrations were obtained. Systems for spin pit operation, rig lubrication, and dynamics instrumentation were satisfactory. The spin rig had proven to be suitable for spinning the final monorotor configuration.

Monorotor Spin Tests

Prior to spinning the advanced turbine monorotor, it was precisely balanced to the same close tolerance as the dummy rotor: maximum residual imbalance of 0.003 oz/in. Pilot bore diameters and blade tip diameters were measured and recorded, and the complete monorotor was coated with a brittle, strain indicating coating known as Stress Coat ST-80. The temperature environment was closely controlled during Stress Coat application and during the spin pit test installation to prevent changes in the Stress Coat strain sensitivity.

The spin pit installation was equipped with instrumentation to measure:

- Temperature of the outer race of the ball thrust bearing (nearest the first stage compressor).
- Turbine rotor speed.
- Dynamic strain of the first stage compressor disc in the axial direction (Figure 44).
- Dynamic strain of the monorotor disc in the axial and radial direction.
- Dynamic motions of the exducer hub of the monorotor in the radial direction.

Bearing outer race temperatures and turbine rotor speeds were recorded on an oscillograph strip chart recorder. The exducer probes (two, 90 degrees apart) and the turbine rotor speed were recorded on the Spectral Dynamics analyzer and motions of the rotor exducer hub were monitored on an oscilloscope. Dynamic strain measurements were also recorded on Sanborn oscillographs.

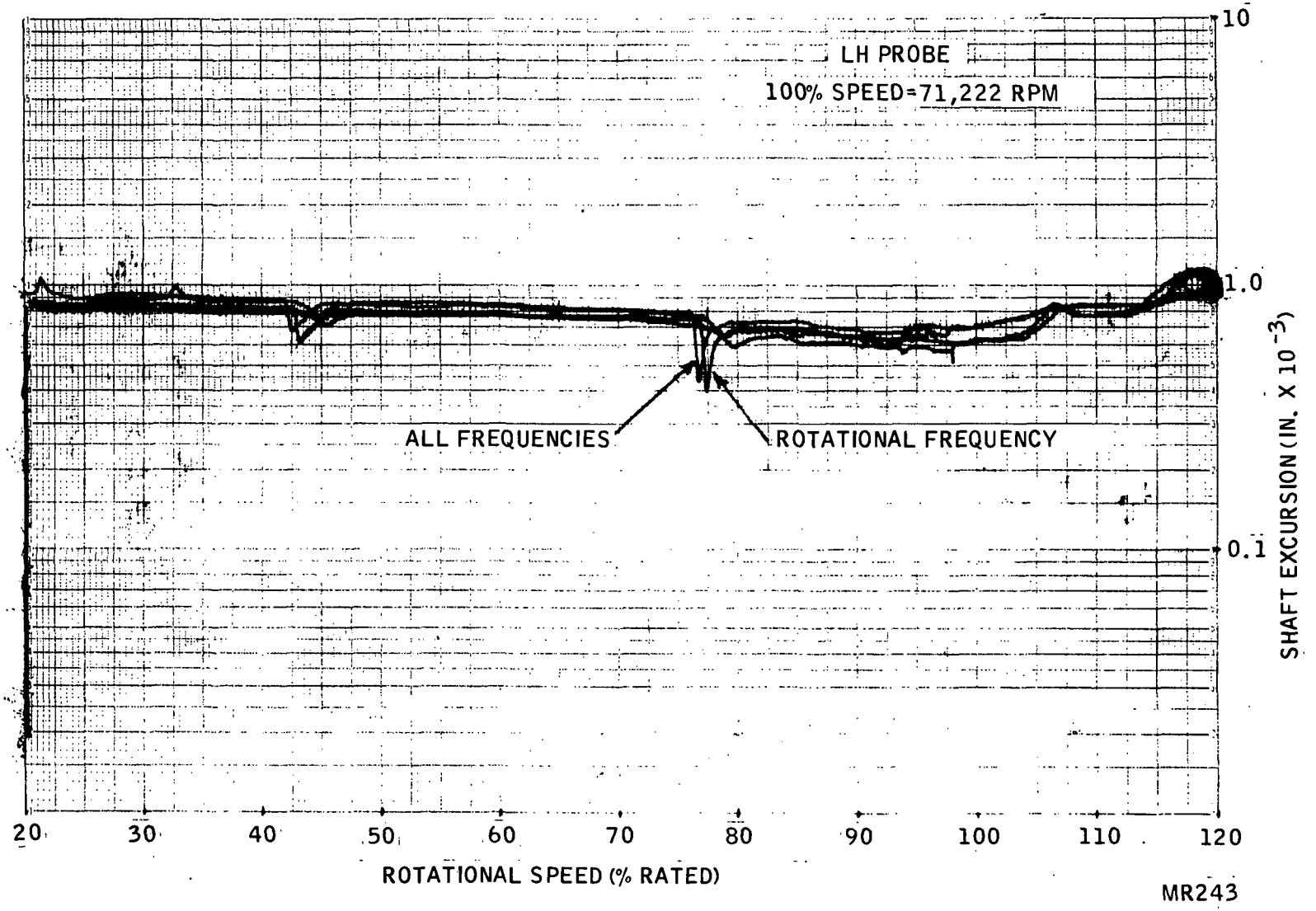

Figure 43 - Dummy Exducer Hub Excursion to 120 Percent Speed

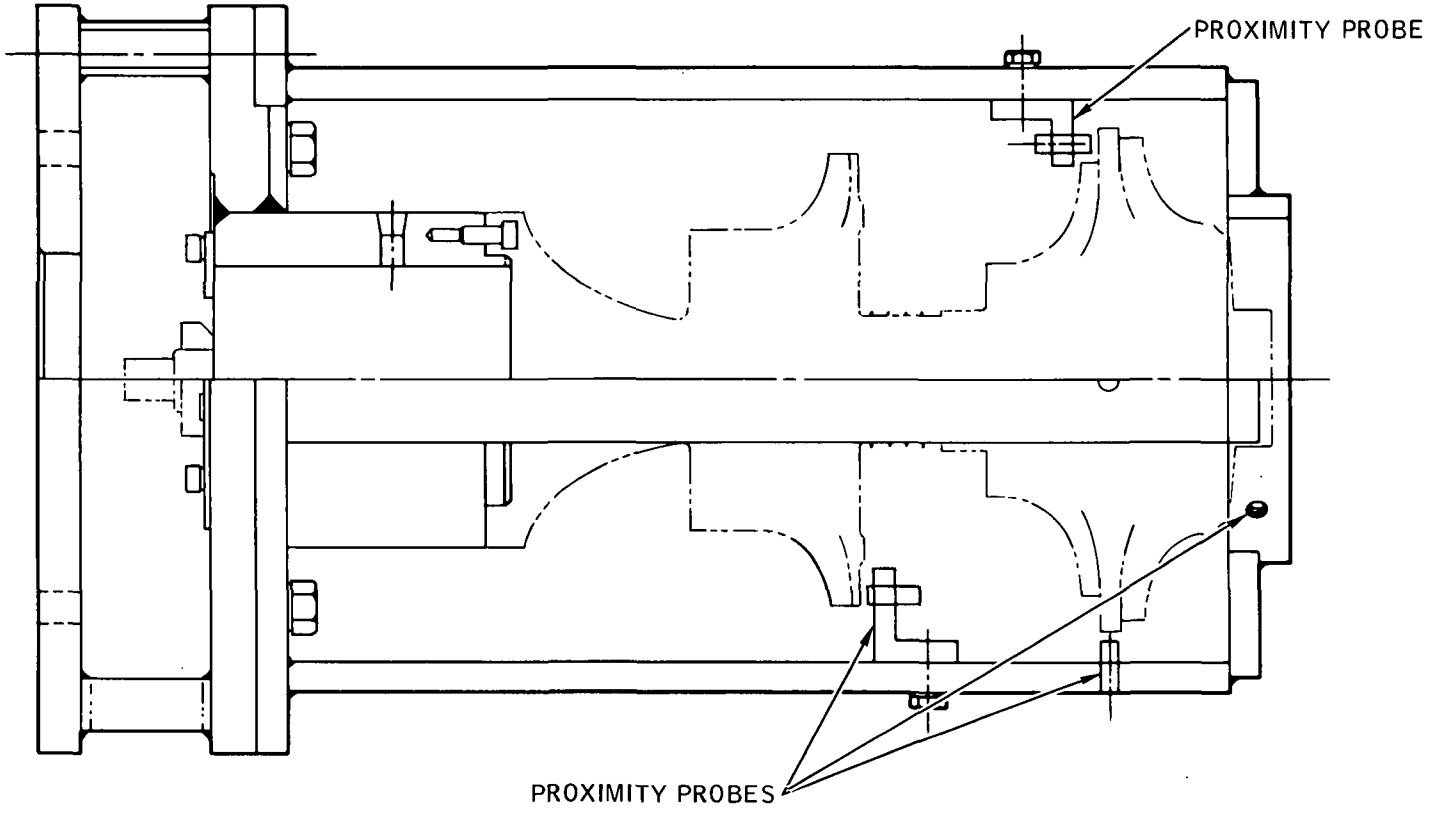

Figure 44 - Spin Cradle Proximity Probe Locations

The spin pit test of the advanced turbine rotor assembly was conducted in the following sequence:

- Accelerate turbine rotor assembly through the first critical speed and record measurement of dynamic excursions as indicated by the proximity probes.
- Rotate the monorotor assembly to 24,000 rpm and incrementally increase the speed to determine the first signs of Stress Coat cracking.
- Accelerate turbine rotor assembly to 100 percent design speed (71,222 rpm) to measure monorotor radial and axial distortions.
- Steady deceleration back to static conditions with subsequent measurement of all critical static dimensions and visual and Zyglo crack detection inspection.
- Conduct 1000 start/stop cycles to 105 percent design speed.
- Measure all critical static dimensions and inspect for cracks with Zyglo.
- Conduct three overspeed runs to 120 percent design speed.
- Measure all critical static dimensions and inspect for cracks with Zyglo.

The final monorotor assembly with instrumentation as shown in Figure 45 was lowered into the spin pit. Pit chamber pressure was reduced to near 101E +03 Pa (30 in. Hg) vacuum. To prevent lubricating oil from contaminating the brittle coating of the rotor Stress Coat, residual oil only was used to lubricate the ball bearings during this brief spin test.

The rotor was accelerated through the first critical speed (8 to 14 percent speed) to 19,586 rpm. Maximum excursion at the exducer hub when going through the critical speed was 0.020 cm (0.008 in.), including the assembly runout of 0.0068 cm (0.0027 in.). After coast-down, a visual inspection was made of the Stress Coat. Successive test runs were made to terminal speeds, increasing in 2200 rpm increments. The first Stress Coat cracking was noted in the compressor vane roots of the monorotor after the 33,510 rpm terminal speed test run. This crack was at a wheel radius of approximately 4.4 cm (1.75 in.) and on the convex side of the vanes.

If it is assumed that the speed at which Stress Coat cracking occurred was 33,510 rpm, the estimated stress at this point in the monorotor is equivalent to 502E + 06 Pa (73 ksi) when operating at design speed. This experimental stress level corresponds to the value obtained from the three-dimensional analysis of an isothermal monorotor operating at 71,220 rpm.

The Stress Coat was then removed from the rotor assembly to prevent Stress Coat particles from contaminating the oil supply. With the lube oil supplied to the

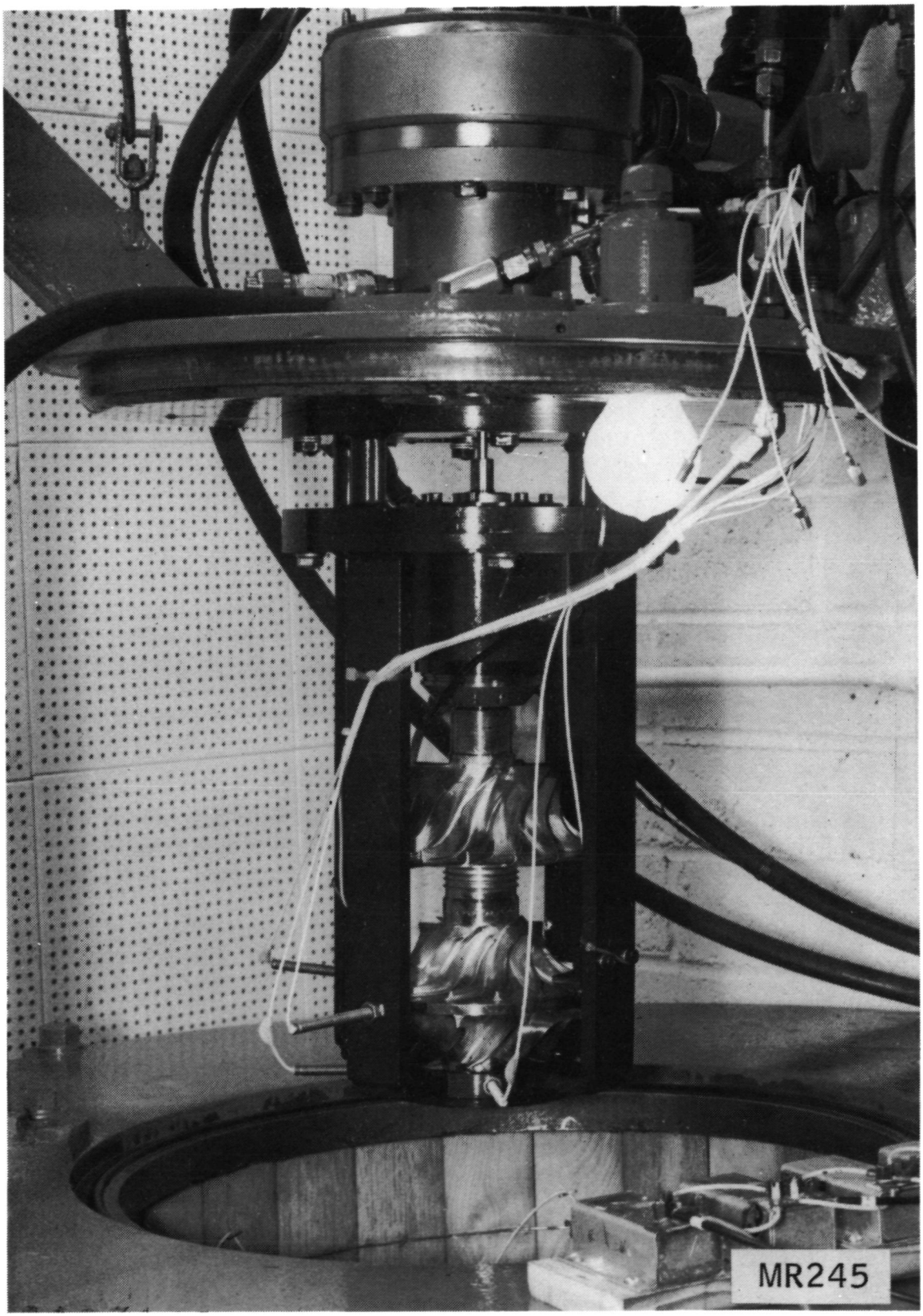

Figure 45 - Test Monorotor in Spin Test Rig

bearing jets at 10 psig, the turbine rotor was run to 100 percent speed (71,222 rpm). Exducer hub excursions were 0.013 and 0.017 cm (0.005 and 0.007 in.) when the rotor was accelerated through the first rotor critical speed. At 100 percent speed, the maximum excursion was 0.010 cm (0.004 in.).

During subsequent rotor spins to 100 percent speed, rotor disc radial growth and axial deflections were noted. A typical recording of these data (Figure 46) indicates that the maximum monorotor radial disc growth is 0.0114 cm (0.0045 in.) and the axial disc tip deflection is 0.0058 cm (0.0023 in.). These compare to the finite element stress model results of 0.0137 and 0.0086 cm (0.0054 and 0.0034 in.) respectively.

For the 1000 start/stop cyclic test, the oscilloscope was retained to monitor rotor exducer hub dynamics, and an oscillograph recorded the bearing outer race temperature and rotor speed. A start/stop cycle was completed every 20 seconds. After completion of 100 cycles, the rotor was partially disassembled and the bearings visually examined. Monorotor blades were inspected for cracks by Zyglo procedures. No distress or defects were revealed, and start/stop cycling was continued.

Start/stop cycles on the rotor system were continued until 619 cycles were completed. At this coast-down, excessive roughness was noted, and an investigation revealed a failed ball bearing at the upper position nearest to the spin pit drive motor. There was no damage to the monorotor. An examination of the bearing indicated that the most probable primary failure was cage fracture. There was no evidence of insufficient lubrication or excessive bearing temperatures, and no reason could be immediately assigned for the assumed primary failure. The bearings were replaced and the test cycles resumed; a total of 806 starts accumulated before a second similar bearing failure occurred. During this failure, operator error may have been instrumental in a decreased lube oil supply to the bearings.

A third set of bearings was installed, and an additional thermocouple was connected to the outer race of the upper bearing. The 1000-cycle test series was completed, and bearing temperature levels were found to be within 11 K (20°F). Measurement of critical diameters and Zyglo crack inspection showed no changes after the cyclic testing.

The rotating assembly was returned to the spin pit for final mechanical testing, comprising three spins to 120 percent design speed. For these tests, the proximity probes to measure axial and radial dynamic distortions were reinstalled.

Results of the tests to 120 percent design speed are shown in Figure 47, and they qualify the previously measured distortions. Measurement of critical diameters and Zyglo crack inspection showed no changes after the 120 percent speed test.

Five Bearings from the spin test rig were subsequently dispatched to Barden Bearing Co. for failure analysis. Results of this analysis are reported in Appendix B.

In summary, mechanical tests on the advanced monorotor confirmed the various analytical dynamic and finite element stress models used in the design stage and the capability of the rotating assembly to operate stably up to 120 percent design speed.

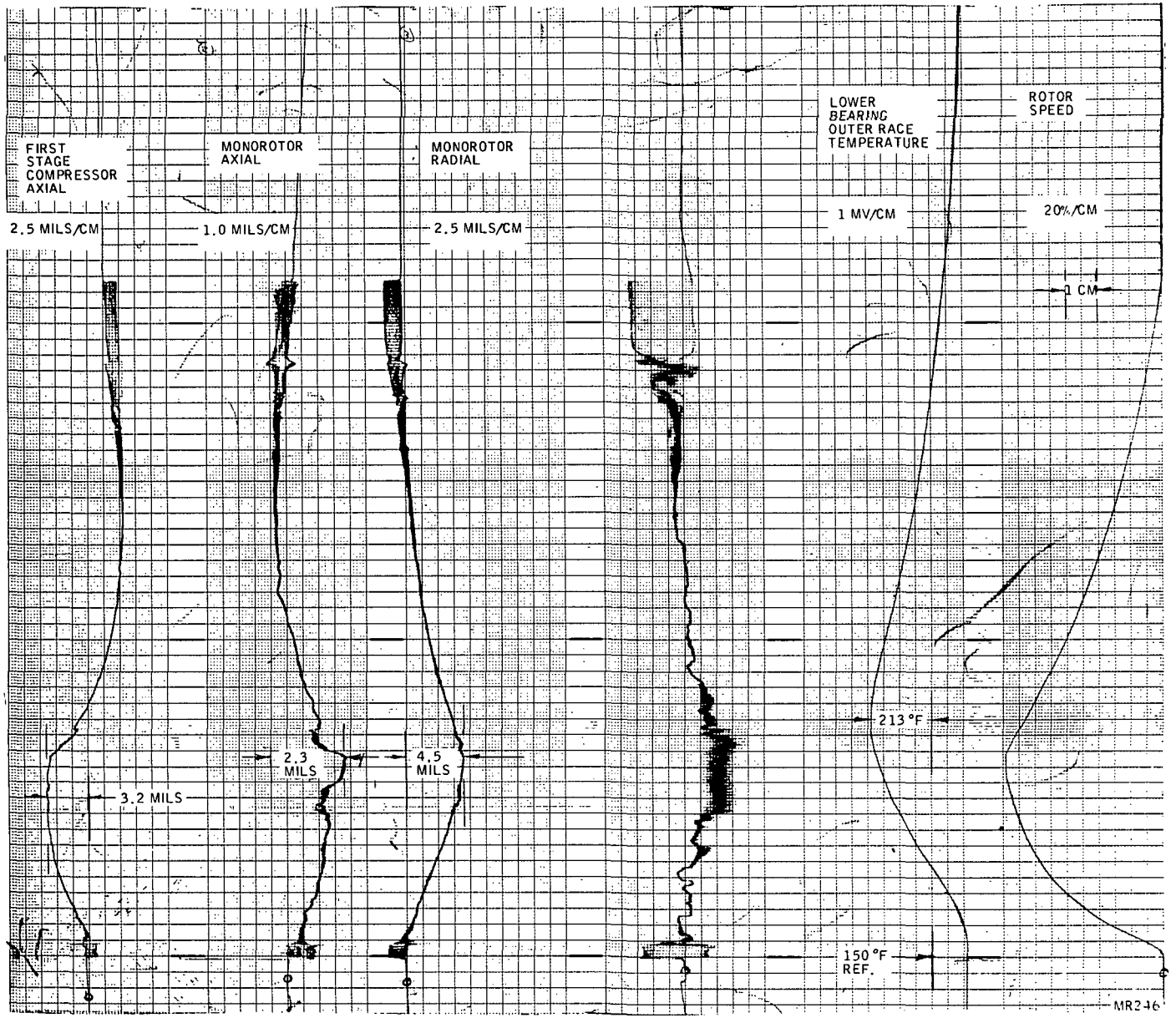

Figure 46 – Monorotor Start/Stop Cycle

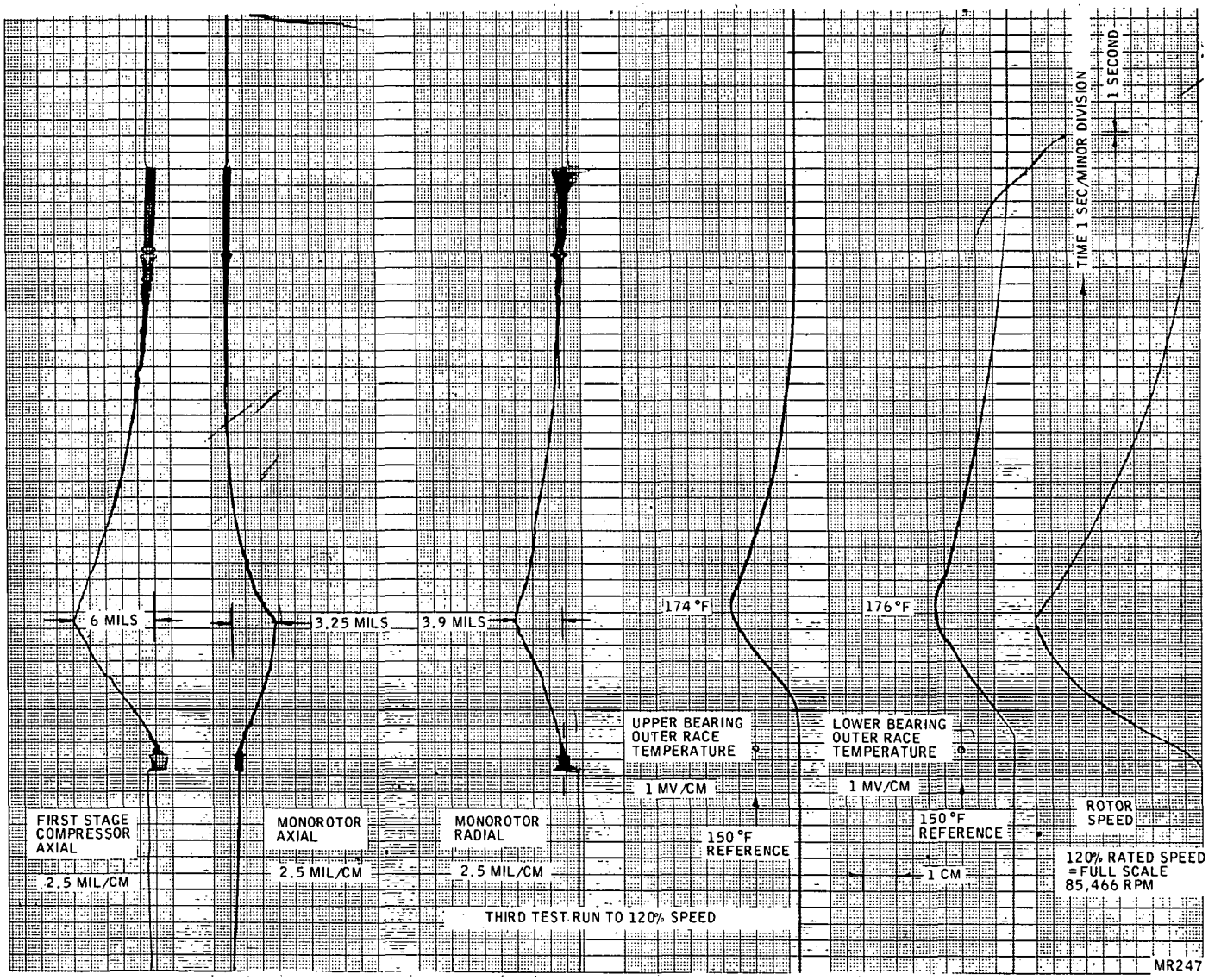

Figure 47 - Spin Test Trace to 120 Percent Speed

CONCLUSIONS AND RECOMMENDATIONS

Conclusions

- Low metal temperatures can be attained with the monorotor by direct conduction cooling, but the resulting relatively high temperature gradients cause large thermal stresses, particularly in the compressor blading near the shroud knee.

- The initial objective of attaining a design life of 1000 hours at a mixed rotor gas inlet temperature of 1478 K (2660°R) with an advanced radial inflow gas producer turbine was not analytically feasible. Derating to 1422 K (2560°R) is recommended to attain the required design life.

- In the high stress zones, approximately 2/3 of the stress level stems from thermal gradients; thus calculation accuracy of the temperature distribution is a key design factor.

- Low-cycle fatigue life considerations limit the number of transient power excursions from idle to maximum power to 7,000 compared with the design requirement of 30,000. The stress range values used for these transients were, however, pessimistic from the standpoint of localized bore stress redistribution.

- With this monorotor configuration, a tip leakage of 7 percent between the compressor and turbine flowpaths dilutes the monostator nozzle exit gas temperature. As a consequence, burner exit temperature is 95°C (170°F) hotter than the mixed rotor inlet gas temperature, requiring the use of an internally cooled monostator.

- A complete monorotor engine rotating assembly was fabricated and assembled for mechanical testing along with a dummy rotating group for initial confirmation of the test facility and equipment.

- Preliminary mechanical testing of a dummy rotating assembly in the spin pit correlated the analytical dynamic model results and confirmed the suitability of the test equipment for operating the final test assembly.

- Mechanical testing of the actual rotating assembly covering 1000 cold start/stop cycles and three spins to 120 percent design speed (85,466 rpm) were successfully completed.

- Dynamic distortion measurements and stress coat data confirmed the finite element stress model computations.

- Two bearing failures were experienced on the upper bearing carrying the least load. One failure may have been caused by an interruption in the oil supply.

- Design drawings were prepared for an aerodynamic test rig with which to evaluate both the compressor and turbine aerodynamic performances.

- Design layouts were prepared for a baseline engine configuration incorporating the monorotor and internally cooled monostator.

- Estimated standard day, sea level performance of the baseline engine configuration was an output power of 236 kW (317 hp) with a specific fuel consumption of 0.318 kg/kW-hr (0.523 lb/hp-hr) with a mixed rotor inlet gas temperature of 1422 K (2560°R).

Recommendations

- Thermal testing of the monorotor in an actual engine environment is recommended to verify the stress levels inherent in this design concept.

- Design layouts of a hot gas generator should be extended to include detail drawings and parts fabrication.

- A hot gas generator should be subjected to performance and thermal testing at design temperature and speed conditions.

APPENDIX A

MONOROTOR HEAT TRANSFER MODEL FOR CYCLE ANALYSIS

The effect of heat transfer on compressor or turbine performance can be calculated if the following assumptions are made:

a) Polytropic efficiency is constant throughout the compression or expansion.

b) The heat transfer rate is a known function of pressure, i.e.,

$$\frac{dq}{dp} = f(p)$$

The temperature rise for compression would be

$$dT = \frac{RT}{JC_p\eta_p}\frac{dp}{p} + \frac{f}{C_p}dp$$

For this analysis, the function f was assumed to be

$$f = f_1 + f_2 p$$

Then,

$$\frac{dT}{dp} - \frac{R}{JC_p\eta_p}\frac{T}{p} = \frac{f_1}{C_p} + \frac{f_2 p}{C_p}$$

Which has the solution:

$$\frac{T_2}{T_1} = x + \frac{f_1 p_1}{\left(C_p - \frac{R}{J\eta_p}\right)T_1}\left(\frac{p_2}{p_1} - x\right) + \frac{f_2 p_1^2}{\left(2C_p - \frac{R}{J\eta_p}T_1\right)}\left[\left(\frac{p_2}{p_1}\right)^2 - x\right]$$

Where

$$x = \left(\frac{p_2}{p_1}\right)^{\frac{R}{JC_p\eta_p}}$$

After calculating T_2 from the above equation, the shaft work absorbed by the compressor is given by

$$\Delta h_c = \int_{T_1}^{T_2} C_p dT - \int_{p_1}^{p_2} (f_1 + f_2 p)dp$$

The analysis of the turbine is performed in a similar manner. If the heat extraction from the turbine is given by

$$\frac{dq}{dp} = \theta(p),\ \theta > 0 \text{ for heat efflux}$$

Then

$$dT = \frac{\eta_P RT}{JC_p}\ \frac{dp}{p} + \frac{\theta}{C_p}\,dp$$

For a linear heat extraction profile where

$$dq = (\theta_1 + \theta_2 p)\,dp$$

$$\frac{dT}{dp} - \frac{\eta R}{JC_p}\frac{T}{p} = \frac{\theta_1}{C_p} + \frac{\theta_2}{C_p}\,p$$

With a solution of

$$\frac{T_4}{T_3} = y + \frac{\theta_1 p_3\left(\frac{p_4}{p_3} - y\right)}{\left(C_p - \frac{\eta R}{J}\right)T_3} + \frac{\theta_2 p_3^2\left[\left(\frac{p_4}{p_3}\right)^2 - y\right]}{\left(2C_p - \frac{\eta R}{J}\right)T_3}$$

where

$$y = \left(\frac{p_4}{p_3}\right)^{\frac{\eta R}{JC_p}}$$

The total power extracted from the turbine is

$$\Delta h_t = \int_{T_4}^{T_3} C_p\,dT - \int_{p_4}^{p_3} (\theta_1 + \theta_2 p)\,dp$$

THE BARDEN CORPORATION

DANBURY, CONNECTICUT 06810 | TELEPHONE: 203 744-2211 | TWX: 710 456 0098

July 7, 1976

Mr. Leland Blinman
Solar Division
International Harvester Corporation
2200 Pacific Highway
P.O. Box 80966
San Diego, Calif. 92138

Dear Lee:

SUBJECT: M204HX39 Bearings from Gas Turbine Engine Test Rig

REFERENCE: Your letters of June 8th and June 14th, 1976

This will confirm my telephone report to you regarding the five bearings sent to us for analysis. Bearings A & B failed after 617 cycles. Sample C failed after some 200 cycles. Bearings D & E were from a machine which did not fail, but had 200 cycles. Our findings on these bearings are as follows:

BEARING "A"

This bearing had failed dramatically. There is heavy distress in both raceways, but negligible outer ring land wear. The cage had broken up with gross wear distress in the pockets prior to cage break up. The cage O.D. shows light to moderate wear. The outer ring O.D. shows some fretting and metal pick up.

BEARING "B"

This bearing shows no real distress. There is some light pocket burnishing and there is metal, probably from the failure in bearing "A", imbedded in the cage surfaces. The inner ring running track is purely in thrust and shows some evidence of unbalance.

BEARING "C"

This bearing which consisted only of the inner and outer ring had failed dramatically. Similarly to bearing "A" except that the cage was missing and there was no significant distress evident on the outer ring.

BEARING "D"

This bearing was in excellent condition with relatively light thrust running tracks at a normal contact angle. There was some dirt denting in it. The outer ring track was three lobed, that is, with three wide areas. There was somewhat heavier scoring on the O.D. at each one of the wide areas in the outer ring track.

BEARING "E"

This bearing was very similar to Bearing "D", except the outer ring track which had just one slightly wider area. On the stamped face of the outer ring adjacent to this widened track area there is a light set of fretting marks.

It is apparent that bearing "A" was failing with considerable distress on the balls prior to cage break up. It does not look like insufficient lubrication because of the condition of the outer ring land and the cage O.D. There does not seem to be any significant unbalance or misalignment causing the failure. The fretting and metal pick up on bearing "A" O.D. could have been a result of the failure or it could have been a condition prior to failure that caused the ring to hang up in the housing. Although there is no direct indicator as to the cause of failure, we believe that it was probably due to insufficient spring load either from a too light spring or from hang up of one of the bearings in the housing.

Sample "C" gives us no further insight into the failures other than that it looks very similar to the failure in bearing "A" and, again, we expect it was from insufficient thrust load during operation from some condition that happened at this point in the test program.

The bearings "D" and "E" both show some adverse OD mounting situation. Although the bearings were operating with no problem and apparently could have continued to operate for their normal B-10 life, the outer ring track anomolies lead us to suggest that you look into possible mounting problems here. An improper housing condition could have led to hang up of the outer rings in the other two tests and caused the failure.

I hope these comments will be of assistance. The bearings are being returned herewith. If we can do anything further to assist you in this program please don't hesitate to call on us.

Very truly yours,

THE BARDEN CORPORATION

H.D. Williams
Senior Application Engineer

HDW/prm

cc: Mr. William Young,
Purchasing

HIGH NUMBER CR DISTRIBUTION LIST TOTAL COPIES 133

		No. of Copies *
1. NASA-Lewis Research Center 21000 Brookpark Road Cleveland, OH 44135 Attention:	M.S.	
Report Control Office	5-5	1
Technical Utilization Office	3-19	1
Library	60-3	2
W. L. Stewart	3-5	1
Fluid System Components Div.	5-3	1
L. W. Schopen	500-206	1
M. J. Hartmann	5-9	1
H. E. Rohlik	77-2	1
R. Y. Wong	77-2	15
J. Acurio	500-317	1
H. W. Davison	77-2	1
T. P. Moffitt	77-2	1
R. S. Colladay	77-2	1
F. S. Stepka	77-2	1
R. W. Graham	301-1	1
2. NASA Scientific and Technical Information Facility Attn: Accessioning Department P. O. Box 8757 Balt./Wash. International Airport MD 21240		30
3. NASA Headquarters Washington, DC 20546 Attn: N. F. Rekos (RLC)		1
H. W. Johnson (RLC)		1
D. Miller (RLC)		1
4. U. S. Army Aviation Material Laboratory Fort Eustis, VA 23604 Attn: John White		1
G. Easterling		1
E. Johnson		1
5. Headquarters Wright-Patterson AFB, OH 45433 Attn: S. Kobelak, TBP		1
R. P. Carmichael, XRHP		1
L. Debruge		1
E. Simpson		1

* Note Max. No. of Pages = 25,000

		No. of Copies
6.	Department of the Navy Naval Air Systems Command Propulsion Division, AIR 536 Washington, DC 20360	1
7.	Department of Navy Bureau of Ships Washington, DC 20360 Attn: G. L. Graves	1
8.	NASA-Langley Research Center Technical Library Hampton, VA 23365	1
9.	The Boeing Company Commercial Airplane Group Attn: G. J. Schott Organization: G-8410, M.S. 73-24 P. O. Box 3707 Seattle, WA 98124	1
10.	Douglas Aircraft Company 3855 Lakewood Boulevard Long Beach, CA 90801 Attn: J. E. Merriman Technical Information Center C1-250	1
11.	United Technologies Corporation Pratt & Whitney Aircraft Division Florida Research & Development Center P. O. Box 2691 West Palm Beach, FL 33402 Attn: R. A. Schmidtke P. Mitchell	1 1
12.	United Technologies Corporation Pratt & Whitney Aircraft 400 Main Street East Hartford, CT 06108 Attn: Library (UARL) R. Fish C. Stavalone E. Crow	1 1 1
13.	United Technologies Research 400 Main Street East Hartford, CT 06108 Attn: R. Olsen	1
14.	Detroit Allison Division, GMC Department 8894, Plant 8 P. O. Box 894 Indianapolis, IN 46206 Attn: Library D. Nealy H. Lueders	1 1 1

		No. of Copies
15.	Northern Research and Engineering 219 Vassar Street Cambridge, MA 02139 Attn: K. Ginwala	1
16.	General Electric Company Flight Propulsion Division Cincinnati, OH 45215 Attn: R. Rossbach Technical Information Center N-32	1
17.	General Electric Company 1000 Western Avenue West Lynn, MA 01905 Attn: Dr. C. W. Smith Library Bldg. 2-40M A. C. Bryans	1
18.	Curtiss-Wright Corporation Wright Aeronautical Wood-Ridge, NY 07075 Attn: S. Lombardo	1
19.	AiResearch Manufacturing Company 402 South 36th Street Phoenix, AZ 85034 Attn: R. O. Bullock J. Erwin Library J. J. Rebeske	1 1 1 1
20.	AiResearch Manufacturing Company 2525 West 190th Street Torrance, CA 90509 Attn: Library	1
21.	Union Carbide Corporation Nuclear Division Oak Ridge Gaseous Diffusion Plant P. O. Box "P" Oak Ridge, TN 37830 Attn: R. G. Jordon	1
22.	Avco Corporation Lycoming Division 550 South Main Street Stratford, CT 06497 Attn: Clause W. Bolton Yao Peng	1 1

No. of Copies

23. Teledyne CAE
1330 Laskey Road
Toledo, OH 43601
Attn: Eli. H. Benstein 1
Marlene S. Dowdell 1

24. Solar
2200 Pacific Highway
San Diego, CA 92112
Attn: Colin Rodgers 1

25. Goodyear Atomic Corporation
Box 628
Piketon, OH 45661
Attn: C. O. Langebrake 2

26. Iowa State University of Science and Technology
Ames, IA 50010
Attn: Professor George K. Serovy
Dept. of Mechanical Engineering 1

27. Hamilton Standard Division of United
Aircraft Corporation
Windsor Locks, CT 06906
Attn: Mr. Carl Rohrbach
Head of Aerodynamics and Hydrodynamics 1

28. Westinghouse Electric Corporation
Small Steam and Gas Turbine Engineering B-4
Lester Branch
P. O. Box 9175
Philadelphia, PA 19113
Attn: Mr. S. M. DeCorso 1

29. J. Richard Joy
Supervisor, Analytical Section
Williams Research Corporation
P. O. Box 95
Walled Lake, MI 48088 1

30. Lockheed Missile and Space Company
Technical Library
P. O. Box 879
Mountain View, CA 94040 1

31. James D. Raisbeck
The Boeing Company
224 N. Wilkinson
Dayton, OH 45402 1

		No. of Copies
32.	James Furlong Chrysler Corporation Research Office Dept. 9000 P. O. Box 1118 Detroit, MI 48231	1
33.	Elliott Company Jeannette, PA 15644 Attn: J. Rodger Schields Director - Engineering	1
34.	R. H. Carmody Dresser Industries, Inc. Clark Gas Turbine Division 16530 Peninsula Boulevard P. O. Box 9989 Houston, TX 77015	1
35.	California Institute of Technology Pasadena, CA 91109 Attn: Professor Duncan Rannie	1
36.	Massachusetts Institute of Technology Cambridge, MA 02139 Attn: Dr. J. L. Kerrebrock Dr. J. Louis	1 1
37.	Caterpillar Tractor Company Peoria, IL 61601 Attn: J. Wiggins	1
38.	Professor B. Lakshminarayana Department of Aerospace Engineering 233 Hammond Building Penn State University University Park, PA 16802	1
39.	Dr. Meherwan P. Boyce P.E. Department of Mechanical Engineering Texas A&M University College Station, TX 77843	1
40.	Commanding General U. S. Army Aviation Systems Command Attn: AMCPM-UA-TP (Mr. G. Kovacich) P. O. Box 209 St. Louis, MO 63166	1

		No. of Copies
41.	Commanding Officer Naval Air Propulsion Test Center Attn: Mr. D. Brunda Trenton, NJ 08628	1
42.	Commander USAF Aero Propulsion Laboratory Attn: AFAPL/TBP (Mr. T. Gingrich) Air Force Systems Command Wright-Patterson AFB, OH 45433	1
43.	Commanding Officer U. S. Army Mobility Equipment Research and Development Center ATTN: SMEFB-ED (Mr. J. E. Montgomery) Ft. Belvoir, VA 22060	
44.	Director U. S. Army Air Mobility R&D Lab. P. O. Box 209 St. Louis, MO 63166 Attn: SAVDL-SR/(Mr. J. Means)	1
45.	Commander Naval Air Systems Command Department of the Navy ATTN: AIR-53631F (Mr. E. Speiden) Washington, DC 20360	1
46.	Commanding Officer U. S. Army Combat Developments Command Transportation Agency Material Division Attn: Mr. R. W. Muschek Ft. Eustis, VA 23604	1
47.	General Motors Technical Center Warren, MI Attn: Ted Rosebrock Engineering Staff	1
48.	Onan Corporation 1400 73rd Avenue N.E. Minneapolis, MN	1
49.	Turbonetics, Inc. 968 Albany-Shaker Road Latham, NY 12110 Attn: Hans Pennink	1

		No. of Copies
50.	Fern Engineering Co., Inc. Buzzards Bay, MA 02532 Attn: Mr. Philip Levine	1
51.	Creare, Inc. Hanover, NH 03755 Attn: D. Japikse	1
52.	Dept. of Mechanical Engineering Arizona State University Tempe, AZ Attn: Dr. D. E. Metzger	1
53.	University of Minnesota Minneapolis, MN 55455 Attn: E. Eckert	1
54.	Purdue University Mechanical Engineering Dept. Lafayette, IN 47907 Attn: M. R. L'Ecuyer	1
55.	Dept. of Mechanical Engineering Michigan State University East Lansing, MI Attn: M. Potter	1
56.	Dept. of Aerospace Engineering University of Cincinnati Cincinnati, OH 45221 Attn: W. Tabakoff	1
57.	Office of Naval Research BCT #1 Washington, DC Attn: Dr. W. Raney	1